Analysis of Tau & Muon pairs at collision energies 192-209 GeV with OPAL detector at LEP

Georgios Anagnostou

Thesis submitted for the degree of
Doctor of Philosophy

Particle Physics Group
School of Physics and Astronomy
University of Birmingham

November 2002

Abstract

This thesis presents the measurement of the cross-sections and asymmetries of tau and muon pairs in e^+e^- collisions at centre-of-mass energies between 192 and 209 GeV. The analysis is based on data of about 433 pb^{-1} collected during the years 1999-2000, by the OPAL detector at LEP (CERN). Cross-sections and asymmetry measurements of the full energy events (non-radiative) are presented separately from the inclusive sample as these are potentially more interesting for new physics searches. The systematic uncertainties for the cross-sections and asymmetries are assessed. No significant deviations from the Standard Model theoretical predictions were found in either channel.

In addition, a separate study is presented concerning the feasibility of a possible forward jet trigger for the ATLAS detector at the LHC which is potentially interesting for the analysis of Higgs production via weak boson fusion. Different versions of the algorithm have been tested with simulated data and the preferred solution is presented.

Author's Contribution

Experiments in high energy physics like OPAL are based on a collective effort of hundreds of physicists and technicians. Thus, it is often difficult to distinguish an individual's work and this is the reason the results of the experiment are published with all collaborators included in the list of authors.

My own involvement started in the first year of my PhD, acting as a Birmingham representative for the Muon Endcap subdetector (ME). I was the last in a series of Birmingham OPAL group members who for 12 years operated and maintained the smooth running of ME. The detector was built by the Birmingham OPAL group in conjunction with the Rutherford Appleton Laboratory. Being responsible for the Muon Endcap subdetector involved daily monitoring of the gas and high voltage systems, reporting to OPAL status meetings and responding to any problems from the pit day or night.

During the first year I also started the study of a possible forward jet triggering for the ATLAS detector at the LHC. In my second and third year I moved onto measuring the cross-sections and asymmetries of muon and tau pairs, evolving the analysis performed at lower energies ([51], [71], [48]) for the high energy data collected during the last two years of LEP operation. The main analysis effort concentrated on undestanding the data for the more difficult tau pair channel.

Acknowledgements

First of all I would like to thank the particle physics group of the Universtity of Birmingham for offering me the opportunity to make this PhD a reality and covering the living expenses for a period of three years. Many thanks to Peter Watkins who supervised my OPAL work for his continued support and encouragement and to my supervisor on ATLAS Alan Watson for all his help. I would also like to thank Scott Talbot, as it would have been a lot harder having to do this from scratch. The Birmingham OPAL memebers Nigel Watson and David Charlton for always been very keen to answer my questions. Pat Ward for her suggestions that made the results better. Frank Votruba for reminding me from time to time that physics is fun. Jim Homer for helping me with ME and offering to do a night shift in OPAL when I was tired. Lawrie Lowe for his help with the local software. Thanks to my friends here in Birmingham Chris, David, Dimitris, Kathrine, Giannis, Mihalis, Olga, Richard, Yves (I hope to keep in touch with all of you). I would also like to thank my family in Greece Niko, Magda, Vaso, Milto and Despina.

Ria, thanks for being so patient and supportive.

Giorgos, Nov 2002.

Contents

List of Figures

List of Tables

$\grave{\alpha}\epsilon\acute{\iota}$ $\acute{o}$ $\theta\epsilon\acute{o}s$ $\acute{o}$ $\mu\acute{\epsilon}\gamma\alpha$s $\gamma\epsilon\omega\mu\epsilon\tau\rho\epsilon\widetilde{\iota}$

Chapter 1

Theory

1.1 Introduction

What is matter? What is matter made off? Can the complexity that surrounds us be explained with simple principles as the ancients dreamt? Can we understand why these principles are necessary? Particle physics attempts to answer some of these difficult questions based on an the interaction between interesting theoretical ideas and experiments that employ hundreds of scientists and technicians.

Today all known matter can be described with the help of a few fundamental pointlike components carrying spin 1/2, the leptons and quarks. The quarks and leptons are grouped into generations, each member having similar properties to the equivalent members in other generations. The first generation consists of a doublet of quarks (u, d), as well as a doublet of leptons (ν_e, e). All ordinary matter is made of the first generation. These elementary particles interact via four different type of forces: electromagnetic, strong nuclear, weak nuclear force and gravity. Quarks form bound states (via the strong force) of three quarks called baryons and bound states of a quark with an anti-quark called mesons. Mesons and baryons are all hadrons, as they all interact via the strong force (in contrast with the leptons).

Forces are mediated via the exchange of a quantum of the force field. The electromagnetic force is mediated by a photon, the strong force is mediated by eight different types of gluons, the weak force by the W^+, W^-, Z^0 gauge bosons and finally gravity by a hypothetical particle called graviton.

Table 1.1: A table of the fundamental particles together with their charges and masses.

			Generation		
			I	II	III
BOSONS		LEPTONS			
Charge		Charge			
$\pm 1e$	$\mathrm{W}^+\mathrm{W}^-$ 80.2 GeV/c^2	0	ν_e $< 3\,\mathrm{eV}/c^2$	ν_μ $< 0.19\,\mathrm{MeV}/c^2$	ν_τ $< 18.2\,\mathrm{MeV}/c^2$
0	Z^0 91.2 GeV/c^2	$-1e$	e^- 0.511 MeV/c^2	μ^- 105.7 MeV/c^2	τ^- 1,777 MeV/c^2
0	γ 0	QUARKS			
		Charge			
0	gluon 0	$+\frac{2}{3}e$	u 5 MeV/c^2	c 1,500 MeV/c^2	t $\sim$ 180,000 MeV/c^2
		$-\frac{1}{3}e$	d 8 MeV/c^2	s 160 MeV/c^2	b 4,250 MeV/c^2

1.2 The Gauge Principle

Gauge theories have an interesting history: they started from Weyl's effort to extend the very successful geometrical interpretation of gravity by general relativity, to the other then known force of nature, electromagnetism. Since then, the gauge principle had to overcome many phenomenological obstacles that hide the gauge character of the nuclear forces.

The basic idea of gauge symmetry is that if a physical system is invariant with respect to some rigid (space-time independent) transformations, G say, then it remains invariant when the group is made local (space-time dependent), that is, when $G \rightarrow G(x_\mu)$, where x_μ, μ=0, 1, 2, 3 are the space-time coordinates, provided that the ordinary space-time derivatives are changed to the covariant derivatives D_μ:

$$\partial_\mu \rightarrow \mathrm{D}_\mu = \partial_\mu + i\ q\ A_\mu$$

where q is the coupling and A_μ are the gauge fields which transform so that D_μ transforms covariantly with respect to the gauge group [1].

1.3 Symmetry breaking: The Higgs Mechanism

Gauge invariance was considered for a long period impossible to be a symmetry of the short range nuclear forces mediated by massive particles, as a mass term for gauge fields in a Langrangian is not gauge invariant [2].

Higgs proposed a mechanism to allow gauge fields to acquire mass, without destroying the gauge invariance of the Langrangian [3]. More specifically he proposed that there is a field in every space-time point (Higgs field) which interacts with the force-mediating gauge field. The interaction current is proportional to the gauge field (screening current condition). Such a term is similar to a mass term.

The above can be more clear by looking at the equation of a massless gauge field A_μ, interacting with a field ϕ (Higgs field):

$$\partial_\nu \partial^\nu A_\mu - \partial_\mu(\partial_\nu A^\nu) = J_\mu(\phi)$$

where the current is :

$$J_\mu(\phi) = iq(\phi^* \partial_\mu \phi - \phi \partial_\mu \phi^*)$$

by replacing $\partial_\mu \rightarrow \mathrm{D}_\mu = \partial_\mu + i\ q\ A_\mu$ and requiring the vacuum expectation value of ϕ to be non zero, we get the screening current condition (the current is proportional to the amplitude of the gauge field) :

$$J_\mu = -M^2 A_\mu$$

By replacing the above condition in the first equation we get the equation for a massive field (we also choose to work in Lorentz gauge : $\partial_\nu A^\nu = 0$) :

$$\partial_\nu \partial^\nu A_\mu + M^2 A_\mu = 0$$

A very important ingredient of this mechanism is that in order to have a screening current condition (a current proportional to the gauge field), a non-zero expectation value of the Higgs field is necessary. By assuming a potential invariant with respect to the gauge field of the form:

$$V(\phi) = -\ \tfrac{1}{2}\ \mu^2 \phi^* \phi + \tfrac{1}{2}\ \lambda\ \phi^2\ \phi^{*2}$$

and choosing any point in the circle where V(ϕ) is minimized (ground state), we get by definition a non-zero expectation value for the Higgs field (the V(ϕ) on the circle is non-zero). Thus, we have a system with a symmetric Lagrangian but with a ground state that does not display the same symmetry. A similar example in nature is the ferromagnet: A person living inside a ferromagnet would not be able to realize that he lives in a symmetric world as there is a 'preferred' direction due to the fact that the system is in the ground state (frozen). If the temperature is increased the symmetry is restored, in a similar way to the observation of electroweak symmetry in high energy physics experiments.

The theory is still gauge invariant to local Higgs field transformations. By 'freezing' this degree of freedom (the phase of the Higgs field), a mass term for the gauge boson is created. This result is independent of the value of the phase we choose for the Higgs field, so the symmetry is still there but hidden (or spontaneously broken as it commonly said). An important property of gauge theories is that they are proven to be renormalisable (t'Hooft [4]). By renormalisation we mean the procedure of redefinition of a finite numbers of parameters (e.g the charge, mass) in order to make the theory insensitive to divergences appearing in loop diagrams, at very high energies.

1.4 The Standard Model

The phenomenology of weak interactions during the sixties indicated that there are leptonic transitions (such as $\nu_e \leftrightarrow e^-$, $\nu_\mu \leftrightarrow \mu^-$), suggesting that these pairs should be regarded as doublets under some group. A weak isospin quantum number $t3$ can be assigned to distinguish between members of the multiplets:

$$t3 \;=\; \left\{ \begin{array}{l} (+1/2) \\ (-1/2) \end{array} \right. \quad \left(\begin{array}{c} \nu_e \\ e^- \end{array} \right)_L , \quad \left(\begin{array}{c} \nu_\mu \\ \mu^- \end{array} \right)_L \cdots \tag{1.2}$$

where $SU(2)_L$ is the group of unitary matrices with $det(U) = 1$ and L is a subscript indicating that only the left-handed parts of the wavefunctions are active in these leptonic transitions [5]. The crucial step was to follow Weyl's idea and require the group invariance to be space-time dependent (local gauge invariance). To achieve unification of weak interactions with electromagnetism Glashow [6] proposed that the group had to be enlarged to the direct product of $SU(2)_L \times U(1)_Y$, where $U(1)_Y$ is the group of unitary matrices associated with the weak isospin Y defined by the relationship $Q = t3 + 1/2\,Y$. In order to make the Lagrangian invariant under $SU(2)_L \times U(1)_Y$ local gauge transformations of the form:

$$\Psi \quad \rightarrow \quad \Psi^{'} \; = \; \Psi \;\; exp(i \; g^{'} \; Y \; \alpha(x)) \;\; exp(i \; g \; \vec{\sigma} \; \Lambda(x)) \tag{1.3}$$

we have to introduce the covariant derivative:

$$\partial_\mu \rightarrow D_\mu = \partial_\mu + i \; \frac{1}{2} \; g^{'} \; Y \; B_\mu + i \; g \; \vec{\sigma} \; \vec{W}_\mu \tag{1.4}$$

where $\alpha(x)$ and $\Lambda(x)$ are the rotations in $U(1)_Y$ phase and $SU(2)_L$ isospin space, g, $g^{'}$ are the couplings constants, $\vec{\sigma}$ are the Pauli spin matrices and $\vec{W}_\mu$, B_μ are the gauge fields. Each symmetry of the group introduces a conserved current (Noether theorem [7]). A Higgs doublet field is introduced with a vacuum expectation value chosen such as to ensure that the symmetry of the subgroup $U(1)_Q$ remains unbroken. The last constraint is introduced so that the photon remains massless after the symmetry breaking. A rotation is introduced to decouple the wave equations of the gauge fields B_μ, W^3_μ [5]:

$$\begin{aligned} A_\mu &= \cos\theta_W B_\mu + \sin\theta_W W^3_\mu \\ Z_\mu &= -\sin\theta_W B_\mu + \cos\theta_W W^3_\mu \end{aligned} \tag{1.5}$$

where θ_W is the mixing angle (Glashow-Weinberg angle), $W^\pm_\mu \equiv (W^1_\mu \mp i W^2_\mu)/\sqrt{2}$ and Z_μ are the weak mass eigenstates and A_μ is the massless photon.

In order to explain the fact that flavour(weak eigenstate) changing neutral currents were not observed in weak interactions, Glashow, Maiani and Iliopoulos proposed that

d, s weak eigenstates are given by a rotation of the d, s mass eigenstates (GIM mechanism [8]). The $SU(2)_L$ doublets are the quark and lepton doublets described in table 1.1, with $d^{'}$, $s^{'}$, $b^{'}$ quarks being mixed quark states given by a rotation of d, s, b:

$$\begin{pmatrix} d' \\ s' \\ b' \end{pmatrix} = \begin{pmatrix} V_{ud} & V_{us} & V_{ub} \\ V_{cd} & V_{cs} & V_{cb} \\ V_{td} & V_{ts} & V_{tb} \end{pmatrix} \begin{pmatrix} d \\ s \\ b \end{pmatrix} \tag{1.6}$$

The matrix is called Cabbibo-Kobayashi-Maskawa (CKM) [9], by the name of the physicists who proposed it as an extension to three generations of the GIM mechanism. The most important property of CKM matrix is its unitarity which reduces the number of free parameters.

The strong interaction is described by the $SU(3)_C$ local gauge group, where C is the conserved charge of the group called color. The spectrum of mesons and baryons can be explained by assigning a color to the quarks : red, green, blue (Quantum ChromoDynamics or QCD). The gauge field introduced are called gluons and are massless as the symmetry remains unbroken [5]. Particles exist only in neutral color, so mesons are made from quark-antiquark (colour-anticolour) pairs and baryons are combinations of red, green, blue quarks. Quarks can not been found in free states, but only asymptotically at very short distances or very high energies. This is due to the fact that the effective coupling constant of QCD, being a function of energy, is decreasing at high energies where quarks behave as free particles. The same coupling constant is increasing for low energies and pertubation theory is not able to describe the strong interaction for energies below 1 GeV. The fact that only colorless objects can be observed can be explained by the increase to infinity of the coupling constant, in the limit of zero energy (and infinite distance). This phenomenon is called confinement.

The description of the strong force by the gauge principle enlarges the group that describes all forces but gravity to the direct product $SU(3)_C \times SU(2)_L \times U(1)_Y$ known as the Standard Model [10]. The most spectacular experimental success of the model was the discovery of the $W^{\pm}$ and Z bosons very close to the values predicted by the Model in UA(1) experiment (CERN [11]). During LEP era the accuracy of the experimental tests of electroweak theory has reached unpreceeding levels and no evidence of any significant deviation from the model has been observed.

1.5 Beyond the Standard Model

The Standard Model despite its experimental success is not the final theory: it has a large number of free parameters which are not predicted or understood. We do not undestand why particles have the masses mentioned in table 1.1 or why there seem to be three generations of quarks and leptons. The necessity of the second and third generation is a mystery. Gravity remains out of this framework, but it is interesting that as pointed out by Utiyama [12] it is also a gauge theory. Thus, after decades of experimental and theoretical advances it seems that the gauge invariance is a crucial element of our understanding of nature.

Grand Unified Theories (GUTs) assume that the strong, weak and electromagnetic interactions are described by a single group G (eg. SU(5)), which after a symmetry breaking similar to the Higgs mechanism, is left with the symmetry of the Standard Model [5], [13]. This idea implies that leptons and quarks belong to the same multiplet, as there is only one coupling constant associated with G. The rotations of this group allows transitions between lepton and quarks which leads to non-conservation of baryon number. No evidence of baryon violation has been observed in proton decay experiments.

Another interesting idea towards unification is supersymmetry. It is an extension of space-time symmetry allowed by algebras based on both commuting and anticommuting relations [14]. A supersymmetry is an invariant property of tranforming boson fields to fermions and vice-versa, thus changing the spin of known particles by half a unit [15]. The non-observation of the supersymmetric partners of the known particles at low energies implies that if supersymmetry exists, it must be a broken symmetry. Supergravity is a theory with local supersymmetry. There is no experimental evidence in favour of supersymmetric theories at present.

String theories extend the pointlike particles to objects with more dimensions. The theory attempt to explain all particles as different vibration modes of a fundamental string. There are no experimental predictions at lower energies making the testing of the theory a difficult problem.

Chapter 2

The OPAL Detector

2.1 The LEP Collider

The Large Electron Positron collider is a synchrotron installed in a circular underground tunnel of 27 km circumference, 100m below the French-Swiss borders in Geneva. Bunches of electrons and positrons circulate in opposite directions and are forced to collide at 4 points where the OPAL, ALEPH, L3 and DELPHI detectors are located [16].

2.1.1 The Injection system

Acceleration of electrons and positrons takes place in several stages before the particles are injected into LEP (figure 2.1). Initially, electrons produced by thermionic emission from a heated cathode are accelerated up to 200 MeV by the LEP Injector Linac (LIL). The electrons are decelerated by a tungsten target producing photons (bremsstrahlung). The emitted photons produce electron-positron pairs which are separated by a magnetic field and further accelerated by a second linac up to 600 MeV. The positrons are then stored in the Electron Positron Accumulator (EPA) storage ring. When a sufficient population is stored, the electrons and positrons are injected into the

Proton Synchrotron (PS), where they are accelerated up to 3.5 GeV. In the final stage particles are accelerated to an energy of 20 GeV in the Super Proton Synchrotron, before being injected in LEP [16].

2.1.2 The accelerating and transport system

Charged particles travelling in a circular path emit radiation (photons) due to the change in their momentum. The energy loss ΔE that a particle undergoes during a complete revolution is proportional to the fourth power of its energy and inversely proportional to the radius of the accelerator:

$$\Delta E \propto \frac{E^4}{R},$$

For high energy light particles such as electrons and positrons this energy loss is significant and unless it is replaced the beam will be soon lost [17]. LEP was designed to have a large radius of 27 km in order to minimise this effect. The energy loss is compensated by using powerful high frequency (RF) cavities installed in the straight sections of LEP. In the initial phase known as LEP I, 128 conventional copper RF cavities were used to produce collision energies around the Z pole. Gradually from 1995 the copper RF cavities were replaced by superior superconducting ones which allowed several energy points up to 209 GeV to be explored (LEP II phase).

The beam pipe is evacuated and maintained at a pressure of 10^{-11} tor in order to reduce the collisions of electrons and positrons with air molecules. Dipole bending magnets keep the particles in circular orbit. Quadrupole, sextupole and octupole magnets are used to keep the beam focused.

2.2 The OPAL Detector

The Opal detector was designed to provide precise measurements of all type of final states occurring in e^+e^- collisions, over a solid angle of nearly 4π. The detector is

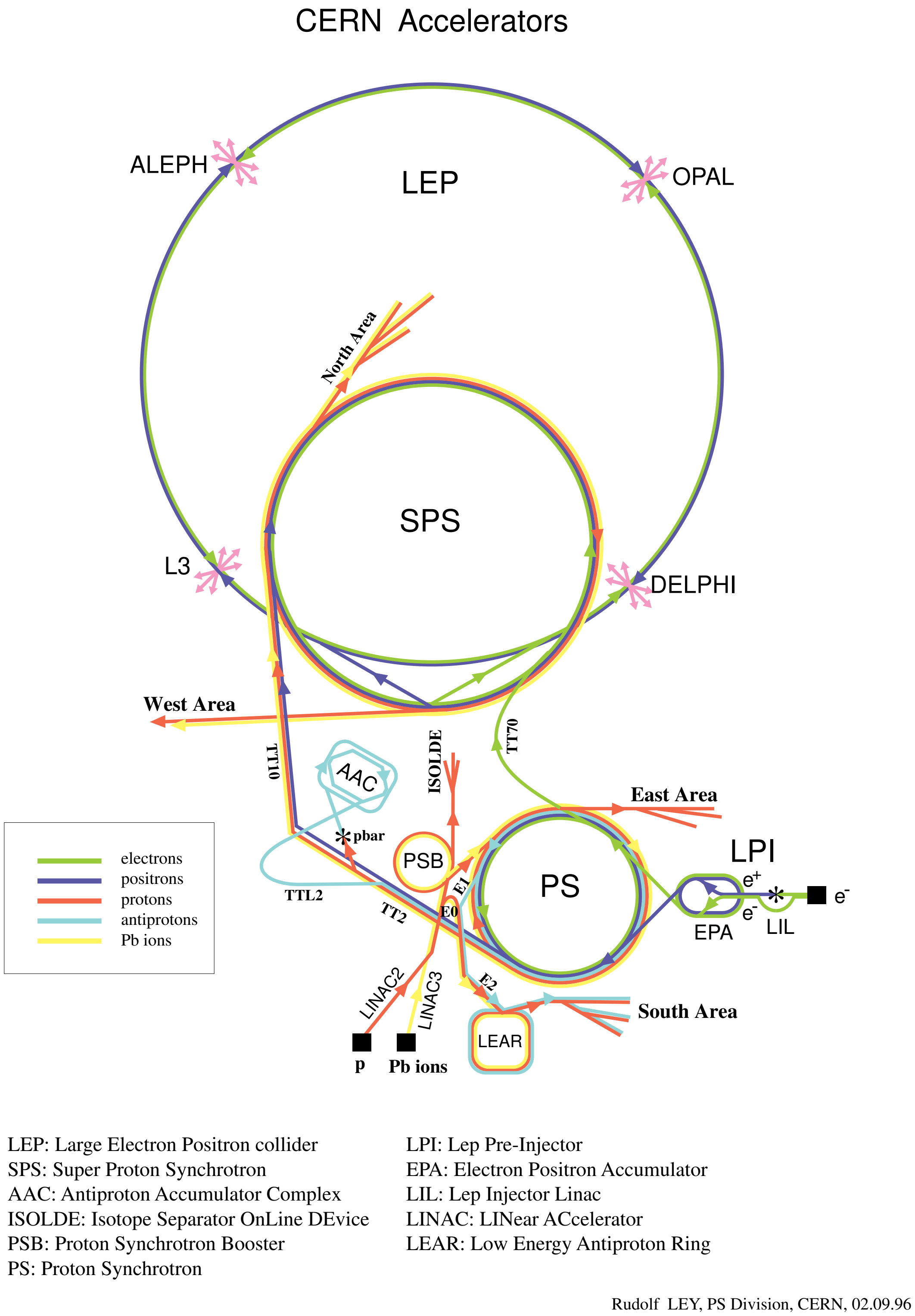

Figure 2.1: A diagram of the LEP accelerator and injector chain.

required to :

- measure the momentum of all charged particles,
- measure the energy and identify electrons and photons,
- measure the energy of hadrons,
- identify muons,
- measure the luminosity of the beam.

In order to fulfil these requirements, the detector consists of several layers of different subdetectors arranged in concentric cylinders around the beam pipe, closed at the ends by endcaps (figure 2.2). The central tracking system consists of a silicon microvertex detector and three drift chamber devices located inside a solenoid [20] . The central tracking detectors are surrounded by a lead glass electromagnetic calorimeter with presampler and the hadronic calorimeter. The outer level are muon detectors. The luminosity is measured by forward detectors close to the beam pipe.

The right-handed Cartesian co-ordinate system used can be seen in figure 2.2: The z axis is the electron direction, with x axis pointing approximately towards the centre (the LEP ring is inclined) of the accelerator and y axis vertical to the $x - z$ plane. In spherical coordinates, the polar angle θ is the angle with respect to the z axis and ϕ is the azimuthal angle when measured clockwise from the x axis.

2.2.1 The central tracking system

The central tracking detectors surround the beryllium beam pipe of outer radius 5.35 cm. It consists of a silicon microvertex detector and three drift chambers: a precision vertex detector, a large volume jet chamber and z-chambers. The whole central detector is located inside a solenoid providing a uniform magnetic field of 0.435 T. The curvature of the charged particles moving in the magnetic field is used to measure their

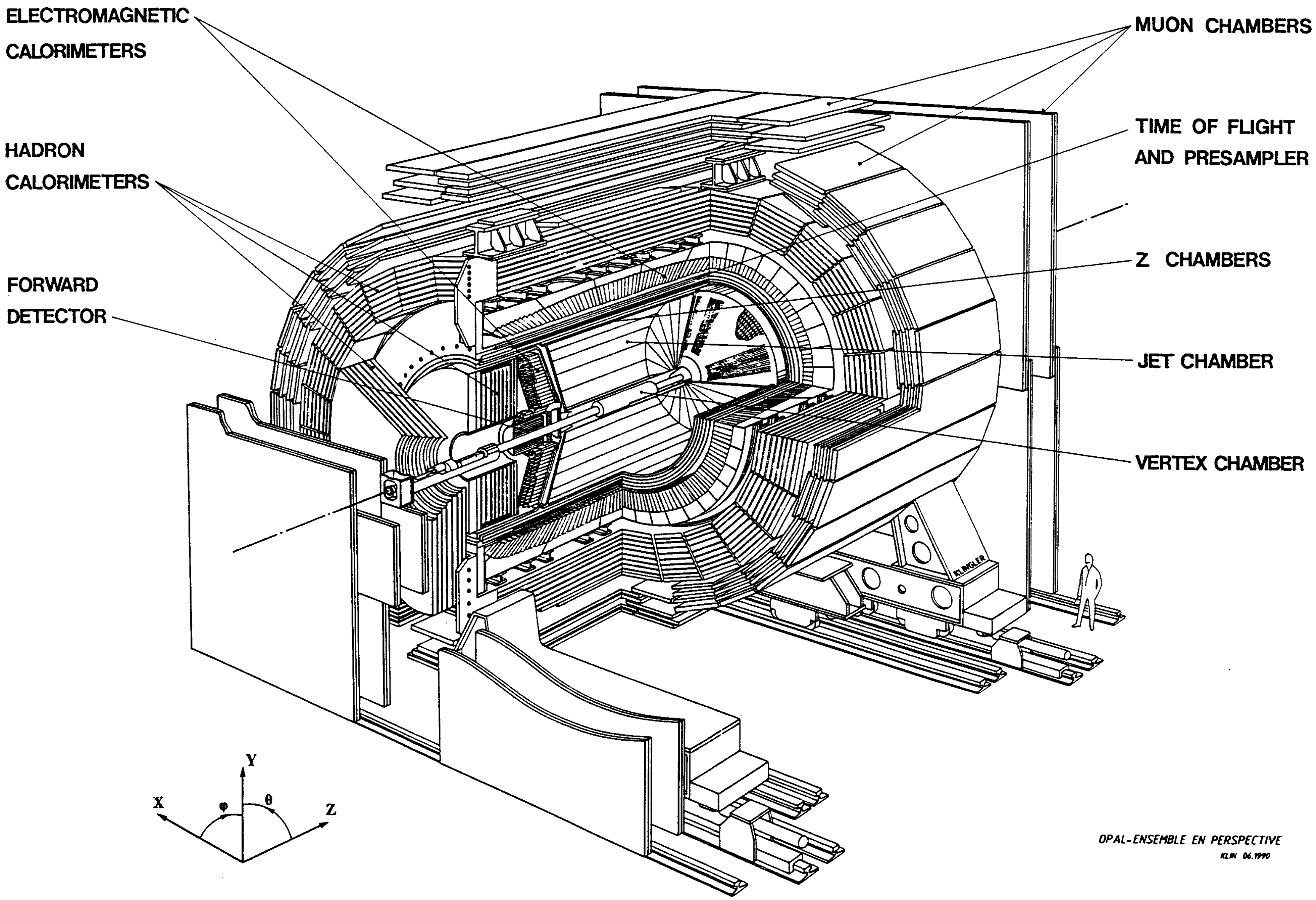

Figure 2.2: A cut-away perspective view of the OPAL detector.

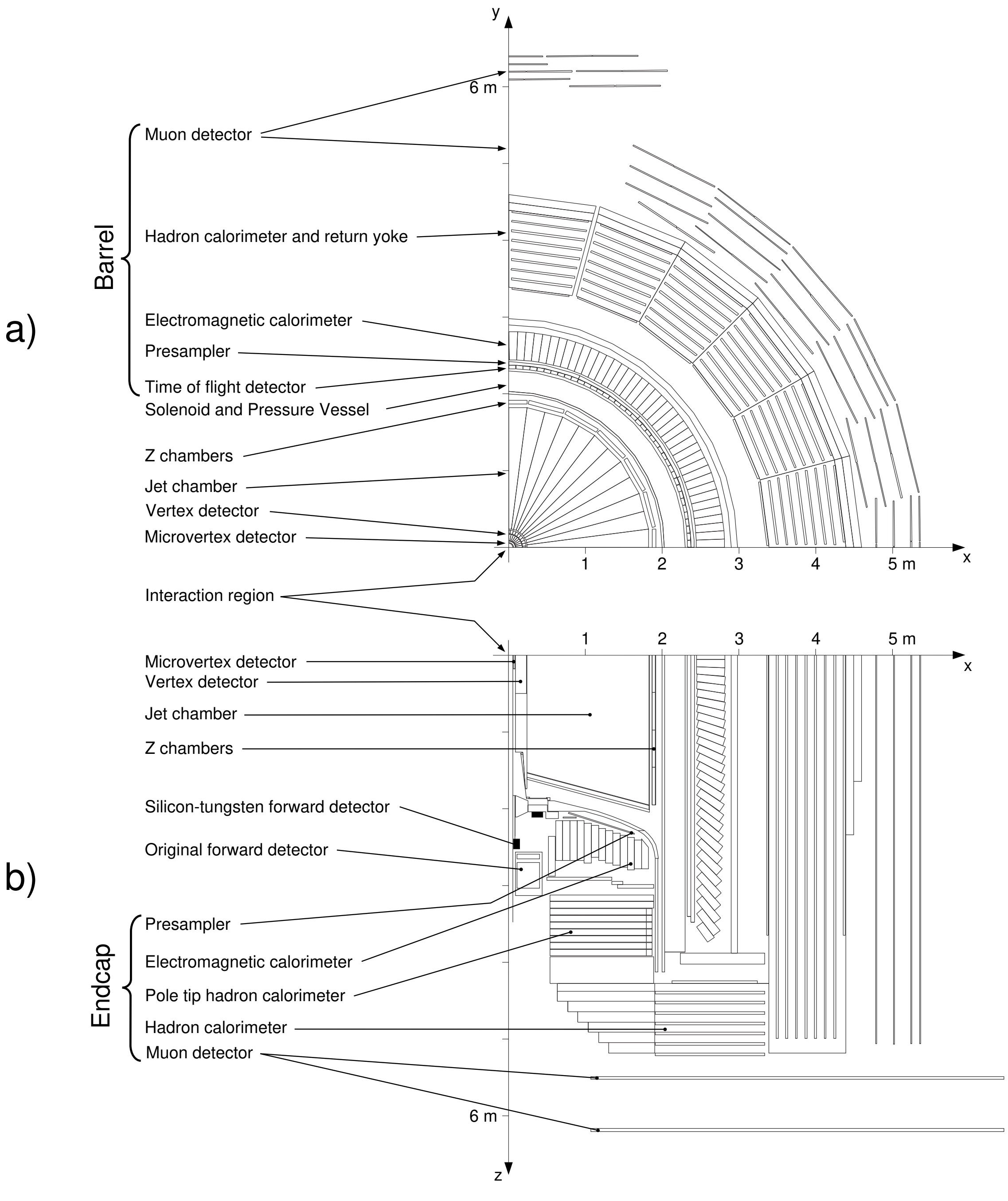

Figure 2.3: A diagram of a cross-section through the OPAL detector showing the subdetectors in (a) the barrel and (b) the endcap regions.

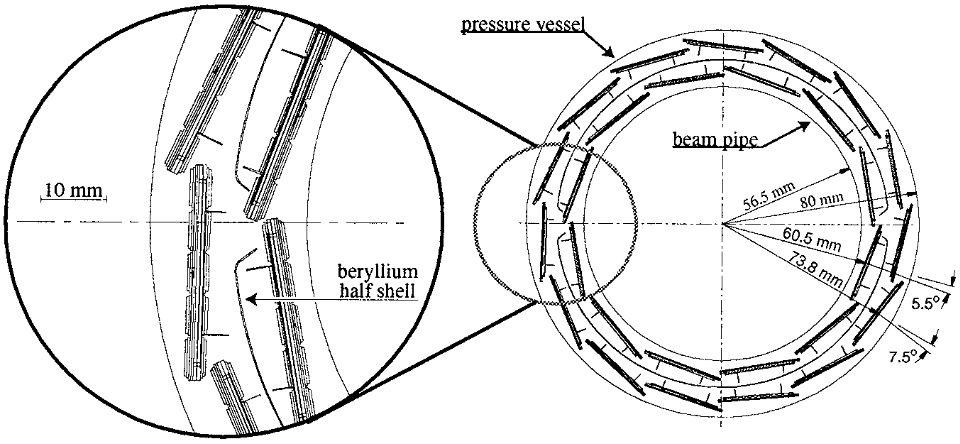

Figure 2.4: A diagram of the end view of the silicon microvertex detector.

momentum. The whole central detector is inside a pressure vessel in order to operate at a pressure of 4 bar. The cylindrical structure of the pressure vessel also provides mechanical support to the solenoidal coil.

- **The Silicon Microvertex Detector (SI)**

  The Silicon Microvertex Detector provides a high precision position measurement close to the interaction point [21]. The location of the decay vertices of short lived particles (secondary vertices) can be derived by extrapolation of the reconstructed tracks. This is a crucial element for many analyses including the measurement of the τ lifetime and identification of particles containing b and c quarks, Higgs searches etc. The detector is located between the beryllium beam pipe and the drift chambers pressure vessel. Two concentric layers of silicon wafer modules of 30 cm long are located at a radius of 6 cm and 7.5 cm from the beam axis. The wafers parallel to the beam axis have a resolution of 10 μm and are tilted to close ϕ gaps. Layers of wafers were also added at the z end perpendicular to the beam, to allow measurements in $r-z$ plane. The passage of charged particles through the silicon causes creation of electron-hole pairs. The electrons induce signals on microstrips implanted in the modules.

- **The Vertex Chamber (CV)**

  The vertex detector surrounds the silicon microvertex detector and assists the latter in the task of precise position measurements close to the interaction point. The detector has a length of 1 m and inner and outer radius of 8 cm and 25.5 cm respectively. Two concentric layers of drift chambers, each divided into 36 ϕ cells of wires (sectors) are located inside the pressure vessel of the central tracking system. Each sector in the inner layer contains a plane of 12 axial (parallel to the beam) sense wires which range radially from 10.3 cm to 16.2 cm with a spacing of 0.5 cm . Each outer sector contains 6 sense wires (called stereo wires) inclined at 4° with respect to the beam axis, in order to assist the z coordinate measurement. The stereo wires range radially from 18.8 cm to 21.3 cm with 0.5 cm spacing. The operation of all drift chambers is based on the same principle: they are filled with a gas mixture which is ionized when charged particles traversed the chambers. An electric field is applied between anode and cathode planes of wires. The time that the ionized electrons need to reach the anodes is translated into a distance from the wire. The centre of gravity of the signals induced in neighbouring wires gives very good position resolution. In the $r-\phi$ plane this is about 50 μm . The time difference of the signal induced in the two ends of the anode wires combined with stereo wire information give a resolution of 700 μm in the r-z plane.

- **The Jet Chamber (CJ)**

  The jet chamber is the principal tracking device in OPAL providing information for track reconstruction and possible particle identification [22]. It is based on a similar design to that used in JADE experiment at PETRA [23]. It is a cylindrical drift chamber 4 m long, having an inner and outer radius of 0.5 m and 3.7 m respectively and it is located inside the pressure vessel. The detector consists of 24 identical ϕ sectors. Each sector has radial $r-z$ planes, each plane consisting of 159 sense wires running parallel to the beam axis. The solid angle covered by the detector is approximately 98% of 4π. The drift time together with the wire position provide position information in the $r-\phi$ plane, with a resolution of 135 μm. The ratio of the charges collected at each end of the wires gives a coarse z coordinate measurement with a resolution of 6 cm.

- **The Z Chambers (CZ)**

  The basic task of this subdetector is to improve the z coordinate measurement of particles leaving the jet chamber. It is another cylindrical barrel layer of drift chambers surrounding the Jet Chamber and covering a polar angle from 44° to 136°. The detector is divided in 24 parts in ϕ, each part 4 m long, 50 cm wide and 5.9 cm thick. It is also divided in 8 cells in z, each cell being $50 \times 50 \times 5.9$ cm, so that the maximum drift distance is 25 cm in the z direction. Inside each cell there are 6 anode wires running in the ϕ direction. The spatial resolution for the z coordinate is approximately 300 μm.

- **Time Of Flight (TOF)**

  The purpose of the TOF system is to generate trigger signals, as well as help particle identification by measuring the time of flight. It also assists the suppression of cosmic background by rejecting particles with time of flight inconsistent with an event occuring from a collision.

  The barrel TOF detector (TB) consists of 160 scintillation counters forming another barrel layer of radius 2.36 m. The counters are 6.84 m long with a cross section 4.5×9 cm^2, wrapped with foil and black PVC sheet. Two plexiglass light guides at each end of the counters collect the light and transfer it to phototubes where it is converted to electrical signals. The endcap TOF subdetector (TE) consists of a layer of 10 thick scintillation tiles and was installed in 1995 to extend trigger capabillities for the higher LEP2 backgrounds. The read out is performed using fibres to carry the light collected outside the solenoidal magnetic field.

- **The Magnet**

  The magnet is designed to provide a uniform ($\pm 0.5\%$) magnetic field of 0.435 T inside the central tracking volume. It is divided into a thin, water-cooled, aluminium solenoidal coil which surrounds the central tracking volume and a return yoke made of soft steel plates. The return yoke is also used as the absorption medium for the hadronic calorimeter. The solenoid is not divided into shorter sections in order to keep the magnetic field between solenoid and the return yoke low, to allow the operation of the electronics in this region.

2.2.2 The Electromagnetic Calorimetry

The basic task of the electromagnetic calorimeters is to measure the positions and the energies of electrons, positrons and photons. They also provide useful information to discriminate $\pi^0 s$ from photons. The calorimeters in general have an absorbing medium of high density which decelerates the incoming particles, producing photons (bremsstrahlung). The photons create electron-positron pairs, which interact further with the material to generate more photons. Eventually all or most of the energy of the particle will be converted to 'heat' by this cascade of interactions, called electromagnetic shower.

For both barrel and endcap electromagnetic calorimeters the absorbing medium is lead glass blocks. Some particles in the shower are produced at a speed greater than the speed of light in the medium, causing the emission of Cerenkov radiation which is collected and detected by phototubes. The lead glass detector has an excellent intrinsic resolution of $\sigma_E/E \simeq 5\%/\sqrt{E}$ where E is the energy in GeV of the incoming particle, but due to the fact that there are 2-4 radiation lengths of material before the calorimeters, it is likely for the electromagnetic shower to be initiated before reaching them. This phenomenon degrades the energy resolution significantly. In order to improve the measurement, presampling detectors are used before both barrel and endcap calorimeters. The energy deposit in the presampler gives an estimation of the evolution of the shower which is used to correct the measurement of the calorimeter.

- **The Barrel Electromagnetic Presampler (PB)**

  The barrel presampler is a cylindrical layer of radius 2,4 m and length 6.6 m located between the TOF system and the electromagnetic calorimeter and covering a polar angle of $|\cos\theta| < 0.81$. The detector is divided into 16 ϕ chambers, each chamber consisting of two layers of limited streamer mode tubes. These are drift chambers using thick anode wires and operated in limited streamer mode. The anode wires run parallel to the beam axis and in each layer of tubes there are 1 cm wide cathode strips on both sides oriented at $\pm 45^\circ$ with respect to the anodes. The spatial positions are obtained by measuring the signals at both ends of the strips (charge division).

- **The Endcap Presampler (PE)**

  The endcap presampler consists of 32 multiwire chambers in 16 ϕ wedges (sectors), forming an umbrella shaped structure. The detector is located between the pressure vessel of the central tracking system and the electromagnetic endcap covering a polar angle of $0.95 > |cos\theta| > 0.83$. In order to fulfill the requirement for good energy and position resolution together with the severe space restriction in the endcaps, the thin multiwire chambers are operated in a high gain mode.

- **The Barrel Electromagnetic Calorimeter (EB)**

  The barrel electromagnetic calorimeter is made of 9440 lead glass blocks, forming a cylindrical layer at a radius 2.46 and covering a polar angle of $|cos\theta| < 0.81$ [24]. Each lead glass block has a cross-section of $10 \times 10\,\mathrm{cm}^2$ and depth 37 cm, which is approximately 24.6 radiation lengths. The longitudinal axis points towards the interaction region in order to reduce the probability for a particle to traverse more than one block, having a small offset with respect to the collision point to reduce particle losses in the gaps between blocks. The Cerenkov light produced is collected and guided to magnetic field tolerant phototubes where it is converted to an electrical signal.

- **The Endcap Electromagnetic Calorimeter (EE)**

  On each side of the detector and between the pressure bell of the central tracking system and the hadronic pole tip calorimeter, there is a domed shaped array of 1132 lead glass blocks covering a polar angle of $0.81 < |\cos\theta| < 0.98$. The lead glass blocks are aligned parallel to the beam axis, due to geometrical constraints imposed by the pressure bell. They have approximately 22 radiation lengths of material and are instrumented by specially developed Vaccum Photo Triodes (VPTs) in order to operate in the full axial field of the magnet.

2.2.3 The Hadronic Calorimetry

The purpose of the hadronic calorimeter is to measure the energy of the hadrons that traverse the electromagnetic calorimeter and provide useful information for muon identification. The iron of the return yoke of the magnet is used as absorbing medium. Inelastic nuclear interactions of the incoming hadrons with the absorber lead at high energies to multiparticle production and particle emission originating from nuclear decay of excited nuclei [25]. This cascade process is called a hadronic shower and may be initiated in the 2.2 interaction lengths of material before this detector. In order to improve resolution, information from the electromagnetic calorimeter is used to correct the energy of the hadronic shower. The energy is sampled by positioning streamer chambers between the layers of iron. The detector is divided into barrel, endcap and pole-tip calorimeter covering a solid angle of 97% of 4π.

- **Barrel and Endcap Hadronic Calorimeters (HB and HE)**

  The barrel detector consists of 8 layers of iron slabs sandwiched between 9 layers of limited streamer tube chambers [26]. It has a length of 10 m with an inner and outer radius of 3.4 m and 4.4 m respectively. The endcap detector is a very similar design with 7 layers of 10 cm thick iron sandwiched between 8 layers of limited streamer tubes. Signals are induced on pads in the inner face of the chambers and on strips on the outer face. The detector is divided into 48 bins in ϕ and 21 bins in θ, by grouping together the layers of pads to form calorimeter towers.

- **Hadron Pole-Tip Calorimeter (HP)**

  The Pole-Tip hadron calorimeter is used to extend the coverage of the polar angle up to $|\cos\theta| < 0.99$. It is similar to the barrel and endcap hadronic calorimeter with 9 layers of iron and in between 10 layers of detector devices. These are multiwire proportional chambers operating in a high gain mode (similar to those used in the electromagnetic endcap presampler). The intrinsic energy resolution is $\sigma_E/E \simeq 100\%/\sqrt{E}$, but deteriorates up to $140\%/\sqrt{E}$ when the material in front of the detector is taken into account.

2.2.4 The Muon Detectors

The amount of material of all the subdetector layers described so far exceeds 1.3 m of iron equivalent or approximately 7 interaction lengths for pions. Thus, a particle traversing all these layers is very likely to be a muon. The task of the muon detector is to identify muons in the presence of a small hadronic background. The identification of these particles is based on extrapolation of the track as reconstructed in the central track system, taking into account energy loss and multiple coulomb scattering and matching it with a track in the muon detector.

- **Muon Barrel (MB)**

  The barrel muon detector of 110 drift chambers forming a cylindrical layer that covers a polar angle up to $|\cos\theta| < 0.72$ [27]. Each chamber has a length ranging from 6 to 10.4 m and cross-section of $120 \times 9\,\text{cm}^2$. It is split into two adjoining cells, with anode wires running parallel to the beam axis. Cathode strips are located on the inner suface of the cells, with diamond shaped cathode pads opposite to the anode wire and in parallel to the beam axis. The position of particles in the $r-\phi$ plane are measured by using the drift time to the anode wires, yielding a resolution of 0.15 cm. The z coordinate is measured by the time difference of signals at both ends of the anode wires, combined with the signals induced on the diamond shaped anode wires [27].

- **Muon Endcaps (ME)**

  In each endcap of the detector there are 2 layers of four rectangular chambers $6 \times 6\,\text{m}^2$ and 2 patch chambers $3 \times 2.5\,\text{m}^2$ perpendicular to the beam axis covering an area of about $150\,\mathrm{m}^2$ and a polar angle of $0.67 < |\cos\theta| < 0.985$ [28]. Each chamber consists of two layers of limited streamer tubes spaced by 19mm and with the anode wires perpendicular with respect to each other. Read-out aluminium strips are located at each side of the layer of streamer tubes, with the ones on one side oriented perpendicular to the wires while the others are parallel. A weighted average of the pulses induced on the strips is used to locate the streamer with a resolution of ~1mm [28].

2.2.5 The FD and SW Luminometers

The main task of the forward detectors is to measure the beam-luminosity, defined as the factor in the event rate depending on the characteristics of the beams. Let us assume that e^+ and e^- beams of equal energy and consisting of bunches of particles are colliding: if the bunch of electrons has a cross-sectional area A and number of particles $N1$, a particle in the positron bunch will 'see' a fraction of the area equal to $\sigma N1/A$ where σ is the cross-section of $\mathrm{e^+e^-} \to \mathrm{X}$ (the total area of overlap of two colliding particles). In every passage the number of interactions will then be $\sigma N1N2/A$, where $N2$ is the number of particles per bunch in the positron beam. Assuming a frequency of bunch collisions f, the event rate will be [17]:

$$\frac{\mathrm{d}N}{\mathrm{d}t} = \sigma\ \frac{fN1N2}{A}, \tag{2.1}$$

The luminosity is defined as: $L \equiv \mathrm{f}N1N2/A$ and it is measured integrated over time in inverse barns, where $1\,\mathrm{barn} \equiv 10^{-24}\,\mathrm{cm}^2$. Usually smaller sudivisions are used such as inverse nanobarns (nb^{-1}) or inverse picobarns (pb^{-1}). In LEP the luminosity is measured by counting the number of small angle bhabha events in a region with accurately known acceptance. The choice of the process $\mathrm{e^+e^-} \to \mathrm{e^+e^-}$ is based on the fact that the cross-section for this reaction is known very accurately. The two forward detectors used in the luminosity measurement are:

- **Forward Detector** The detector consists of 35 sampling layers of lead-scintillator sandwich, separated in two basic modules: the presampler and the main calorimeter with 4 and 20 radiation lengths respectively. It is located at $\pm 2.6\,\mathrm{m}$ from the collision point and covers an acceptance of 40-150 mrad from the beam axis. Wavelength shifters are used to transfer the light to vacuum phototetrodes.

- **Silicon-Tungsten Luminometer** This detector is located at $z = \pm 2.4\,\mathrm{m}$ and covers a polar angle of 25-59 mrads from the beam axis. It consists of 19 layers of silicon detectors between 18 layers of tungsten. It provides better luminosity measurements than the forward detector due to the lower lateral spread of the showers in tungsten and the superior precision position resolution of the silicon detectors.

2.3 Monte Carlo Simulation

The Monte Carlo method is a numerical technique to simulate the outcome of a physics experiment, as predicted by the theory being tested. The output results can then be compared with the data recorded in the actual experiment, allowing a direct test of the theory. In particular physics this is typical done in two stages:

Generation of momentum four-vectors

Monte-Carlo methods are based on random-number generators: a series of random values are produced $r1$, $r2$, .. following a uniform distribution in the interval $(0, 1)$. The next step is to find a function θ(r) that is distributed according to a known f(θ), given that r follows a uniform distribution between 0 and 1. This is usually performed with numerical methods such as the Von Newman's acceptance-rejection technique [29]. If f(θ) is the angular distribution of a known physical process, event four vectors can be calculated based on the kinematic constraints.

Simulation of the detector

Given the generated event (the momentum of resulting particles), the same method is used to simulate the passage of particles through the several detector layers. This also involves random processes, such as the production of ionization, multiple Coulomb scattering etc. For example, if the random process is causing the deflection of the track according to a gaussian distribution around its momentum vector the same Monte-Carlo method is used to derive the angle of deflection with the use of random numbers [29]. Accurate detector modelling is a crucial part of each experiment to allow proper understanding of the data collected.

A software package used in many particle physics experiments and used by all LEP collaborations is GEANT [30]. This program can describe complex detectors such as OPAL, provided that the geometry and type of materials are given as input. GEANT is used within GOPAL [31] software package (Geant at OPAL). The output produced are the simulated signals induced in the readout of each subdetector. The reconstruction software ROPE [32] can treat this information as real data to produce Monte-Carlo events which are stored as DST tapes for offline physics analysis.

2.4 Data Acquisition

- **Trigger system**

  Bunches of positrons and electrons collide at LEP every $22\,\mu$s giving a possible event rate of 45 kHz. In order to make it feasible to store all this information a fast selection takes place to reduce the event rate to 10 Hz. The decision is taken in real time by a flexible and programmable system based on information delivered from each subdetector or standalone signals. The 4π solid angle of the detector is divided into 6×24 bins in θ and ϕ respectively and most subdetectors provide trigger signals in this binning. The final trigger decision is based on correlations in space between subdetectors in $\theta - \phi$ together with standalone signals triggered by total energy sums or track counting. The interesting physics events are triggered by more than one independent trigger condition, giving a redundancy to the system which leads to a high efficiency. Backgrounds from cosmic rays or interactions of the beam with the gas in the pipe or the pipe wall and noise are significantly suppressed.

- **Event builder, Filter and Event reconstruction**

  When a potentially interesting event is selected by the trigger system, information from the different subdetectors is read out as subevent structures. These are assembled by the event builder processor and passed to the filter system. A fast analysis is carried out by the filter processor where events are classified into basic categories (multihadron, dilepton etc) and background events are rejected. The next step in this sequence is the full reconstruction process where the events in the form of raw data are passed as input to the ROPE (Reconstruction of Opal Events) software package. Information from a calibration database (OPCAL) is used together with the event data to calculate event quantities such as energy and momentum of clusters and tracks and identify particles. These results are stored in the Data Summary Tapes (DSTs) for further analysis.

Chapter 3

Flavour of LEP2 physics

During the years 1989-1995 LEP operated at a collision energy at or near the Z^0 mass. A large number of these events (about 17 x 10^6) were produced allowing precision tests of electroweak theory with unprecedented accuracy. Radiative electroweak corrections were established as an experimental fact and from the cross-section lineshape of the Z the number of neutrino species was constrained to 3 (on condition that $m_\nu < M_Z/2$). The top mass was measured indirectly by electroweak data to a value consistent with the direct measurement performed later at Fermilab. The Z mass is now known to $\pm$ 2.2 MeV which is an uncertainty of approximately one part in 5×10^4. After the summer of 1996 the copper radiofrequency cavities were gradually replaced by niobium superconducting cavities allowing the collision energy to reach and exceed W boson pair production threshold (161 GeV). The study of W pairs permitted a precise measurement of of the W mass (M_W) and the study of the non-abelian character of electroweak theory via the Triple Gauge Couplings (TGCs). This period known as LEP2 provided an excellent lab for new physics searches such as supersymmetric particles, the hypothetical Higgs particle and even exotic extra dimension theories [33]. In this chapter an attempt to give a flavour of some interesting parts of LEP2 physics is made. The last part referring to two fermion physics is more detailed as it introduces concepts useful in the tau and muon pair analysis that follows.

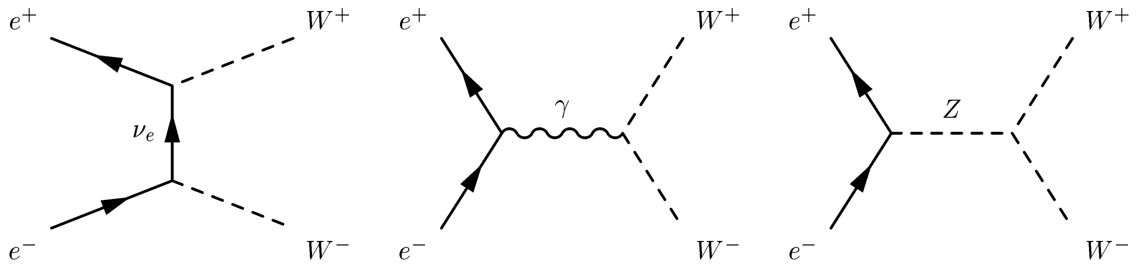

Figure 3.1: Feynman diagrams for W pair production: via t channel (left), s channel via a photon (middle), s channel via a Z boson (right).

3.1 W pair physics

W pairs are produced above the 161 GeV threshold via the s channel or the ν exchange t channel diagrams (figure 3.1). Each W boson can decay leptonicaly to a charged lepton and a neutrino or hadronically to a quark anti-quark pair with decay branching ratios of approximately 1/3 and 2/3 respectively. Thus the W pair events can be classified as:

- **Fully leptonic events** ($W^+W^- \rightarrow \mathrm{l}\nu\ l\nu$) The presence of neutrinos and the low branching ratio (1/9) reduces the impact of this channel on the W mass measurement M_W.
- **Semileptonic events** ($W^+W^- \rightarrow \mathrm{q\overline{q}}\ l\nu$) The experimental signature for these events is one lepton and two jets. Due to low backgrounds it is the ideal channel for extracting the W mass.
- **Fully hadronic** ($W^+W^- \rightarrow \mathrm{q\overline{q}\ q\overline{q}}$) It contains at least four jets and has significant irreducible backgrounds. There are no neutrinos in the final state so the momentum of the decay products is balanced.

3.1.1 Measurement of the W boson mass

The precise measurement of the W boson is one of the most important physics results of LEP2. This is due to the fact that when radiative corrections are taken into account, M_W depends quadratically on the mass of the top quark m_t and logarithmically on the Higgs mass M_H:

$$M_W = \frac{\pi\alpha}{\sqrt{2}\sin^2\theta_W}(1+\Delta\rho)$$

$$\Delta\rho = f(m_t^2, \log M_H) \tag{3.1}$$

where m_t is the top quark mass, $sin\theta_W$ is the weak mixing angle, $\Delta\rho$ is the radiative correction to the tree level cross-section ([34], [35]). This dependence allows a powerful test of the Standard Model as well as an indirect measurement of the Higgs mass. Two basic experimental methods were used to extract M_W by LEP collaborations [65]. In the first method the sensitivity of the inclusive cross-section to M_W is exploited at the threshold of W pair production. This method has the great advantage of small systematic uncertainties, but the reduced amount of data collected at this energy produced large statistical errors.

The most precise mass measurement is given by the direct reconstruction of M_W from its observed decay products, on an event by event basis. The mass by direct reconstruction of a quark-antiquark W decay is then:

$$M_{ij} = \sqrt{2E_iE_j(1-\cos\theta_{ij})} \tag{3.2}$$

where E_i, E_j are the jet energies, θ_{ij} is the jet-jet opening angle (the jet masses have been neglected here). The relatively poor jet energy resolution of the LEP detectors introduces large uncertainties. In an electron positron collider this problem can be

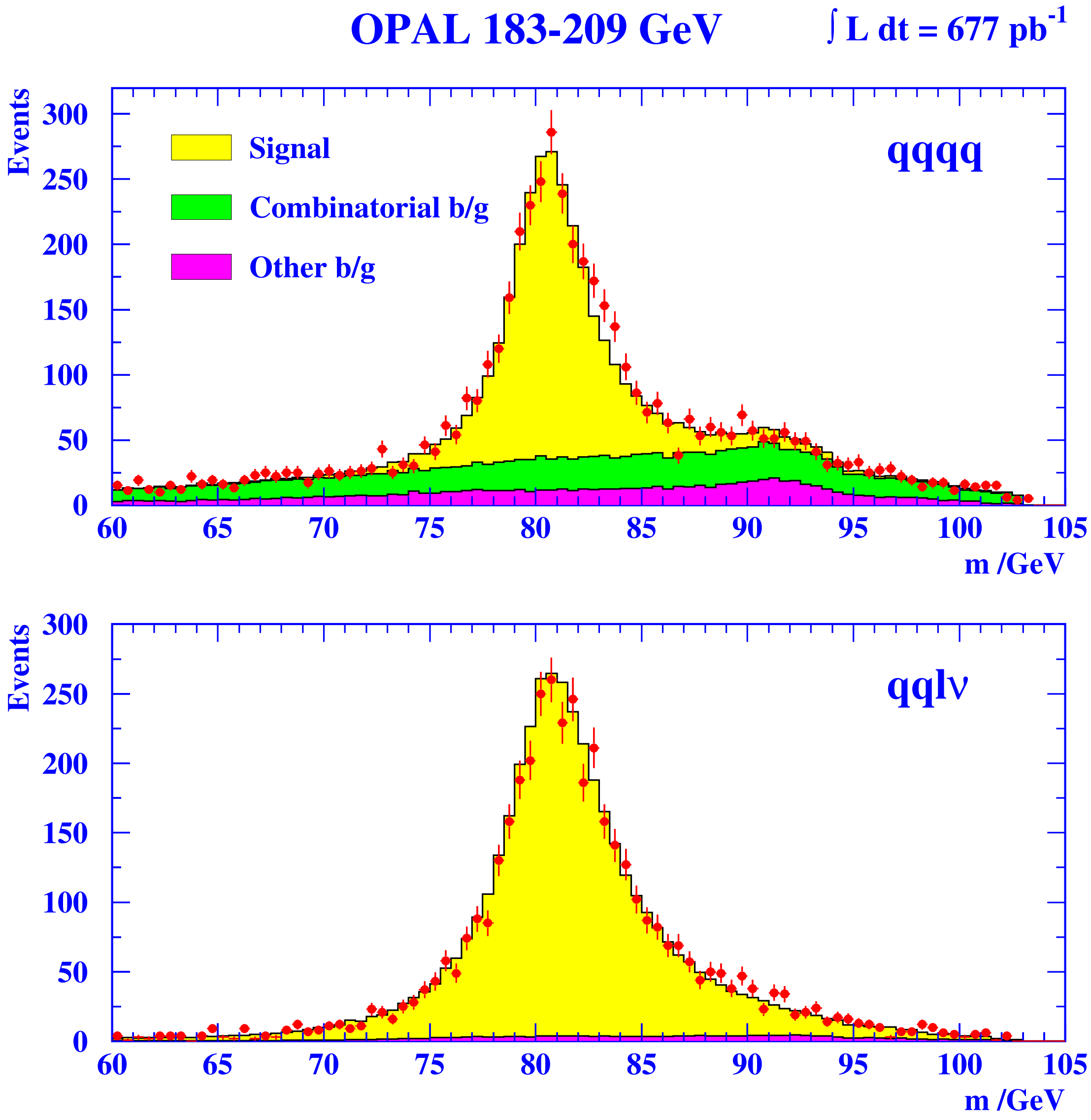

Figure 3.2: Distributions of the reconstructed W mass for all OPAL data from $\sqrt{s}$=183 GeV to 209 GeV. The points are data with statistical error bars, while the Standard Model expectation is indicated by the histogram [55].

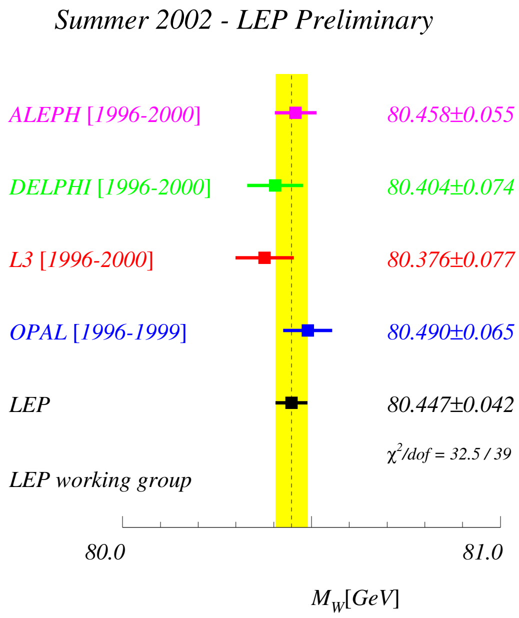

Figure 3.3: Combined results for the W mass measurement obtained by the four LEP collaborators [37] .

reduced by exploiting the knowledge of the collision $\sqrt{s}$ energy and energy-momentum conservation:

$$(E, \vec{p}) = (\sqrt{s}, 0) \tag{3.3}$$

giving four constraints. An additional constraint can be imposed by requiring the mass of the two reconstructed W bosons to be equal:

$$M_{W^+} = M_{W^-} \tag{3.4}$$

The mass resolution can be improved significantly by a kinematic fit: the measured parameters are varied until a solution is found which satisfies the imposed constraints and also minimizes the χ^2 difference between the measured and fitted values. Due to the neutrinos involved in the leptonic decays of W, the fully-leptonic channel has at least six unknown degrees of freedom and is therefore not very useful for measuring M_W. In the semi-leptonic channel the number of constraints in the kinematic fit is reduced by 3 due to the unknown momentum of the neutrino. The fully hadronic channel has the additional problem of how to associate jet pairs to W bosons in order to reconstruct each W boson. The radiation of a gluon can complicate things even more, and several analyses force some or all events to be reconstructed as five-jet events. The correct pair can be chosen as the one with the best kinematic fit.

M_W cannot be extracted by fitting simply an analytic Breit-Weigner function, due to Initial State Radiation (ISR) which decreases the collision energy to lower values than the ones already assumed in the kinematic fit and detector effects that distort the mass distribution. The kinematic fit which assumes the collision energy is equal to $\sqrt{s}$, overestimates M_W causing a tail towards higher invariant masses (figure 3.2). Detector effects must also be taken into account, as the resolution is not significantly better than the W boson width (Γ_W). To account for these effects an asymmetric Breit-Wigner function is used [36]. As there will in general be a bias introduced by this analytic fitting method, an explicit bias correction is applied based on a comparison of the Monte-Carlo value used for the W mass (M_W^{gen}) with the value obtained from the fit M_W^{fit}.

An alternative method in which biases are implicitly corrected involves a reweighting of Monte-Carlo events including simulation of the detector: A number of MC samples with different M_W and Γ_W are generated and the one which has the best χ^2 when compared with data can be chosen for a direct fit. The problem is then that the large number of MC samples needs unacceptable processing time. To overcome this limitation just one MC sample is generated with (M_W, Γ_W). A new MC sample with $(M_W^{new}, \Gamma_W^{new})$ is created by multiplying each event in the first sample by a factor which is the ratio of the matrix elements of M_W^{new} with respect to the M_W [39] :

$$\omega_i = \frac{|M_i(M_W^{new})|^2}{|M_i(M_W)|^2} \tag{3.5}$$

3.1.2 Test of the non-abelian couplings

A non-abelian local SU(2) invariant theory has a kinetic term of the form [5]:

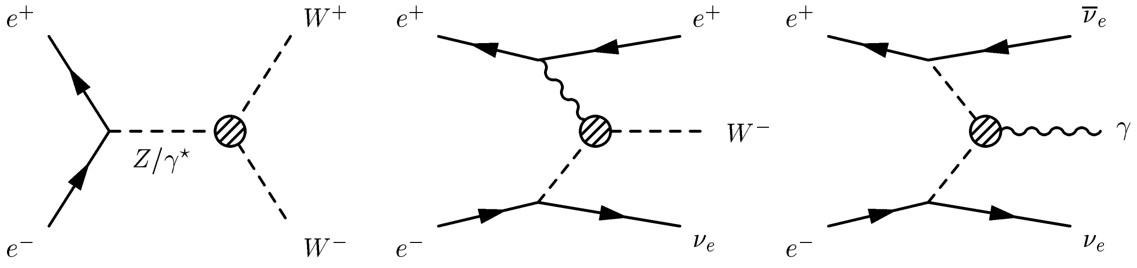

Figure 3.4: LEP2 processes sensitive to triple gauge couplings

$$
\begin{aligned}
\mathcal{L}^W = -\frac{1}{4}\vec{F^{\mu\nu}}\ \vec{F_{\mu\nu}} = -\frac{1}{2}\ (\partial_\mu \vec{W}_\nu - \partial_\nu \vec{W}_\mu)\ \partial^\mu \vec{W}^\nu \\
+g\ (\vec{W}_\mu \times \vec{W}_\nu)\ \partial^\mu \vec{W}^\nu \\
-\frac{1}{4}g^2\ [(\vec{W}_\mu\ \vec{W}^\mu)^2 - (\vec{W}_\mu\ \vec{W}_\nu)(\vec{W}^\mu\ \vec{W}^\nu)]
\end{aligned}
$$

Clearly the last two lines of this expression leads to three point vertices (trilinear gauge couplings or TGCs) and four point vertices (Quadratic gauge couplings). These interactions originate from the kinetic part of the Lagrangian and exist even in the absence of matter fields. Thus, self interactions of the gauge fields are a fundamental characteristic of non-abelian Yangs-Mills theories, such as the Standard Model. Absence of the Yangs-Mills form of triple gauge couplings would lead to the WW cross-section increasing with energy and eventually violating unitarity. The measurement of the WW cross-section provides evidence for the non-abelian character of electroweak interactions as it is can be seen by figure 3.5. The W production angular distribution is also sensitive to deviations from the standard couplings (called anomalous couplings). The LEP2 processes which are sensitive to TGCs can be seen in figure 3.4. There are seven possible Lorentz invariant couplings for each WWV vertex, where V can be a photon or a Z [35]. As it is impossible experimentally with LEP data to measure all these couplings, symmetry constraints are usually imposed: gauge invariance, C, P and CP conservation reduce the possible couplings to five and these are usually denoted as $\kappa_\gamma, \kappa_z, \lambda_\gamma, \lambda_z, g_z^1$. The SM predicts that the value of these parameters are [65]:

$$\kappa_\gamma = \kappa_z = g_z^1 = 1 \qquad \lambda_\gamma = \lambda_z = 0$$

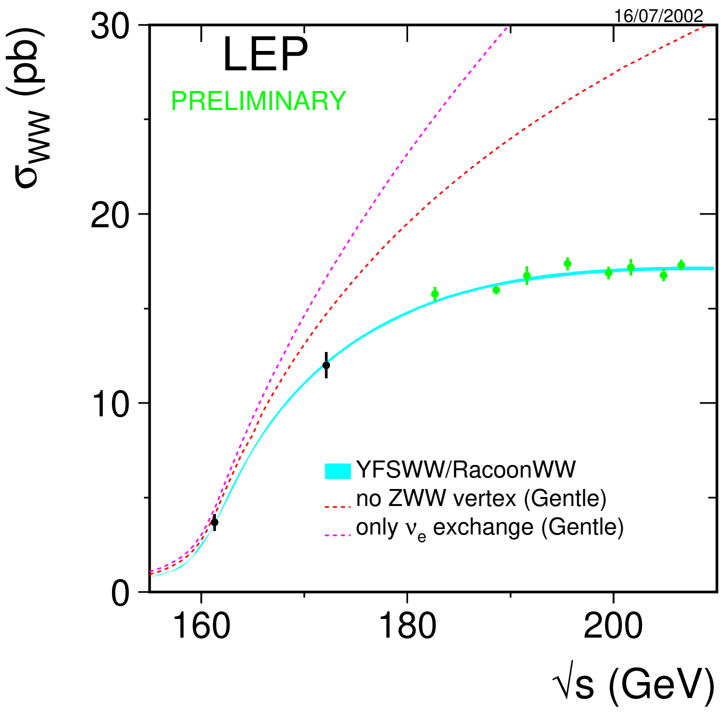

Figure 3.5: The LEP combined results for the WW cross-section as a function of the energy [40]. The solid curve shows the Standard Model prediction and the other two lines the effect of removing the TGC diagrams.

No significant deviation from the Standard Model prediction is seen for any of the electroweak TGCs studied [38].

3.2 Higgs boson search

The Weinberg-Salam $SU_L(2) \times U_Y(1)$ electroweak model has impressive experimental confirmation over the last 25 years. Precision measurements performed in LEP and SLD established the success of the model beyond the tree level diagrams. The only missing particle not yet experimentaly verified remains the hypothetical Higgs particle, responsible for the electroweak symmetry breaking. The dominant production

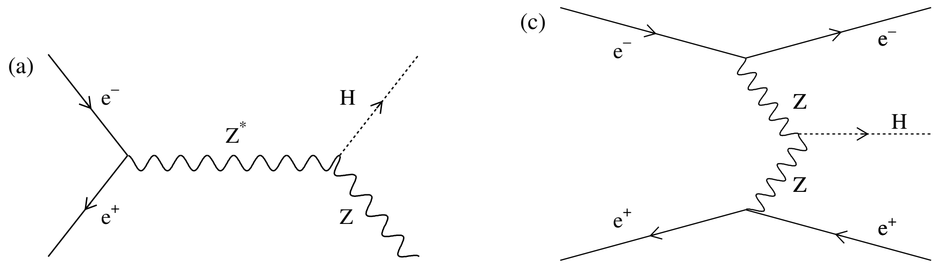

Figure 3.6: Higgs production through Higgstrahlung (left) or Weak boson fusion (right)

processes at LEP2 energies are Higgstrahlung or Weak boson fusion (figure 3.6). The Higgstrahlung diagram dominates when on shell Z production is kinematically allowed ($m_H < \sqrt{s} - M_Z$). For a hypothetical mass of m_H=115 GeV Higgs decays predominantly to a b$\overline{\text{b}}$ pair with a branching ratio of approximately 74%, gluons ($\sim$ 7%), W pair ($\sim$ 8%) or a tau pair ($\sim$ 7%), leading to the following search topologies [42], [65]:

- **Four jet channel ($H \rightarrow \text{b}\overline{\text{b}}, Z \rightarrow \text{q}\overline{\text{q}}$)**

  This topology arises when the Z decays into a quark-antiquark pair and the Higgs into a b$\overline{\text{b}}$ representing 60% of the Higgs production cross-section. It suffers from a large irreducible background arising from hadronic decays of W and Z pair production. A kinematic fit is used to improve the energy resolution.

- **Missing energy channel ($H \rightarrow \text{b}\overline{\text{b}}, Z \rightarrow \nu\nu$)**

  In this channel the Z decays into neutrinos leading to an acoplanar pair of b-quark jets and large missing energy close to M_Z.

- **Leptonic channel ($H \rightarrow \text{b}\overline{\text{b}}, Z \rightarrow ll$)**

  This process is characterised by the presence of a high mass pair of isolated and well identified charged leptons (electrons or muons) together with 2 jets arising from the Higgs decay.

- **Tau channels ($H \rightarrow \text{b}\overline{\text{b}}$ $(\tau^+\tau^-), Z \rightarrow \tau^+\tau^-(\text{q}\overline{\text{q}})$**

  The experimental signature for this channel is a pair of well collimated tau jets associated to a high multiplicity hadronic system.

The interpretation of the results is performed with the help of a binned likelihood statistical test. More specifically the reconstructed mass M_H is divided into bins with $s_i(M_H)$ the predicted signal events in bin i for a M_H Higgs hypothesis and b_i the expected background. Two different likelihoods are constructed one for the signal+background hypothesis and the other for background only. The probability for observing n_i events in bin i is assumed to be poissonian. The likelihood functions are:

$$\mathcal{L}_{signal+background} = \prod_i \frac{(s_i + b_i)^{n_i} \; e^{-(s_i+b_i)}}{n_i!}$$

$$\mathcal{L}_{background} = \prod_i \frac{b_i^{n_i} \; e^{-b_i}}{n_i!}$$

The two likelihoods are then compared by taking the logarithm of their ratio:

$$-2 \; \ln Q(M_H) = -2 \ln \; \frac{\mathcal{L}_{signal+background}}{\mathcal{L}_{background}}$$

This likelihood ratio can be seen in figure 3.7 and the measure of inconsistency with the background hypothesis in figure 3.8. There is an excess of events consistent with a signal of 115 GeV but the statistical significance is only 2.1 σ, consistent with background hypothesis too. Experiments at the Large Hadron Collider are expected to give definitive results on the nature of symmetry breaking mechanism.

3.3 Supersymmetric Searches

As already mentioned in chapter 1, supersymmetry has many nice features and many theorists believe that it is realized somewhere in nature. The question is then how. The Minimal Supersymmetric extension to the Standard Model (MSSM) predicts that

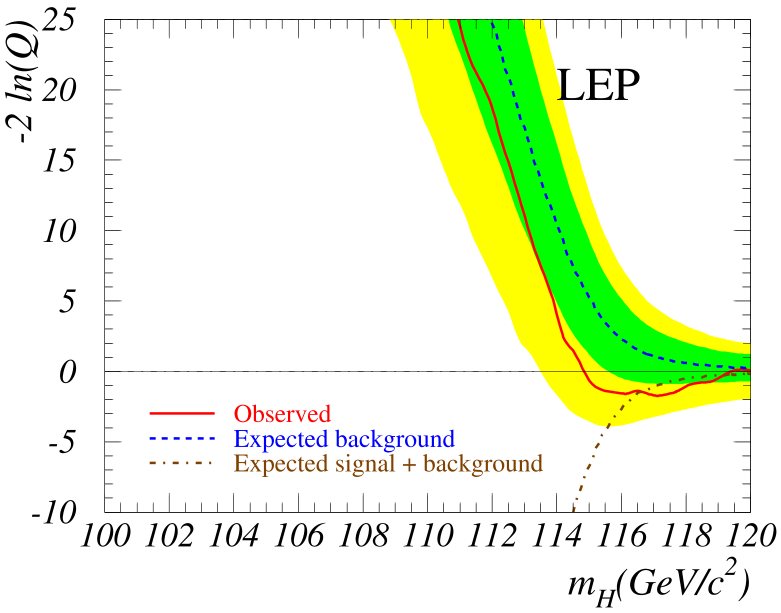

Figure 3.7: Observed and expected behavior of the test-statistics -2 lnQ as a function of the test-mass m_H, obtained by combining data of all four LEP experiments [41].

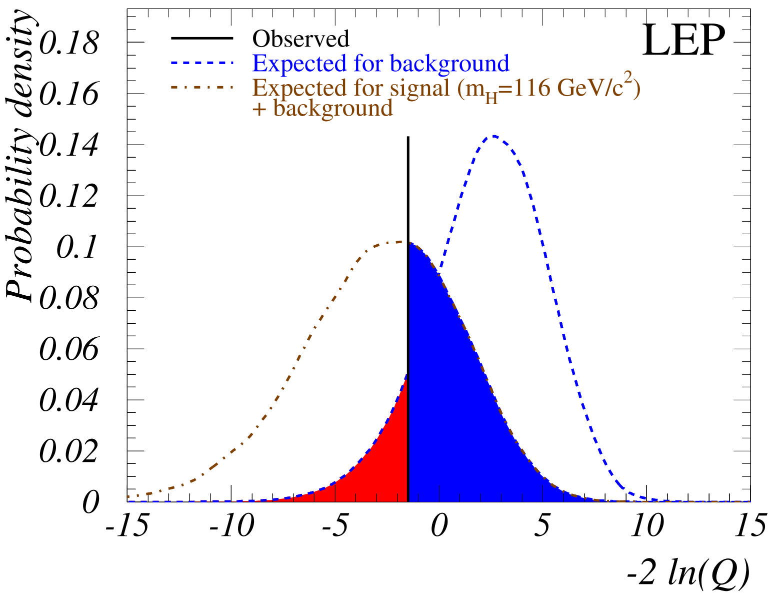

Figure 3.8: Probability density functions for a fixed test mass m_H=116 GeV , for the background and the signal+background hypotheses. The observed test-statistic -2lnQ is indicated by the vertical line. The red (light shaded area measures the combatibility with the background hypothesis and the blue (dark) shaded area with the signal+background hypotheses [41].

each SM particle has one superpartner [65]. The superpartners of gauge bosons (gauginos) have spin 1/2, the partners of fermions (sfermions) have spin 0, and the partners of Higgs (Higgsinos) have spin 1/2. The Higgs sector contains 2 doublets, with $\tan\beta = v2/v1$ the ratio of their vacuum expectation values. The fact that we do not observe selectrons with mass equal to electrons means that supersymmetry is broken. Several models attempt to describe the nature of the symmetry breaking mechanism. The physical mass eigenstates are derived by mixing the Higgsinos and gauginos to give two charged fermions $\tilde{\chi}_i^{\pm}, i = 1, 2$ (charginos) and four neutral fermions $\tilde{\chi}_i^0, i = 1, ..4$ (neutralinos). The conservation of Baryon and Lepton number introduces a new quantum number called R-parity $Rp = (-1)^{3B+L+2S}$. Assuming that R-parity is conserved implies that supersymmetric particles are produced in pairs and that the lightest one (Lightest Supersymmetric Particle or LSP) is stable. Some typical searches can be classified as:

- **Chargino searches** ($\tilde{\chi}_1^{\pm}, \tilde{\chi}_2^{\pm}, m_{\chi_1} < m_{\chi_2}$)

  In the electron positron collisions they are produced in pairs via γ and Z exchange in the s-channel and via $\tilde{\nu}_e$-exchange in the t-channel. The experimental signatures depend on the mass difference between $\tilde{\chi}_1^{\pm}$ and the LSP [65]. For example $\tilde{\chi}_1^{\pm} \to \tilde{\chi}_1^0 \mathrm{l}^{\pm}\nu$ via W boson leads to two acoplanar leptons.

- **Neutralino searches** ($\tilde{\chi}_1^0, \tilde{\chi}_2^0$)

  A thorough study of $\mathrm{e}^+\mathrm{e}^- \to \tilde{\chi}_1^0\tilde{\chi}_2^0$ needs to take into account all posible $\tilde{\chi}_2^0$ decays via a Z boson. For example $\tilde{\chi}_2^0 \to \tilde{\chi}_1^0\ l^+l^-$ or $\tilde{\chi}_2^0 \to \tilde{\chi}_1^0\mathrm{q}\overline{\mathrm{q}}$ leading to two acoplanar leptons or jets and missing momentum from the two undetected $\tilde{\chi}_1^0$'s.

- **Slepton searches**

  Each SM charged lepton l has two scalar partners called right $\tilde{l}_R$ and left $\tilde{l}_L$ sleptons. Charged scalar leptons are pair produced $\mathrm{e}^+\mathrm{e}^- \to \tilde{l}^+\ \tilde{l}^-$ and $\tilde{l}^+\ \tilde{l}^-$ can decay into $\tilde{l}^{\pm} \to l^{\pm}\tilde{\chi}_1^0$ leading to two acoplanar leptons and missing energy.

- **Squark searches**

  The main production process is $e^+e^- \rightarrow \tilde{q}\bar{\tilde{q}}$ followed by $\tilde{q} \rightarrow q\tilde{\chi}_1^0$ where $\tilde{\chi}_1^0$ is the lightest neutralino. The experimental signature is acoplanar jets with large missing energy in hadronic events.

  There are many supersymmetry models with different symmetry breaking mechanisms leading to a large number of possible searches. There are more than 100 free parameters making many of these models under-constrained. Experimental input is necessary to choose the one that describes nature (if any) in contrast with the Standard Model which made remarkable predictions for the gauge boson masses and had fewer free parameters.

3.4 Fermion pair physics

The production of fermion pairs is one of the basic processes of the Standard Model. It is described by the exchange of a photon or Z in the s-channel. Due to the fact that the final state is identical to the initial one the bhabha scattering process takes place also in the t-channel (figure 3.9).

The experimental precision of the full LEP2 data set allows new physics processes to be investigated in these final states. The differential cross-section is given by:

$$\frac{\mathrm{d}\sigma}{\mathrm{d}\Omega} = |\gamma_s + Z_s + (\gamma_t + Z_t)_{bhabhas} + NewPhysics?|^2$$

where $\gamma_{s/t}, \mathrm{Z}_{s/t}$ are the photon and Z amplitudes in the s/t channels. The last term refers to the following searches for new physics including:

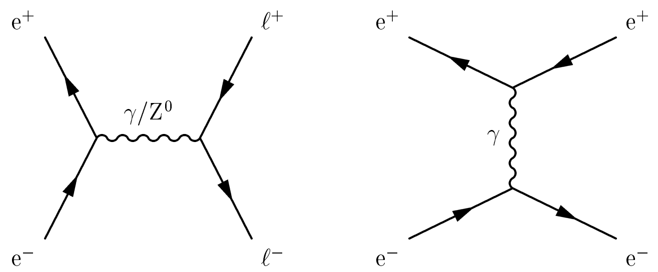

Figure 3.9: Feynman diagrams for fermion pair production: via s channel (left) and t channel (right)

3.4.1 Contact interactions

Contact interactions refer to a very general framework to search for new physics, from $e^+e^-\to f\bar{f}$ data. For example we can look for another deeper level of substructure in quarks and leptons [16], [44] or exchange of new heavy particles, assuming an effective Lagrangian similar to the one used by Fermi to describe nuclear beta decay (weak force) [54]:

$$\mathcal{L}^{contact} = \frac{g^2}{(1+\delta)\Lambda^2} \sum_{i,j=L,R} \eta_{ij}[e_i\gamma^\mu e_i][f_j\gamma^\mu f_j]$$

where $\delta = 1$ for bhabhas and 0 otherwise, $e_L(f_L)$ and $e_R(f_R)$ are chirality projections, Λ the new physics energy scale and g the unknown coupling. The η_{ij} are parameters with values ± 1, 0 depending on the vector or axial-vector character of the specific model. The Standard Model cross-section decreases like s^{-1} while the contact interactions would grow with s (as in the old Fermi theory). Limits on the energy scale or signal for new physics can be extracted by fitting the angular distributions for the leptons or the hadronic cross-sections.

3.4.2 Limits on $Z^{'}$ boson

The hadronic and leptonic cross-sections and the leptonic asymmetries were used to fit data to models including an additional heavy neutral Z boson. This originates from Grand Unified Theories (GUT's) where the Standard Model $SU_C(3) \times SU_L(2) \times U_Y(1)$ arises from a master group like E(6), SU(5),.. etc. The master group breaks via a Higgs mechanism to the S.M, in a similar way the S.M breaks into $SU_C(3) \times U_Q(1)$. For example in E(6) theory two additional gauge groups $U_\chi(1)$ and $U_\psi(1)$ are introduced [46], [54], each related to a new gauge boson χ, ψ, respectively. The new $Z^{0'}$ can be any mixture of χ, ψ. The observed particles are the Z $Z^{'}$ resulting from the mixture of the SM Z^0 and $Z^{0'}$. The mass of the $Z^{'}$ and the mixing angle Θ_M are free parameters. The exchange of $Z^{'}$ in fermions pairs can change the measured cross-sections and asymmetries. The χ^2 between the prediction of the models and data is used to constrain these models.

3.4.3 Constraints on Low Scale Gravity

The difference of many orders of magnitude between the two fundamental physics scales is a puzzle for physicists: The electroweak scale ($M_{EW} = 10^2$ GeV) and the energy where gravity becames important known as the Planck scale M_{Pl} ($M_{Pl} = 10^{19}$ GeV), have a ratio of about 10^{-17} (hierarchy problem). A new model has been proposed that attempts to explain this puzzle [33]. According to this, gravity is propagating to extra 'large' compact dimensions, while the rest of gauge interactions are confined to the usual space-time. Kaluza and Klein have introduced tiny compact dimensions as early as 1927 [45]. The Planck mass in $D = n + 4$ dimensions (M_D) is assumed to be at the electroweak scale, so the M_{Pl} in the usual space time is:

$$M_{Pl} = R^n M_D^{n+2}, \tag{3.6}$$

where R is the compactification radius of extra dimensions. By choosing $M_D \sim M_{EW}$ we can solve equation 3.6 for R, allowing the number of extra dimensions to be from

$n = 2$ up to 7 (constrained by D_{MAX}=11 predicted by superstring theory). The value $n = 1$ is excluded experimentaly as gravity would be modified at solar system distances, but for $n = 2$ the model predicts $R \sim \mathcal{O}(1\,\mathrm{mm})$ which is not excluded. Such a theory could modify the 2-fermions cross-section via the process $\mathrm{e^+e^-} \rightarrow G^* \rightarrow \mathrm{f\bar{f}}$, where G^* is the hypothetical gravity quantum. The theory is parametrized in a similar way to the contact interactions (but including terms in the cross-section proportional to $\cos\theta$) and fits to muon, tau, electron pairs angular distributions are used to constrain the theory [47].

Chapter 4

Tau pairs Analysis

4.1 Introduction

The analysis of the tau pairs process $e^+e^- \rightarrow \tau^-\tau^+(\gamma)$ presented in this chapter includes all the high energy data collected by OPAL during the last two years of operation (1999-2000), at energies 192-209 GeV. Taus are produced back-to-back in the centre of mass frame and decay via weak interactions to leptons or hadrons.

The most important experimental characteristic of two fermion physics at LEP2 is the frequent emission of one or more initial state radiation photons (ISR), which complicates the definition of centre of mass energy and signal and efficiency of the selection. Initially, the estimation of the effective centre of mass energy is presented. The selection of tau pairs which is an evolution of the one used at lower energies is then described ([48], [49], [50], [51]). Then the description of the background processes and the complications to the efficiency due to initial state radiation are discussed. Finally, the Monte-Carlo estimations for the background and efficiencies are described followed by the results and systematic checks.

4.1.1 The effective centre of mass energy $\sqrt{s'}$

The emission of one or more photons by the beam particles (ISR), enhances significantly the two fermion cross-sections, as can be seen by the $\mu^+\mu^-$ cross-section (figure 4.1). The radiation of a hard photon decreases the centre of mass energy and as the cross-section peaks at the Z pole, collisions are more likely for events with this energy. This process is called radiative Z -return and causes a large portion of two fermion events to be clustered around $m_{\mathrm{f\bar{f}}} = M_{\mathrm{Z}}$. The definition of the reduced centre of mass energy $\sqrt{s'}$ is complicated by the fact that Final State Radiation (FSR) cannot be cleanly separated from ISR since ISR-FSR photon interference terms are not negligible at LEP2 energies.

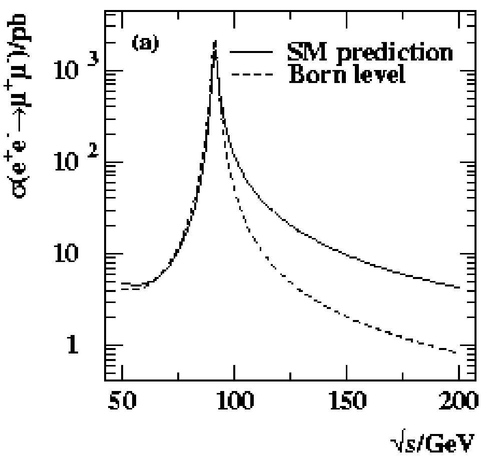

Figure 4.1: The $\mu^+\mu^-$ cross-section as predicted by Standard Model (including radiative terms) and at Born level (excluding corrections)

The effective collision energy $\sqrt{s'}$ is defined as the mass of the s-channel propagator. The ISR-FSR interference is subtracted to make the propagator mass unambiguous. The most interesting events in terms of new physics searches are collisions at full energy. This is the reason for studying the events with $s'/s > 0.7225$ as the 'non-radiative' data sample, where s is the centre of mass energy. The inclusive events are all events with $s'/s > 0.01$. The experimental determination of $\sqrt{s'}$ is based on the the polar angles of the detected particles. The measurement of θ is based on combining both tracking

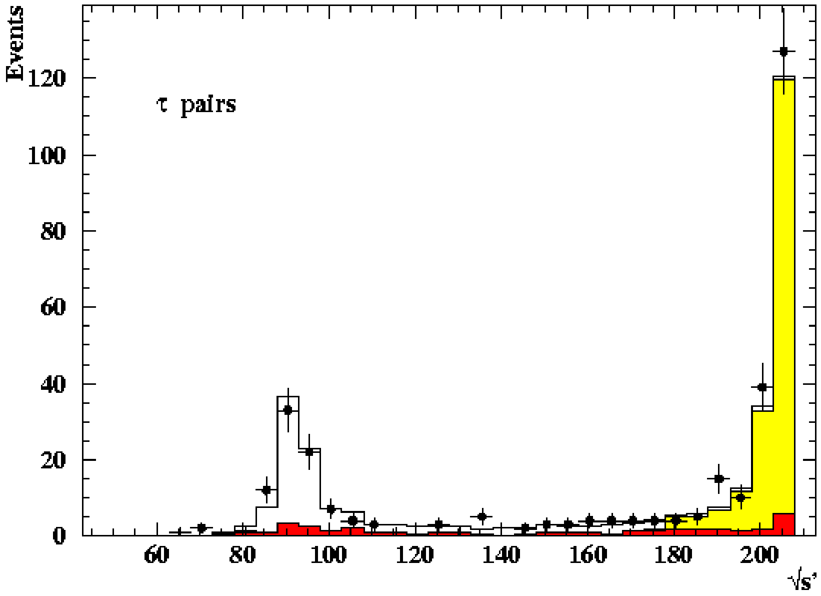

Figure 4.2: The $\sqrt{s'}$ distribution for tau pairs at 206 GeV. The open histogram is the Monte-Carlo prediction, the yellow(lightgrey) histogram is the prediction for non-radiative events and the red (dark grey) is the background contamination. The points are data.

and electromagnetic calorimeter clusters inside each tau cone of 35 ° (section 4.2.2).

In all events where no high energy photon is detected, a single ISR photon is assumed to have been emitted along the beam axis without being detected. The energy of such a photon E_γ and the equivalent $\sqrt{s'}$ are then given by:

$$E_\gamma = \sqrt{s}\ \frac{|\sin(\theta 1 + \theta 2)|}{\sin\theta 1 + \sin\theta 2 + |\sin(\theta 1 + \theta 2)|} \tag{4.1}$$

$$\sqrt{s'} = \sqrt{s\ - 2\ E_\gamma \sqrt{s}} \tag{4.2}$$

where $\theta 1$, $\theta 2$ are the directions of the two charged cones as measured by using both clusters and tracks.

If there is a photon (neutral cone) detected in the electromagnetic calorimeter with $E_\gamma > 30\,\text{GeV}$ in addition to the two tau cones and the event is planar (the sum of all angles between the 3 particles is greater than 358 °), then the $\sqrt{s'}$ is derived from 3-body massless kinematics, assuming that the photon is from initial state radiation (ISR) [52]. The planarity is necessary to ensure that all particles are detected in the event. The assumption that the detected photon is due to ISR is based on the fact that final state photons are predominantly within the charged cones. The energy of the photon is estimated as :

$$E_\gamma = \sqrt{s}\,\frac{|\sin\theta 3|}{\sin\theta 1 + \sin\theta 2 + |\sin(\theta 1 + \theta 2)|} \tag{4.3}$$

where $\theta 3$ is the polar angle of the most energetic neutral cone. The $\sqrt{s'}$ distribution for tau pairs at 206 GeV is plotted in figure 4.2. For quality checks the the $\sqrt{s'}$ region was split into three energetic regions:

- **The** Z **region:** from $0.01 < s^{'}/s$ up to $\sqrt{s'} < 110$ GeV
- **The intermediate region:** from 110 GeV< $\sqrt{s'}$ up to $s^{'}/s < 0.7225$
- **The non-radiative region:** with $s^{'}/s > 0.7225$

The correlation between the reconstructed $\sqrt{s'}$ and the true (generated) $\sqrt{s'}_{true}$ is reasonably good as can be seen in figure 4.3 for a sample of Monte Carlo tau pair events generated at $\sqrt{s} = 206\,\text{GeV}$. The reconstructed collision energy is higher for radiative events where both electron and positron emit a photon resulting to more back-to-back events compared with single photon radiation. The correlation between the reconstructed and generated $\sqrt{s'}$ for the planar candidates when the energetic detected photon is taken into account is clearly improved as can be seen in figure 4.4.

In a small fraction of collisions the emission of an ISR photon from both of the colliding particles can result in a back to back event. In this case the reconstructed

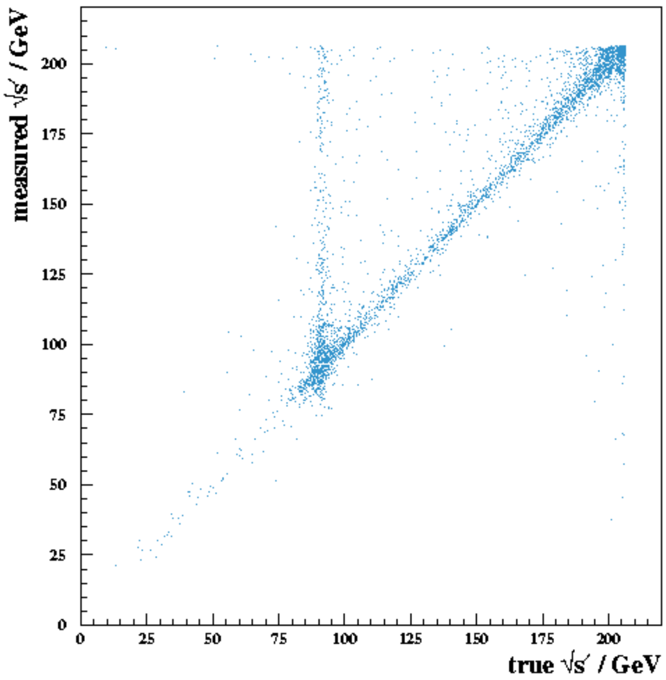

Figure 4.3: The correlation between the reconstructed $\sqrt{s'}$ and the true (generated) $\sqrt{s'}_{true}$ for a sample of Monte Carlo tau pair events generated at $\sqrt{s} = 206\,\mathrm{GeV}$.

collision energy is overestimated and the events are falsely considered as non-radiative. These are called feedthrough events and are treated like a background in the non-radiative sample. An undetected FSR photon can also change the momentum of the τ lepton leading to an underestimation or overestimation of $\sqrt{s'}$.

4.2 Selection of tau pairs

Taus are heavy leptons with an average lifetime of $\sim 219\ fs$ and the only ones that can decay via weak interaction not only leptonically but also hadronically, having at least one neutrino in the final state. The tau pairs are produced back-to-back, unless there is photon radiation. Where an initial state photon is emitted (ISR), the centre of mass of the tau pairs is boosted, but the event remains back-to-back in the rest frame of the Z particle, unless final state radiation occurs (FSR).

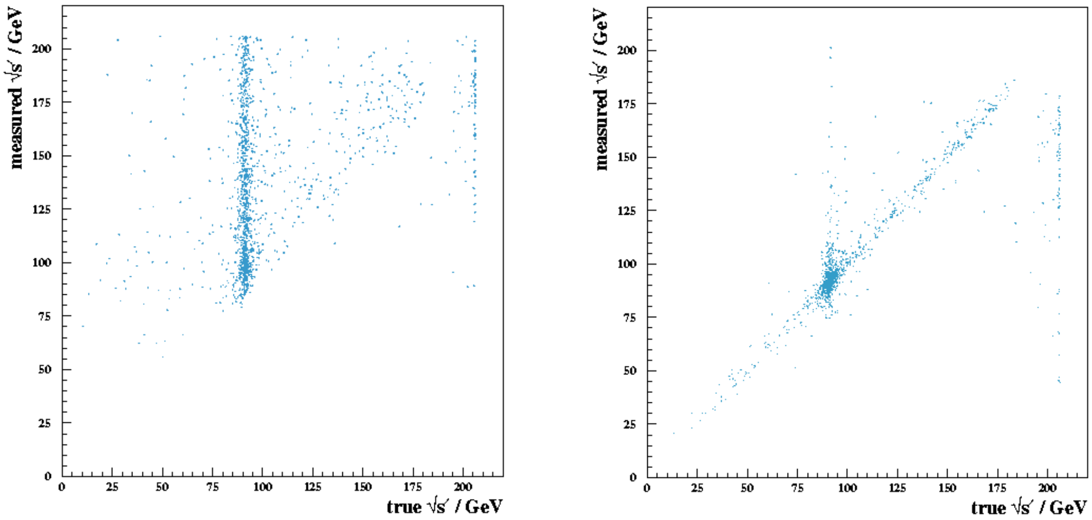

Figure 4.4: The correlation between the reconstructed $\sqrt{s'}$ and the true (generated) $\sqrt{s'}_{true}$ for planar events with an energetic photon when the photon is not taken into account (left), and when it is used for $\sqrt{s'}$ calculation (right). The sample of Monte Carlo tau pair events was generated at $\sqrt{s} = 206\,\mathrm{GeV}$.

The conservation of charge implies that tau can decay to either one charged lepton or to an odd number n (called 'n-prongs') of charged mesons like pions and kaons. In the hadronic decays the quarks are hadronized to form narrow jets. The selection of tau pairs is based on a jet-finding algorithm, which associates tracks and electromagnetic calorimeter clusters that lie inside cones of half-angle of 35°. The neutrino(s) produced complicate further the study of tau pairs as they cannot be detected. The missing energy in the tau cones means that energy-momentum conservation cannot be used as a constraint, making the selection far from difficult than for other lepton or quark-antiquark pairs at LEP. The detected energy for tau pairs (also called visible energy), has a range from high to low values, covering a big phase space occupied by many background processes.

4.2.1 Preselection

A preselection is applied before the tau pairs selection cuts in order to reduce the amount of non physics data recorded and ensure the quality of the tracks and calorimeter clusters reconstructed. An event is preselected if at least one of the following condition is satisfied [56]:

- There is at least one 'good' track which originates close to the collision point. This is ensured by requiring the closest approach of the track to the interaction point in the $r-\phi$ plane to be within a distance $|d0|$ less than 1 cm and z-coordinate $|z0|$ less than 50 cm. Aditionally at least 20 hits in the central detectors are required (CJ, CV, CZ) and the transverse track momentum with respect to the beam axis should be greater than 1.65% of the beam energy.
- There are at least two electromagnetic calorimeter clusters back-to-back within 25 °, one of which has total calorimeter energy greater than 15% of the beam energy, or two clusters with energy deposit greater than 15% of the beam energy.
- There is a track in the Muon Endcap (ME) detector which when extrapolated back to the collision point has a distance of less than 20 cm from the beam spot when measured at $z = 0$ plane. Only events containing 4 or less such tracks are considered.

In addition a loose veto is applied to reduce the multihadronic events originating from final states containing quarks such as the two fermion process $e^+e^- \to q\overline{q}$. These events can be substantially removed by requiring the total number of tracks and electromagnetic calorimeter clusters to be less than 18. After the preselection most of the multihadronic background and non-physics events originating from the interactions of the beam with the gas or the beam wall, are removed leaving dominantly a dilepton data sample.

4.2.2 Multiplicity cuts

In addition to the high multiplicity veto applied in the general preselection of lepton pairs a tighter cut is applied in the tau selection to reduce further the hadronic background. This is necessary as taus are the only leptons pairs that decay into hadrons and the data sample is more sensitive to contamination from quark-antiquark pairs. The tighter multiplicity cut requires that the total number of tracks is less than 7 and the number of tracks and electromagnetic calorimeter clusters is less than 16.

As already mentioned, the study of a tau candidate is based on a cone algorithm. More specifically starting from the most energetic track or cluster, a cone of half angle 35° is searched. If new tracks or clusters are found, a new direction is calculated by adding vectorially the initial track/cluster to the next most energetic track/cluster found within the cone. The process is repeated until no more tracks or clusters are found. The algorithm then looks for other cones, starting from the most energetic track or cluster outside the cone(s) already found. Cones with total net charge equal to zero are characterized as neutral cones. The number of charged cones is required to be exactly two.

4.2.3 Event Vetos

Cosmic veto

Events produced in e^+e^- collisions originate close to the beam crossing, in contrast with cosmic rays which are distributed uniformly over all the detector volume. In addition, collision events are in time coincidence with the beam-crossings. Cosmic rays can be strongly suppressed by imposing space-time constraints based on Time-Of-Flight (TOF) measurements and vertex cuts. In the barrel region for events with at least one TOF measurement, the smallest absolute time recorded must be within 10 ns of the expected time-of-flight of a particle travelling at the speed of light and originating at the vertex. For events with two back-to-back TOF measurements there is an additional requirement: the difference between the two counters is required to be less than 8 ns. For events in the barrel with no TOF measurements, tight vertex constraints are imposed:

$$|\sum z0| < 10\,\mathrm{cm}, \sum |d0| < 0.08\,\mathrm{cm}$$

where $|d0|, z0$ are the distance and z-coordinate of point of closest approach of the track to the collision point. The latter is found by extrapolating the track to the $r - \phi$ plane that includes the interaction point. For events in the endcap region due to poorer position resolution looser vertex cuts are applied:

$$|\sum z0| < 50\,\mathrm{cm}, \sum |d0| < 1.5\,\mathrm{cm}$$

Finally, constraints are also imposed on the minimum $|d0|$ and average $z0$ of the event:

$$|d0_{min}| < 0.5\,\mathrm{cm}, z0_{avr} < 20\,\mathrm{cm}$$

Other event vetoes

Events with two electrons represent a large percentage of background as they predominantly originate from bhabha scattering or two photon $\mathrm{e^+e^-} \rightarrow \mathrm{e^+e^-e^+e^-}$ untagged events. The identification of the electron can be based on the comparison of its calorimeter energy and track momentum: if the calorimeter and the track measurements are reliable, they should be similar. As the measurement resolution is poorer at large $\cos\theta$ for the central tracking detectors, the ratio of the calorimeter cone energy E to the track momentum P, can be significantly different from unity. The dependence of the E/P ratio on $\cos\theta$ angle for a Monte-Carlo sample generated at 206 GeV for the process $e^+e^- \rightarrow e^+e^-$ (bhabhas) can be seen in figure 4.5. To account for the $cos\theta$ dependence, a different selection range is used for the E/P ratio in the barrel, endcaps and the overlap region between these two as listed in table 4.1. Events with two electrons identified by these E/P selections are rejected.

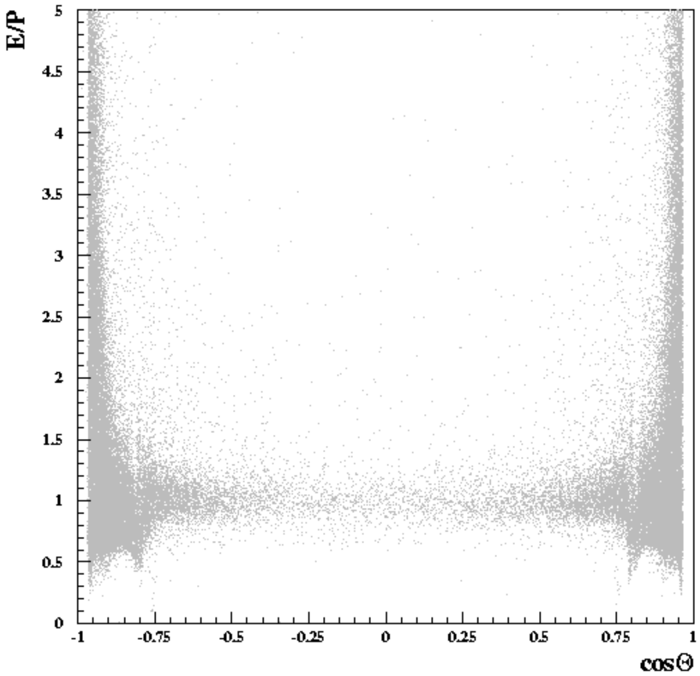

Figure 4.5: E/P distribution versus $\cos\theta$ before selection is applied for bhabha Monte-Carlo events generated at 206 GeV.The polar angle is measured from the tracking information.

Region	polar coverage	E/P range
Barrel	$cos\theta < 0.79$	$0.7 < E/P < 1.3$
Overlap	$0.79 < cos\theta < 0.815$	$0.5 < E/P < 1.5$
Endcap	$0.815 < cos\theta$	$0.7 < E/P < 1.5$

Table 4.1: polar range of electron E/P veto.

Due to the importance of the electron pair veto, it was attempted to improve it further by using the hadronic calorimeter information. More specifically, an event can also be identified as an electron if it is not a muon and has no significant hadronic energy deposit. The new definition in addition to the E/P veto can suppress to almost zero the backgound from two photon process $e^+e^- \to e^+e^-e^+e^-$ and decrease the bhabhas significantly, with a few percent loss in the efficiency. However, in the final selection it was decided to use only the E/P veto, as it was desirable to move towards higher efficiency in the efficiency-purity plane and the Monte-Carlo simulation of the hadronic calorimeter is less precise than that of the electromagnetic calorimeter.

Events that satisfy the standard LEP2 muon pairs selection as presented in the next chapter are also rejected and as the collision energy is above WW threshold the standard OPAL WW veto [57] is also applied.

4.2.4 Visible, expected and missing energy

Visible energy

The total energy detected in the electromagnetic calorimeter scaled to the collision energy $Rshw$ and the corresponding quantity for the total track momentum $Rtrk$ are important observables for this analysis: due to neutrino emission, tau pairs are fairly uniformly distributed in the $Rshw$, $Rtrk$ plane. In contrast, background bhabha, two photon and muon pair events occupy specific regions of the plane and can be suppressed by cuts on these variables.

More specifically, the bhabhas are very likely to have large momentum tracks and large energy deposits in the electromagnetic calorimeter. The visible energy $Rvis$, defined as the sum of $Rshw$ and $Rtrk$, is required to be less than 1.1 to reduce the bhabha contribution. The two photon events are mostly untagged and so only a small fraction of the collision energy is detected. The discrimination of the tau pair signal against the two photon background is difficult as there are many tau pairs at the lower visible energy but events having $Rshw < 0.2$ and $Rtrk < 0.2$ are removed from the final sample. Additionally $Rshw$ was required to be between 0.02 and 0.7 to reduce dimuon(bhabha) events with small(large) calorimeter deposits. Finally $Rtrk$ was required to be less than 0.8 to suppress further bhabhas and non-radiative muon events.

Expected energy

The expected energy of each cone can be calculated from the measured angles, under the assumption of a single ISR photon along the beam, as following:

$$R_{cone(i)} = \sqrt{s}\ \frac{|\sin\theta_i|}{\sin\theta 1 + \sin\theta 2 + |\sin(\theta 1 + \theta 2)|} \tag{4.4}$$

An additional background reduction can be achieved by comparing the sum in quadrature of the two expected charged cones energies to that measured by the calorimeter or the tracking detectors.

For bhabha background the measured energy from both tracks or calorimeter clusters should be close to that calculated using equation 4.4. For muon pairs the calorimeter energy should be low when compared to the expected one. Thus, the following cuts were applied:

$$\frac{P^2_{cone1} + P^2_{cone2}}{R^2_{cone1} + R^2_{cone2}} < 0.8$$

$$0.02 < \frac{E^2_{cone1} + E^2_{cone2}}{R^2_{cone1} + R^2_{cone2}} < 0.8$$

where $R_{cone(i)}$, $E_{cone(i)}$ and $P_{cone(i)}$, are the expected, calorimeter and track energy for cone(i) respectively.

Missing energy

Background processes such as bhabhas and two photon collisions tend to have the vector of the missing energy parallel to the beam axis due to ISR photons or untagged electrons

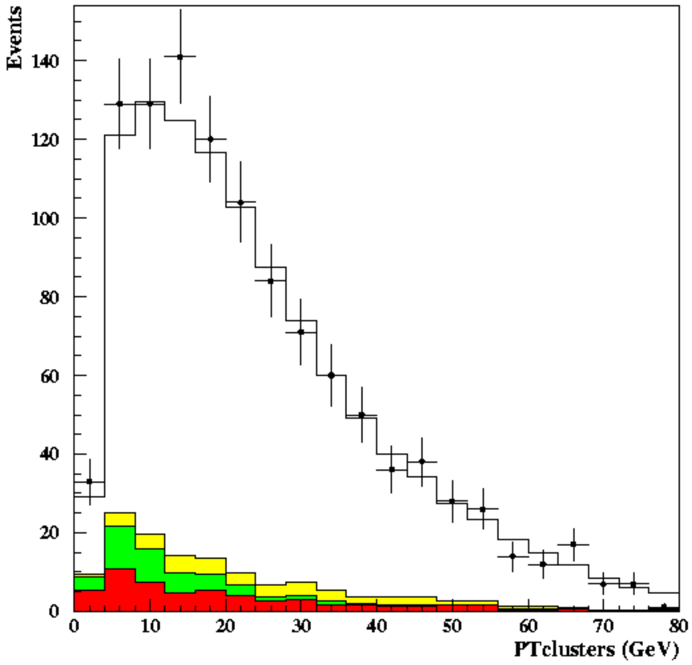

Figure 4.6: The $PT_{clusters}$ distribution for all energies combined. The open histogram is the signal Monte-Carlo prediction, the red(dark), green(medium) and yellow(light) are the predictions for two fermion, two photon and four-fermion background processes respectively. The points with error bars are data.

respectively. In contrast, the missing energy vector in tau pairs due to neutrino emission has an amplitude and polar angle over a wide range of values. Thus, a large observed transverse momentum is a strong characteristic of tau pairs and its value as measured by the calorimeter variable $PT_{clusters}$ (figure 4.6) is required to be greater than 0.015 $\sqrt{s}$. In addition, the $|\cos\theta|$ angle of the missing energy vector as measured from the calorimeter is required to be less than 0.99.

4.2.5 Events with zero calorimeter cone energy

An excess of events where zero calorimeter energy is observed in one cone has led to a further investigation of this region of phase space. As can be seen in figure 4.7, there are 25 data events with zero calorimeter energy in the second most energetic cone and very few in the Monte-Carlo simulation. These data events were scanned visually with the help of the OPAL event display GROPE [58]: the most common characteristic was the missasignment of the cluster to tracks in one of the cones and noise in the track chamber. This is caused by very poor track reconstruction, as can be seen in figure 4.8, leading to tau candidate cones with no calorimeter energy. Due to the fact that the effect is not simulated well in the Monte-Carlo, events with calorimeter energy less than 0.1 GeV were removed from the sample.

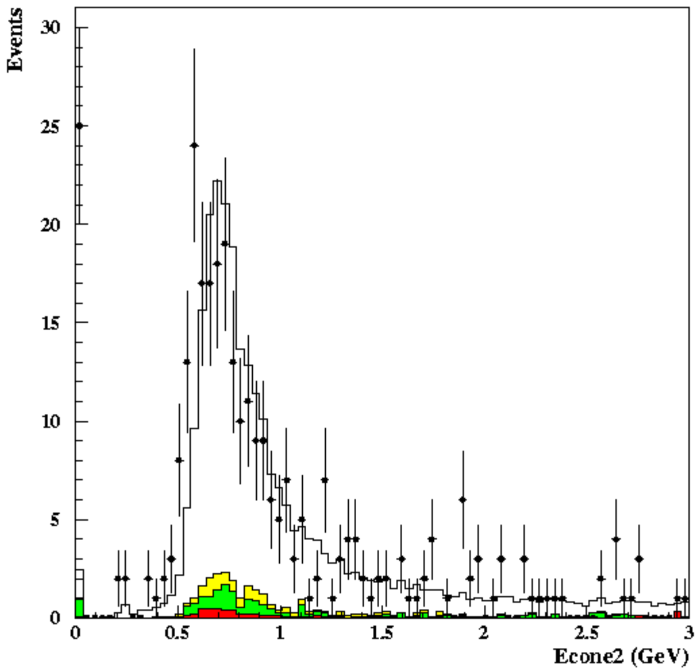

Figure 4.7: Calorimeter energy of the second most energetic cone in the range 0-3 GeV for all high energy data combined. (Most of the data has a larger calorimeter energy than 3 GeV). There is a small shift in the peak of the distribution for data and Monte-Carlo due to the fact that the calorimeter is optimized for electron identification.

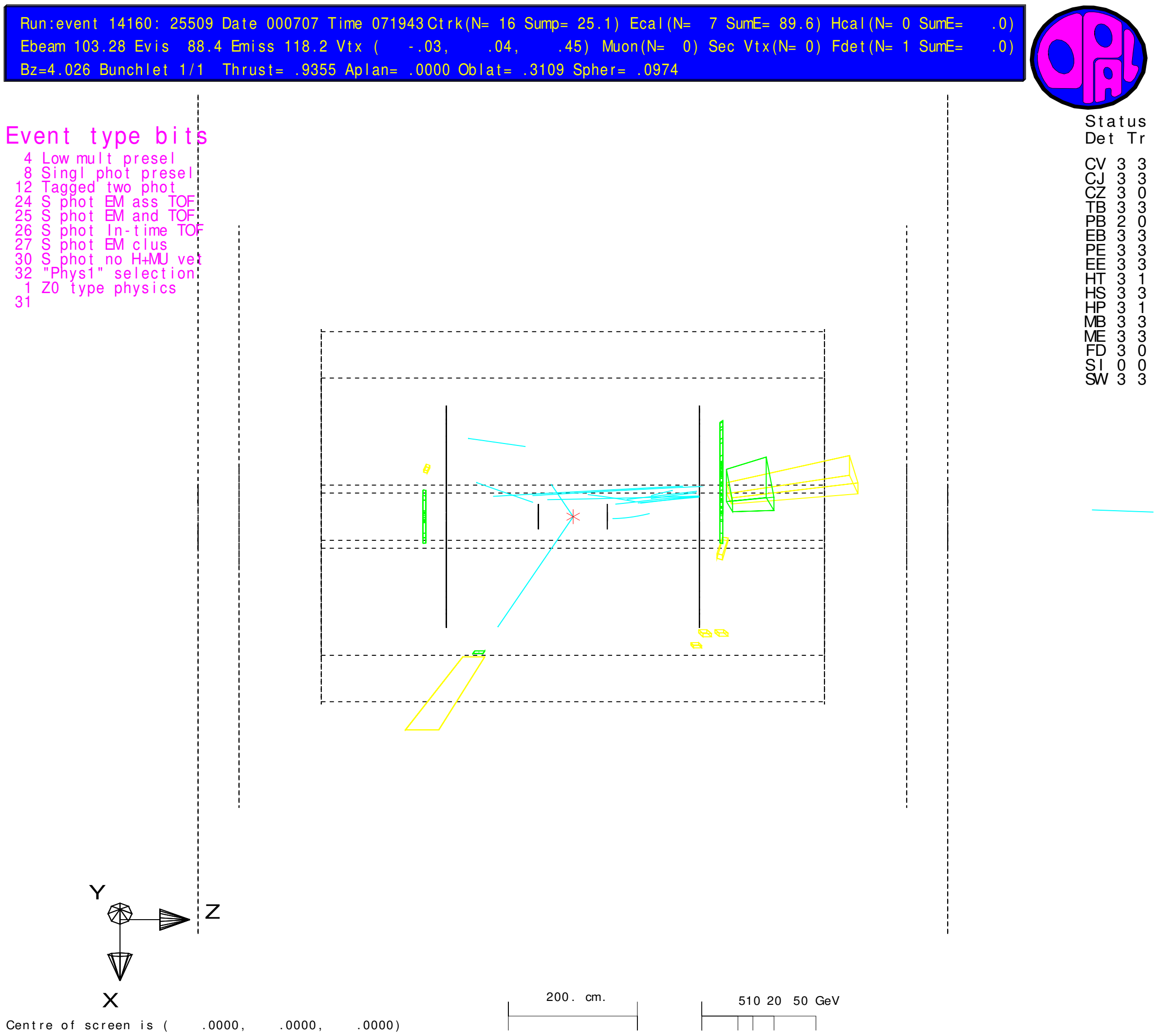

Figure 4.8: Event display of tracks and calorimeter clusters for an event with zero calorimeter energy.

4.2.6 Acoplanarity, Acolinearity

The particles produced in the process $e^+e^- \to \tau^+\tau^-$ are constrained to lie in the same plane. At full energy the initial taus are produced back-to-back. An ISR photon can change that by boosting the centre of mass frame with respect to the lab, but as it is usually emitted along the z-axis, the back-to-backness in the x-y plane is conserved. Tau decays cannot change the initial direction significantly, as the transverse momentum component to the cone direction is limited by the tau mass. Thus, the difference between the tau cone angles when projected on the x-y plane and compared to π is a measure of acoplanarity and is small for the signal. In contrast, four fermion background events are not constrained to be in the same plane if the tau candidates originate from the different decaying bosons. For this analysis the acoplanarity is required to be less than 30 °.

The general measure of back-to-backness is the acolinearity defined as the difference from π of the angle between the tau cones:

$$\theta_{acolinearity} \equiv 180^\circ - \cos^{-1}\left(\frac{\vec{p1} \cdot \vec{p2}}{|\vec{p1}||\vec{p2}|}\right) \tag{4.5}$$

where $\vec{p1}$, $\vec{p2}$ are the vector sum of the cone track momentum and calorimeter energy.

The virtual photons in two photon processes do not have usually equal momentum, resulting in highly acolinear events. In order to suppress this two photon background the acolinearity is required to be:

$$\theta_{acolinearity} \quad < \quad 180^\circ - 2\tan^{-1}\left(\frac{2M_Z\sqrt{s}}{s - M_Z^2}\right) + 10^\circ \tag{4.6}$$

which for a centre of mass energy of 206 GeV is approximately 94 °. The cut is a function of $\sqrt{s}$ and allows most of the acolinear taus to pass the selection (figure 4.9).

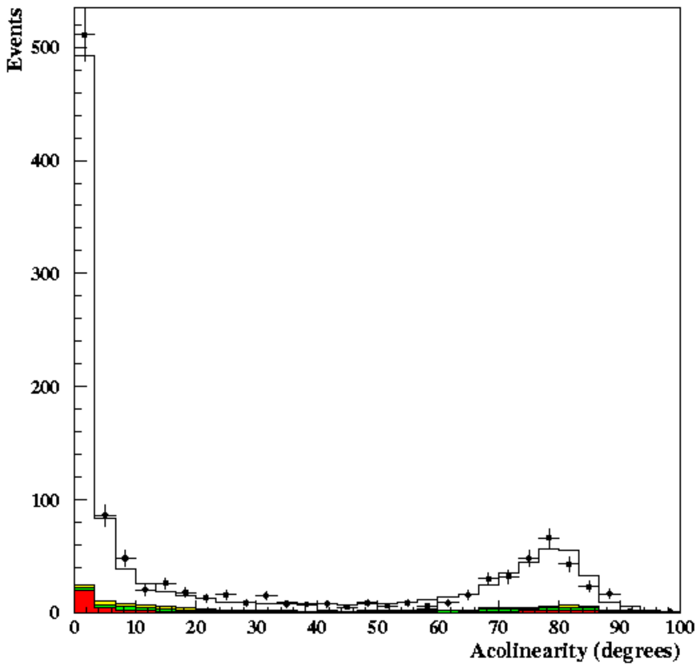

Figure 4.9: The acolinearity distribution for all energies combined.

For planar events with a high energy photon detected as described in the determination of $\sqrt{s}$, both acoplanarity and acolinearity constraints are not applied as they are based on the assumption that there are only two cones [52]. The non-application of acolinearity and acoplanarity for planar events with an energetic photon increases the efficiency with a negligible increase on the background.

4.2.7 Geometrically accepted region

Geometrical acceptance

The momentum resolution of the detector becomes poorer for large polar angles. Only events with both tau candidate cones having a $|\cos\theta|$ less than 0.9 are accepted to avoid poorly modelled detector regions.

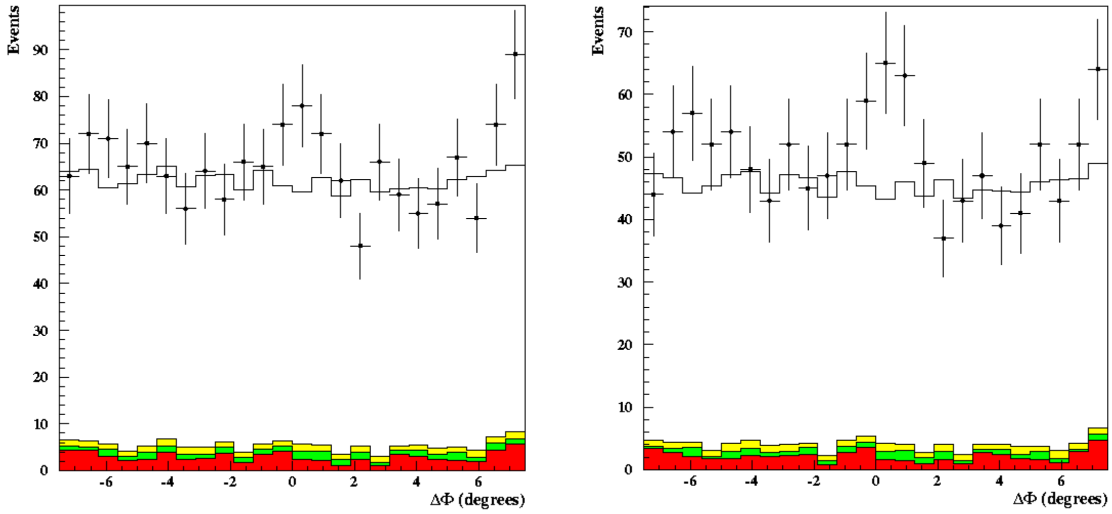

Figure 4.10: The $\Delta\phi$ distribution for all energies (left) and for all data above $\sqrt{s} > 200$ GeV (right). The open histogram is the Monte-Carlo prediction for the signal and the coloured(grey) is the background. The points are data.

Anode Wires

As already mentioned in chapter 2, the CJ detector consists of 24 identical ϕ sectors with radial r-z planes, each consisting of 159 anode wires running parallel to the beam axis. It is known since the LEP1 era that high momentum charged particles passing close to the anode wires of the central jet chamber (CJ), have relatively poor momentum measurement and may suffer track reconstruction problems ([59], [60]). The Monte Carlo modelling of this detector effect is not so precise. The difference in ϕ from the anode planes is defined as:

$$\Delta\phi \equiv \quad mod(\phi, 15^\circ) - 7.5^\circ$$

where the shifting of 7.5 $^\circ$ is necessary to take into account that the wires are located in the middle of each of the 24 sectors.

In figure 4.10 $\Delta\phi$ is plotted for non-radiative tau pair candidates. These are more likely to be affected as they are energetic and by definition back-to-back. Due to the higher momentum they have straight tracks moving parallel to the wire plane for a longer time than radiative events which have more curved tracks. A small excess of events in the region of the anode wires is observed in the non-radiative sample, but due to much lower statistics at LEP2 it was decided to to use the LEP1 fiducial cut to define the acceptance. Events with either track within 0.5 $^\circ$ difference in ϕ from the anode wire plane are removed from the final sample as a geometrical cut to exclude a region of the tracking detector that is not well simulated.

4.2.8 Likelihood Rejection of Two Photon Background

After applying the cuts already discussed the background contamination of the intermediate $\sqrt{s'}$ region was much higher than in the other two $\sqrt{s'}$ regions in the selection used to derive the preliminary results. The most important background contribution arises from two photon processes which were a significant source of the total systematic uncertainty in the cross-section when the OPAL 189 GeV selection was used for a preliminary analysis of the high energy data [55]. Attempts to reduce this background using simple cuts were not efficient and so a more effective observable was constructed using the multivariant discriminant likelihood method.

Multivariable discriminant methods

The extraction of a signal from a data sample is traditionally done with the help of simple conditions ('cuts') on single variables. The advantage in this case is that each cut can be studied separately, for example in the estimation of the systematic uncertainties. The big disadvantage is that not all the available information is used as correlation between different variables are not taken into account. For example an event that fails a few cuts only slightly is more likely to be a signal than an event which passes some of them but fails the rest a large amount. In order to use the information given by the correlations multivariable discriminant methods need to be used, such as:

- **Fisher linear discriminant**

  A linear combination of n variables is constructed and the coefficients are calculated such that the separation of the signal with the background for the new observable is maximum [29].

- **neural networks**

  A single layer (node) is a non-linear function which takes as input a linear combination of n-variables. The coefficients are adjusted so as the output separation for the signal and background is maximized (training). More than one layer is usually used where each layer takes as inputs the outputs of the previous layers. The separation is optimum, but the technique is often criticized for being fragile to uncertainties in the model [61].

- **nearest neighbour**

  The phase space is partitioned to n-cubes for n-variables and the signal to background ratio is used to decide whether the cube will be in the accepted region [61].

- **likelihood discriminant** as described in the next section.

The likelihood discriminant

A new observable is constructed from n-input variables called the likelihood probability $\mathcal{L}$, such as for most of signal events $\mathcal{L}$ is peaking near 1 whereas for most of background it is concentrated at lower values ([62], [63]).

A probability distribution function (PDF) is constructed for each of the input variables for both signal and background events by normalizing to unity the distributions (histograms) generated using Monte-Carlo. As the kinematics of the three $\sqrt{s'}$ regions are different, the study was performed using the distributions of tau pairs and two photon simulated events in the intermediate $\sqrt{s'}$ region where the background problem was most severe.

For a given histogram generated for a variable j the probability for an event generated at bin i to be signal is:

$$p_i^j(signal) = \frac{h_i^j(signal)}{h_i^j(signal) + h_i^j(background)} \tag{4.7}$$

where $h_i^j(signal), h_i^j(backgr.)$ are the PDFs for variable j, for signal and background Monte-Carlo events. The probability for an event in bin i to be background is similarly:

$$p_i^j(background) = \frac{h_i^j(background)}{h_i^j(signal) + h_i^j(background)} \tag{4.8}$$

In order to overcome fluctuations due to limited statistics in the intermediate $\sqrt{s'}$ energy region, simple polynomial functions were fitted and used to model the distributions p_i^j. The combination of information from n variables is achieved by multiplying all p_i^j:

$$P_i(signal) = \prod_{j=1}^{n} p_i^j(signal). \tag{4.9}$$

$$P_i(background) = \prod_{j=1}^{n} p_i^j(background). \tag{4.10}$$

The construction of the likelihood $\mathcal{L}$ is then achieved by taking:

$$\mathcal{L} = \frac{P_i(signal)}{P_i(signal) + P_i(background)}, \tag{4.11}$$

The selection of input variables for the likelihood is not an easy problem. In practice a manageably small subset of the possible variables is preferred, with an emphasis on those which have significant discriminating power on their own. Different combinations of variables that were considered able to discriminate tau pairs from two photon events have been tested.

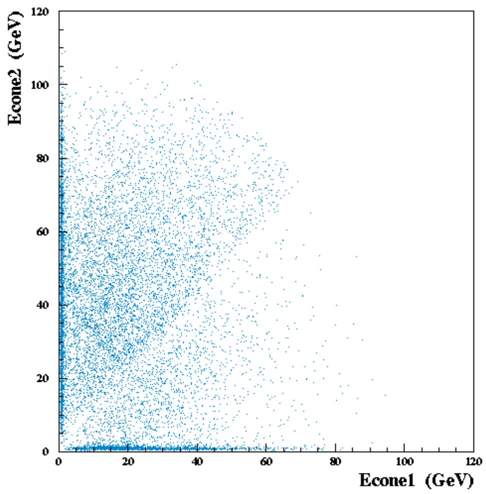

Figure 4.11: Correlation between the cluster cone energy of the two tau candidates for tau pairs Monte-Carlo at 206 GeV. The region close to the line $E_{cone1} = E_{cone2}$ is less populated than the rest of the plane.

Finally the following four variables were used:

- $|E_{cone1} - E_{cone2}|$

  where $E_{cone1,2}$ are the calorimeter energies associated with the two tau cones. The detected energy for each tau cone coves a wide range of values due to neutrino emission. Thus, it is unlikely for the two uncorrelated tau cones to have the same detected calorimeter energy as can be seen in figure 4.11.

- $PT_{clusters}$

  The vector sum of calorimeter cluster momentum transverse to the beam is as already mentioned an important variable for selecting tau pairs.

- R_{trk}

  The visible energy as measured from the tracks for the two photon events is usually small as the initial electrons(positrons) are lost in in the beam pipe.

- The invariant mass of the two cones,

  as calculated from the combined cluster energy and track momentum of the two cones.

The likelihood constructed in the intermediate region using the above 4 observables can be seen in figure 4.12. The taus have indeed populated the region close to $\mathcal{L}$=1, whereas most of the two photon background is concentrated at lower values. This separation between the two distributions allows the efficient rejection of a large fraction of the two photon background by rejecting all events in the intermediate $\sqrt{s'}$ region that have a likelihood $\mathcal{L}$ of less than 0.5.

4.3 Efficiency Determination

The efficiency ϵ_{2f} of the two fermion process $e^+e^- \rightarrow \tau^+\tau^-$ is defined as the number of events selected divided by the total number of generated signal events. In addition for the non-radiative selection the events selected must have generated $s'/s > 0.7225$. The determination of the efficiency is complicated by the radiation of photons as some four fermion events can be considered as signal events. However, this produces a very small change in the overall selection efficiency.

4.3.1 Four Fermion efficiency correction

The definition of the effective centre of the mass energy as the mass of s-channel propagator introduces a further complication: The events arising from the emission of additional low mass fermion pairs must be included in the signal definition like the

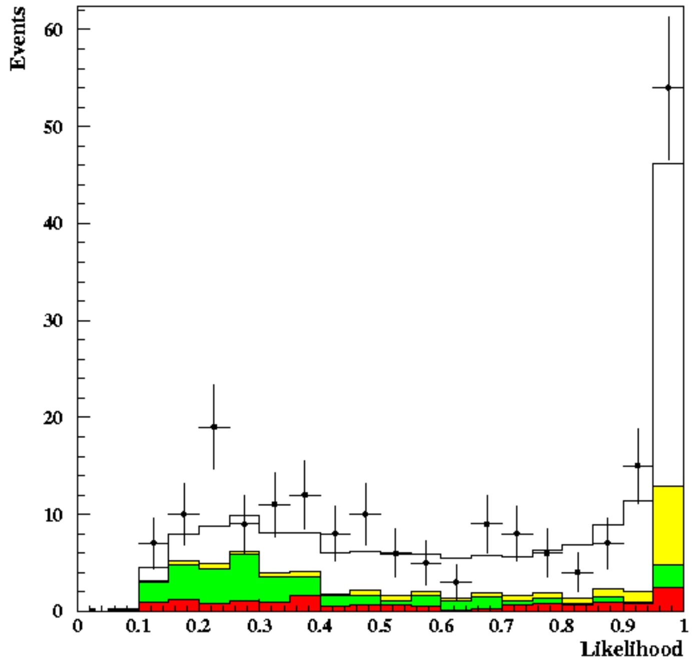

Figure 4.12: The likelihood distribution in the intermediate $\sqrt{s'}$ region for all energies combined. The open histogram is the signal Monte-Carlo prediction, the red(dark), green(medium) and yellow(light) are the predictions for two fermion, two photon and four-fermion background processes. The points with error bars are data.

photons. On the contrary, four fermion events originating from virtual Z boson in either initial or final states must be regarded as background [54]. At lower collision energies, kinematic cuts were used to classify these events to signal if the pair was produced via a photon, or to background if it was produced via a Z boson.

For higher energies a different method was introduced by the LEP2 collaborations [64]: each four fermion Monte Carlo event is given a weight of being a signal or a background based on the ratio:

$$\omega_i = \frac{\sum |\mathcal{M}^{signal}|^2}{\sum |\mathcal{M}^{signal} + \mathcal{M}^{background}|^2}$$

where $\sum |\mathcal{M}^{signal}|^2$ is the sum of all amplitudes for a given final state originating from Feynman diagrams compatible with being a signal and $\sum |\mathcal{M}^{signal} + \mathcal{M}^{background}|^2$ is the sum over all such four fermion final states. The four fermion events passing the selection are multiplied by ω_i and added to the selected two fermion events under study. The same procedure is repeated at the generator level. The four fermion efficiency ϵ_{4f} is then the ratio of weighted total of selected events to the weighted total of generated four fermion events.

4.3.2 Efficiency estimation

The overall selection efficiency ϵ is calculated by weighting the contribution of two fermion and four fermion events in the measured cross-section as follows:

$$\epsilon = \left(1 - \frac{\sigma_{4f}}{\sigma_{tot}}\right) \epsilon_{2f} + \frac{\sigma_{4f}}{\sigma_{tot}} \epsilon_{4f}$$

where ϵ_{2f}, ϵ_{4f} are the two fermion and four fermion efficiencies respectively, σ_{4f} is the generated signal four fermion cross-section and σ_{tot} is the total cross-section from ZFITTER [53] including pair emission. A more detailed discussion about the selection efficiency used by the OPAL two-fermion group can be found at [54].

The efficiency estimation for all energies can be seen in table 4.2. For the inclusive selection the efficiency ranges from 31.9% up to 33.1%, whereas for the non-radiative selection it varies between 47% - 48%.

4.4 Background Processes

4.4.1 Two photon background

Two photon physics refers to processes where the beam electron and positron each emit a virtual photon which interact to give a lepton-antilepton pair as shown in figure 4.13 or a hadronic system. This reaction offers the opportunity to study interesting physics

Efficiencies and backgrounds 192 - 206 GeV				
Energy		Efficiency (%)	Background (pb)	Feedthrough (pb)
192 GeV	$s'/s > 0.01$	33.10±0.64±0.81	0.272±0.023±0.045	–
	$s'/s > 0.7225$	48.08±0.73±1.18	0.120±0.019±0.017	0.057±0.003±0.003
196 GeV	$s'/s > 0.01$	32.85±0.65±0.81	0.273±0.016±0.045	–
	$s'/s > 0.7225$	47.80±0.73±1.18	0.119±0.012±0.017	0.051±0.003±0.000
200 GeV	$s'/s > 0.01$	32.66±0.65±0.80	0.292±0.017±0.045	–
	$s'/s > 0.7225$	47.70±0.73±1.17	0.125±0.014±0.018	0.050±0.003±0.001
202 GeV	$s'/s > 0.01$	32.06±0.66±0.79	0.277±0.016±0.045	–
	$s'/s > 0.7225$	47.43±0.74±1.17	0.110±0.012±0.017	0.043±0.002±0.001
205 GeV	$s'/s > 0.01$	32.22±0.66±0.79	0.263±0.014±0.041	–
	$s'/s > 0.7225$	47.78±0.73±1.18	0.100±0.009±0.017	0.044±0.002±0.001
206 GeV	$s'/s > 0.01$	31.89±0.66±0.78	0.271±0.017±0.041	–
	$s'/s > 0.7225$	47.07±0.74±1.16	0.109±0.012±0.018	0.040±0.002±0.001

Table 4.2: Efficiencies, backgrounds and feedthrough for tau pair analysus for each energy from 192 up to 206 GeV. The first error is statistical and the second systematic.

	Physics process	Generator	$s'/s > 0.01$ σ (pb)	$s'/s > 0.7225$ σ (pb)
2-fermion	$\tau^+\tau^-$	KORALZ		
	$\mu^+\mu^-$	KORALZ	0.0328±0.0020	0.0071±0.0010
	$\mathrm{e}^+\mathrm{e}^-$	BHWIDE	0.0699±0.0132	0.0499±0.0112
	$\mathrm{q\overline{q}}$	PYTHIA	0.0079±0.0020	0.0005±0.0005
2-photon	$\mathrm{e}^+\mathrm{e}^-\mathrm{q\overline{q}}$ tagged	HERWIG	0.0010±0.0010	0.0000±0.0000
	$\mathrm{e}^+\mathrm{e}^-\mathrm{q\overline{q}}$ untagged	PHOJET	0.0000±0.0000	0.0000±0.0000
	$\mathrm{e}^+\mathrm{e}^-\mathrm{c\bar{c}}$	PYTHIA	0.0000±0.0000	0.0000±0.0000
	$\mathrm{e}^+\mathrm{e}^-\mathrm{e}^+\mathrm{e}^-$	VERMASEREN	0.0279±0.0054	0.0114±0.0034
	$\mathrm{e}^+\mathrm{e}^-\mu^+\mu^-$	VERMASEREN	0.0116±0.0034	0.0010±0.0010
	$\mathrm{e}^+\mathrm{e}^-\tau^+\tau^-$	VERMASEREN	0.0443±0.0066	0.0098±0.0031
4-fermion	$\mathrm{e}^+\mathrm{e}^-\mathrm{e}^+\mathrm{e}^-$	GRC4F	0.0016±0.0006	0.0002±0.0002
	$\mathrm{e}^+\mathrm{e}^-\mu^+\mu^-$	GRC4F	0.0072±0.0012	0.0012±0.0005
	$\mathrm{e}^+\mathrm{e}^-\tau^+\tau^-$	GRC4F	0.0114±0.0015	0.0010±0.0005
	$\mathrm{e}^+\mathrm{e}^-\mathrm{q\overline{q}}$	GRC4F	0.0052±0.0010	0.0010±0.0004
	$\mathrm{q\overline{q}q\overline{q}}$	GRC4F	0.0002±0.0002	0.0000±0.0000
	$l^+l^-\mathrm{q\overline{q}}$	GRC4F	0.0018±0.0006	0.0010±0.0005
	$l^+l^-l^+l^-$	GRC4F	0.0481±0.0031	0.0247±0.0022

Table 4.3: Monte Carlo sample used in efficiency and background estimates at 206 GeV and the background estimates as cross-sections for both inclusive and non-radiative samples.

processes as LEP can be considered a high luminosity as well as high energy gamma gamma collider [65], [66]. The cross-section of these processes increase logarithmically with the collision energy and become important backgrounds to many analyses such as fermion pair production where the annihilation cross-section decreases like s^{-1}.

If the virtualites of the two photons are small, the electron and positron are scattered at small angles escaping undetected in the beam pipe (untagged 2 photon events). In the case where only one of the photons has large virtuality while the other is quasi-real, only one electron is detected (tagged event). Detection of both electron and positron is very rare .

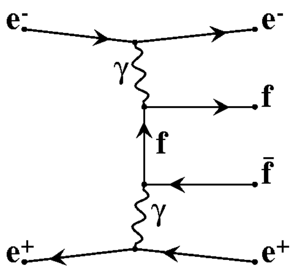

Figure 4.13: Feynman diagram of a two photon process

4.4.2 Four Fermion Background

Four fermion processes refer to essentially all S.M final states at LEP which are not two fermions ($e^+e^-\to f\bar{f}(\gamma)$) or multi-photons ($e^+e^-\to\gamma\gamma(\gamma)$). They are classified according to the intermediate states produced before decaying to four fermions.

$$\sigma(e^+e^-\to 4f) = \sigma(e^+e^- \to \chi) \times BR(\chi\to 4f)$$

The processes are classified as:

- **WW production** which has been discussed in section 3.1.
- $e^+e^-\to f\bar{f}e^+e^-$ production via multiperipheral graphs. These are the two photon events discussed in section 4.4.1.

- **ZZ production** The Feynman diagram for this process can be seen in figure 4.14 (c) The experimental signature depends on wether the Z bosons decay to charged leptons, neutrinos, or quark pairs.

- **Single W, Z production** as seen in figures 4.14 (a), (b) and 4.14 (d) respectively.

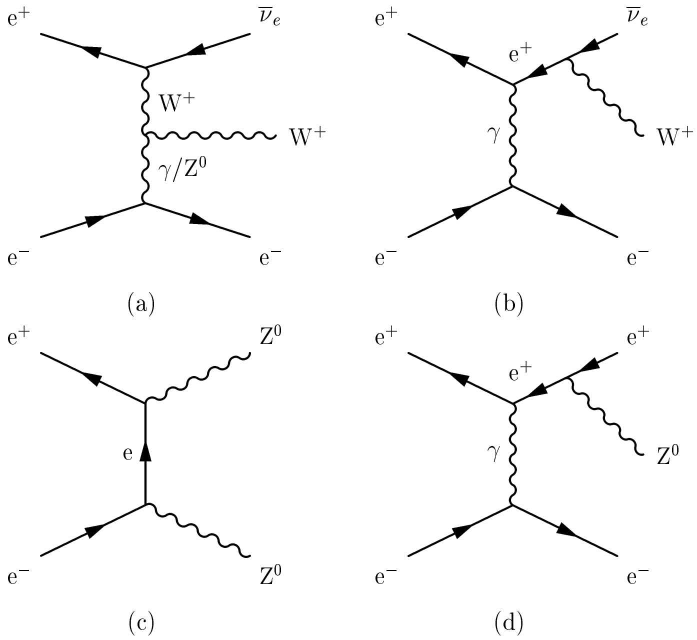

Figure 4.14: Feynman diagrams for four fermion processes (a-b) single W production, (c) Z-pair production, (d) single Z production.

4.5 Background estimation from Monte-Carlo

The estimation of the background for the tau pair selection is performed with the help of a sample of Monte Carlo events created using the generators listed in table 4.3. The feedthrough events are defined to have generated $s^{'}/s$ less than 0.7225 but a reconstructed value above this cut. The contribution of the background and feedthrough to the measured cross-section is estimated by $\sigma_{visible}$:

$$\sigma_{visible} \equiv \frac{N_{selected}}{N_{generated}} \quad \sigma_{generated} \tag{4.12}$$

The calculated cross-sections are scaled by E_{MC}^2/E_{CM}^2 to take into account the very small difference between the generated Monte-Carlo collision energy E_{MC} and the luminosity weighted centre of mass energy of the data E_{CM}. This scaling is not applied to two photon processes, as these remain almost constant within small energy variations. The total background for both the inclusive and non-radiative selections has no significant variation between different collision energies.

Table 4.3 gives the visible cross-section for all background processes as predicted by Monte-Carlo simulation at energy 206 GeV. For the inclusive selection the total background level is estimated to be $\sim 11.8\%$ of the observed cross-section. The biggest contribution to the background comes from the two-fermion diagrams ($\sim 40.8\%$), in which a large fraction originates from bhabhas ($\sim 25.8\%$). The two photon processes contribute about 31.3%, mainly from $e^+e^-\tau^+\tau^-$ ($\sim 16.3\%$) and $e^+e^-e^+e^-$ ($\sim 10.3\%$). The four fermion contribution is 27.9%.

For the non-radiative selection the background level is around 8% , with an additional feedthrough contribution of 3.1% . The bhabhas make the most significant individual contribution to the background ($\sim 45.9\%$), followed by the four fermion ($\sim 26.7\%$) and two photon ($\sim 20.4\%$) processes.

4.6 I/FSR interference

As already mentioned the effective collision energy after ISR, is defined as the mass of the s-channel propagator. This definition is ambiguous due to the interference between the initial and final state radiation. This problem is dealt with by calculating the contribution of the interference terms and subtracting it from the data. This correction removes the ambiguity in $\sqrt{s'}$ definition and allows direct comparison with the KORALZ [68] Monte Carlo samples generated with I/FSR interference switched off [54].

This correction is calculated by the ZFITTER program [53], which allows the calculation of the differential cross-section including ($\mathrm{d}^2\sigma_{int}/\mathrm{d}m_{\mathrm{f\bar{f}}}\mathrm{d}\cos\theta$) or excluding ($\mathrm{d}^2\sigma_{noint}/\mathrm{d}m_{\mathrm{f\bar{f}}}\mathrm{d}\cos\theta$) interference. The difference between these defines the differential 'interference cross-section' $\mathrm{d}^2\sigma_{IFSR}/\mathrm{d}m_{\mathrm{f\bar{f}}}\mathrm{d}\cos\theta$, $m_{\mathrm{f\bar{f}}}$ being the invariant mass of the fermion pair. The efficiency assumed for this cross-section E_{IFSR}, is the same as the one calculated from MC events which do not include interference:

$$E_{IFSR}(\cos\theta, m_{\mathrm{f\bar{f}}}) = \epsilon_{noint}(\cos\theta, m_{\mathrm{f\bar{f}}}),$$

where $\epsilon_{noint}(\cos\theta, m_{\mathrm{f\bar{f}}})$ is the efficiency without interference as a function of $m_{\mathrm{f\bar{f}}}$ and $\cos\theta$. In practice the calculation is performed in twenty $m_{\mathrm{f\bar{f}}}$ and twelve $\cos\theta$ bins.

4.7 Measurement of Cross-sections & Asymmetries

4.7.1 Data quality and Luminosity

Recorded data are used in the tau pair analysis if they satisfy specific quality requirements. Each subdetector/subtrigger is given a status which has a range from 0-3, 0/1 being when the status of the detector is unknown/unfunctional and 2/3 if there are minor/no problems respectively. Table 4.4 describes the status required for each subdetector/trigger in this analysis.

Status	CV	CJ	TB	EB	EE
Detector	2	2	3	3	3
Trigger	0	2	3	2	3

Table 4.4: The detector and trigger status requirements for the tau pair analysis.

The luminosity is measured using small angle bhabha scattering as detected by the silicon tungsten monitor (SW), or the forward detector (FW) when SW is not at status

3. Data where neither of these two subdetectors is at status 3 are rejected. The data sample is divided into 6 energy bins, each having a range and measured integrated luminosity as described in table 4.5.

Energy	Range	$\sqrt{s}$	$\int \mathcal{L}dt$ (pb^{-1})
192	191.0-194.0	191.59	29.14±0.09
196	194.0-198.0	195.53	75.92±0.19
200	198.0-201.0	199.52	78.04±0.21
202	201.0-202.5	201.64	36.85±0.11
205	202.5-205.5	204.88	78.57±0.21
206	205.5-209.0	206.56	134.68±0.33

Table 4.5: The energy bins, their range, the luminosity weighted E_{CM} and the integrated luminosity per energy as used in the tau pair analysis.

4.7.2 Cross-sections

The observed cross-section is derived by dividing the number of selected data events by the integrated luminosity. The measured tau cross-section is calculated by subtracting the visible background and feedthrough cross-section, as well as the I/FSR interference and correcting for the selection efficiency:

$$\sigma = \frac{1}{\epsilon} \left(\frac{N_{sel}}{\int \mathcal{L}\mathrm{d}t} - \sigma_{bkg} - \sigma_{feed} - \sigma_{int} \right) \tag{4.13}$$

The measured cross-sections for all energy bins are included in table 4.6 and presented in figure 4.15. The latter figure shows that there is no deviation from the theoretical Stanadard Model predictions as calculated by ZFITTER. The insets show the ratio of the measurements and predicted cross-sections for both inclusive and non-radiative samples.

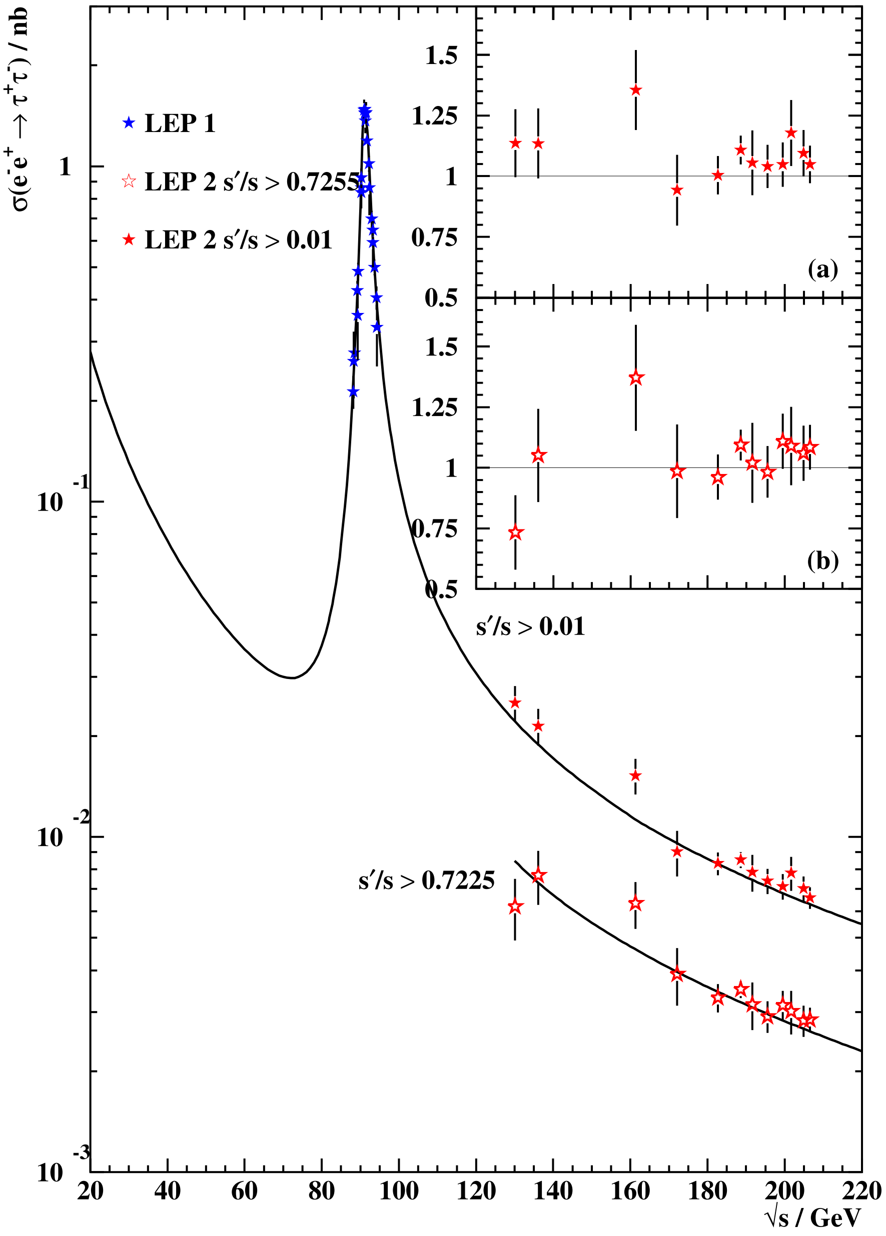

Figure 4.15: The cross-section measurements for the tau pair analysis as a function of $\sqrt{s}$ for both non-radiative and inclusive samples. The solid line is the Standard Model prediction as calculated by ZFITTER. The insets show the ratio of the measurements and predicted cross-sections for (a) $s^{'}/s > 0.7225$ and (b) $s^{'}/s > 0.01$.

Cross-sections					
Energy		$\int \mathcal{L}\mathrm{d}t$ (pb^{-1})	Events	σ (pb)	σ^{SM} (pb)
192	$s'/s > 0.01$	29.14	84	7.85±0.95±0.29	7.44
	$s'/s > 0.7225$		50	3.16±0.50±0.11	3.10
196	$s'/s > 0.01$	75.92	206	7.39±0.57±0.27	7.11
	$s'/s > 0.7225$		120	2.91±0.30±0.10	2.97
200	$s'/s > 0.01$	78.04	205	7.12±0.56±0.27	6.79
	$s'/s > 0.7225$		132	3.15±0.31±0.10	2.84
202	$s'/s > 0.01$	36.85	103	7.82±0.86±0.29	6.63
	$s'/s > 0.7225$		59	3.02±0.44±0.10	2.77
205	$s'/s > 0.01$	78.57	199	7.01±0.56±0.26	6.40
	$s'/s > 0.7225$		119	2.84±0.29±0.09	2.68
206	$s'/s > 0.01$	134.68	321	6.59±0.42±0.25	6.29
	$s'/s > 0.7225$		203	2.85±0.22±0.10	2.63

Table 4.6: Tau pair cross-sections for energies 192-206 GeV. The integrated luninosity, the number of selected events and the Standard Model value as calculated by ZFITTER are also shown. The first error on the cross-section is statistical and the second systematic.

4.7.3 Angular distributions and Asymmetries

The forward-backward asymmetry A_{FB} is measured by counting the number of events in the forward N_F ($\cos\theta > 0$) and in the backward region N_B ($\cos\theta < 0$) according to:

$$A_{FB} = \frac{N_F - N_B}{N_F + N_B} \tag{4.14}$$

As already mentioned, the radiation of an initial state photon boosts the centre of mass frame, resulting in events which are not back-to-back in the laboratory frame. For these events, the two tau cones fall into different $cos\theta$ bins, leading to different corrections for efficiencies, backgrounds and other effects. In order to reduce the systematic effects, the distributions for both positive and negative particles are combined in the charged-signed -Q $cos\theta$ plot (figures 4.16 , 4.17). Only events where the charge can be reliably determined are used, to avoid migration of events to the wrong side of the distribution with respect to zero.

The measured angular distribution is divided into 40 $\cos\theta$ bins. The correction of the -Q $cos\theta$ distribution is done bin-by-bin in the following steps:

- The background per bin is estimated from Monte Carlo and subtracted. For the non-radiative selection the same procedure is also followed for the feedthrough events.
- The I/FSR interference cross-section per bin is estimated with ZFITTER and subtracted.
- The efficiency per bin is calculated by dividing the distribution of selected by the generated events. The number of events per bin after background and feedthrough subtraction is divided by the estimated efficiency to derive the corrected number of events.
- As there is an acceptance cut on the cones of $|\cos\theta| < 0.9$, a correction is applied to correct to the full-angular range, using ZFITTER.

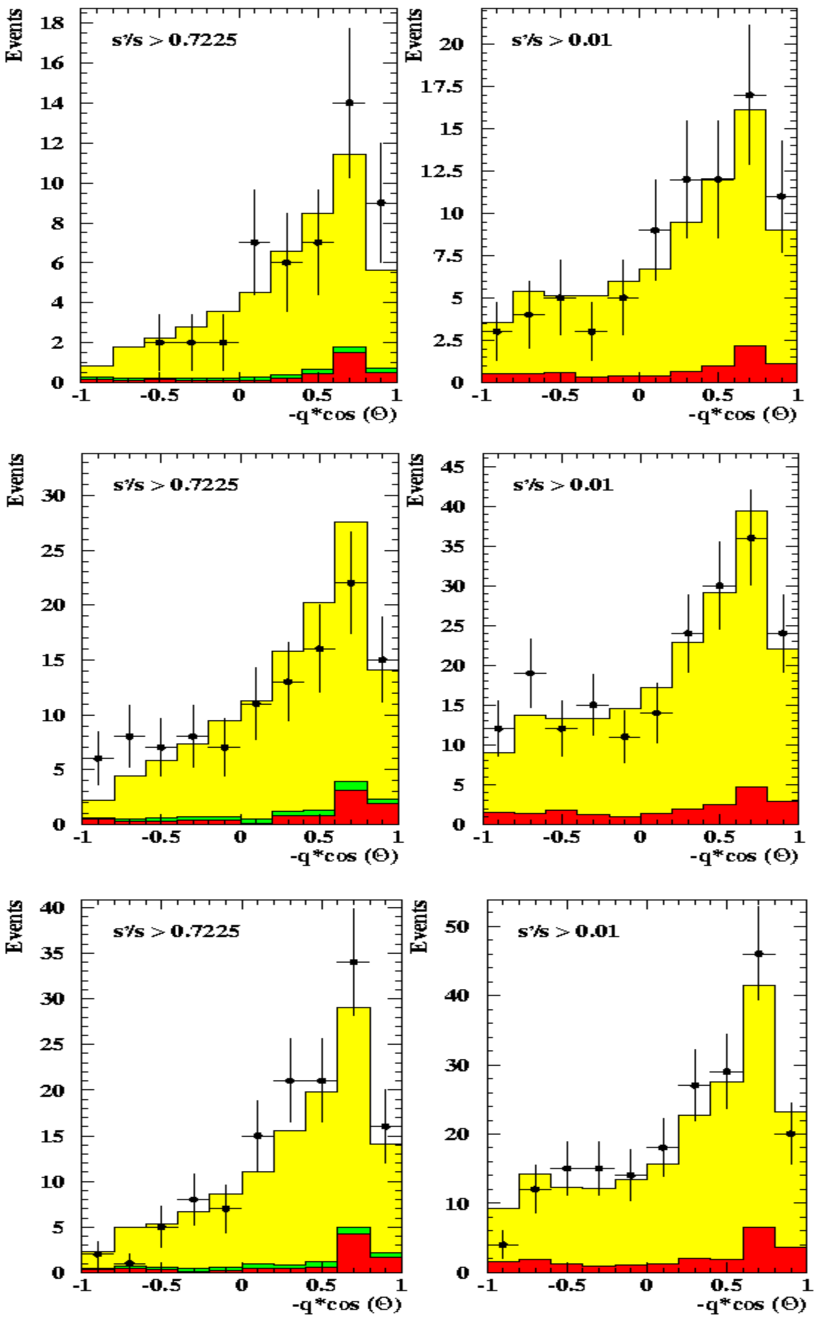

Figure 4.16: The $-Q\ cos\theta$ distributions at $\sqrt{s'}$=192 GeV (upper), 196 GeV (middle), 200 GeV (lower). The plots on the left are for the non-radiative samples and on the right are for the inclusive samples. The yellow (light grey) histogram is the prediction for the tau pairs from Monte-Carlo. The green (medium grey) and red (dark grey) histograms are the predictions for feedthrough and background contributions respectively and the points represent data.

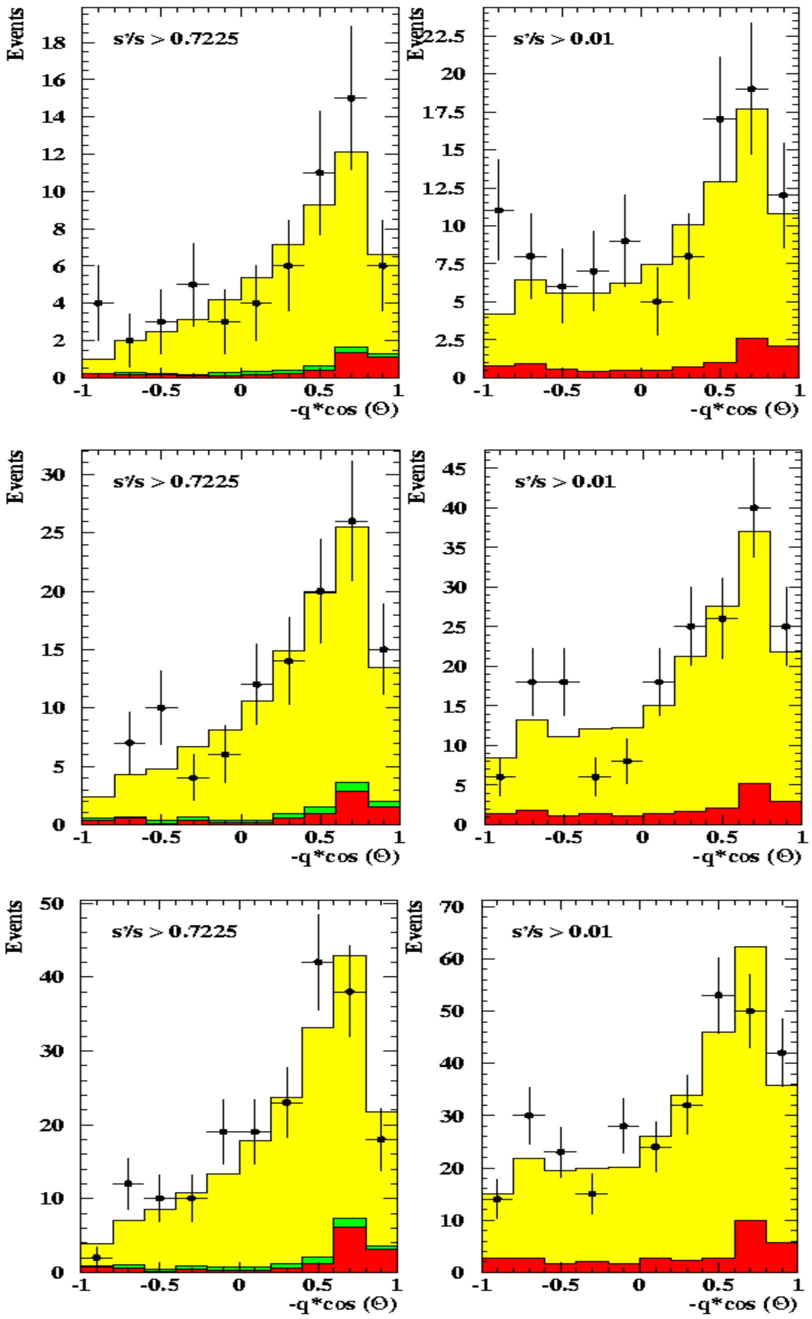

Figure 4.17: The $-Q\ cos\theta$ distributions at $\sqrt{s'}$=202 GeV (upper), 205 GeV (middle), 206 GeV (lower). The plots on the left are for the non-radiative samples and on the right are for the inclusive samples. The colour scheme is the same as in figure 4.16.

The measured asymmetries are presented in table 4.7 and plotted in figure 4.18. The agreement with Standard Model predictions is good for both inclusive and non-radiative samples.

4.8 Systematic Errors

Background

The systematic error for the background was estimated by finding an observable where the background under study can be isolated in a specific region. The cuts suppressing the background are relaxed and the number of data and Monte-Carlo events for all energies combined are compared. The percentage difference is the estimated uncertainty for the background under study. For the process $e^+e^- \rightarrow \mu^+\mu^-$ the comparison of data and Monte-Carlo took place in the visible energy plot between 0.88 and 1.12 giving a percentage difference of $\sim$ 4.8%, whereas for the bhabhas the region was 1.2 to 1.6 where the difference was $\sim$ 19.1%.

For the estimation of two-photon background error the likelihood observable was employed: cuts that suppress this background like the $PT_{clusters}$ and visible energy cuts were relaxed. The likelihood was not applied and the comparison took place in the background-like region ($\mathcal{L} < 0.5$) resulting in an observed difference of $\sim$ 9.6%. The estimated value for this error is very similar to that observed when the visible energy variable is used. For less significant backgrounds the uncertainty was taken conservatively to be 50% of their visible cross-section. The error in the cross-section is then given by:

$$\Delta\sigma(Background) = \frac{\Delta\sigma(bkg_{selected}(pb))}{\epsilon} \tag{4.15}$$

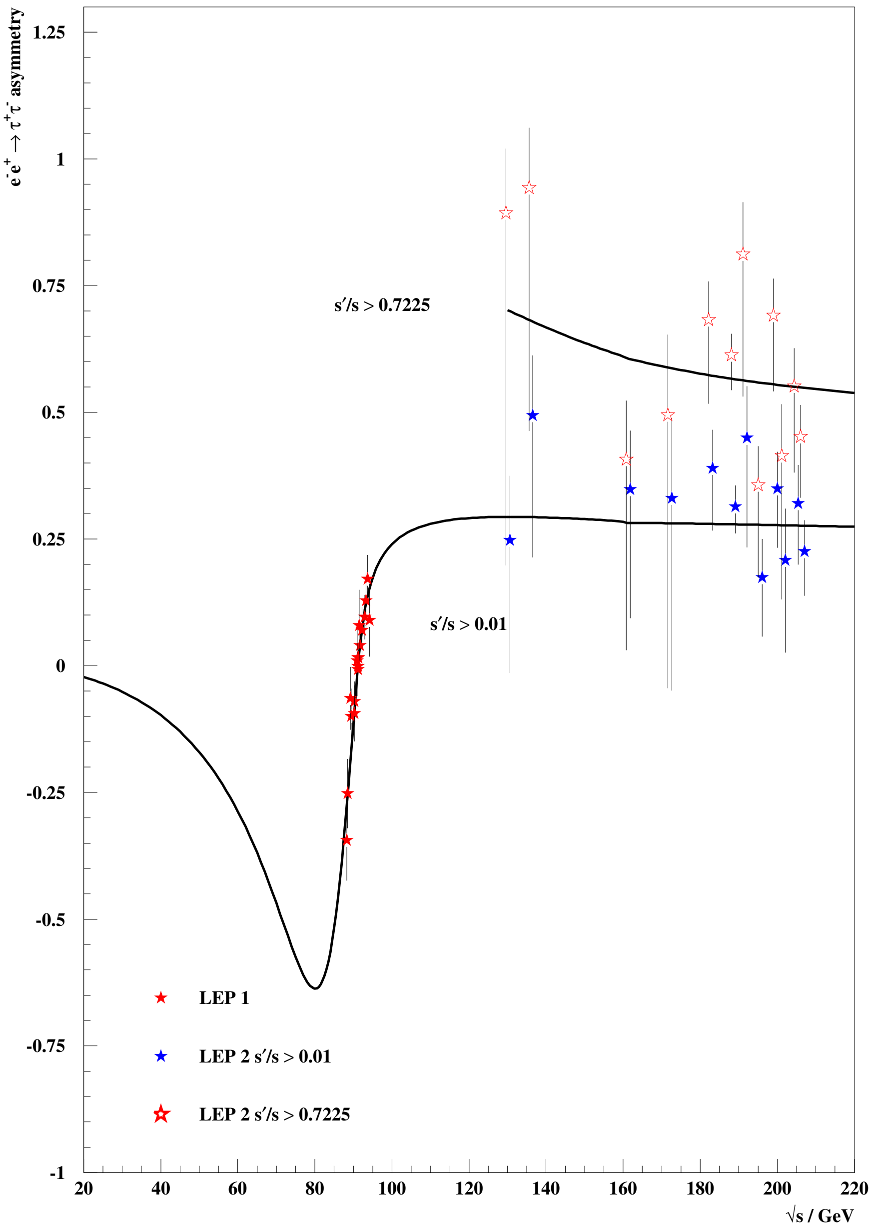

Figure 4.18: The measured asymmetries for tau pairs as function of $\sqrt{s}$ for both inclusive and radiative samples. The solid lines are the Standard Model predictions as calculated by ZFITTER.

Asymmetries					
	Energy	N_{F}	N_{B}	A_{FB}	A_{FB}^{SM}
192 GeV	$s'/s > 0.01$	259.28	95.32	$0.45^{+0.10}_{-0.22} \pm 0.01$	0.28
	$s'/s > 0.7225$	142.84	18.75	$0.81^{+0.10}_{-0.28} \pm 0.04$	0.56
196 GeV	$s'/s > 0.01$	513.44	356.98	$0.17^{+0.08}_{-0.12} \pm 0.01$	0.28
	$s'/s > 0.7225$	246.63	122.20	$0.36^{+0.10}_{-0.18} \pm 0.04$	0.56
200 GeV	$s'/s > 0.01$	587.85	276.45	$0.35^{+0.07}_{-0.12} \pm 0.01$	0.28
	$s'/s > 0.7225$	352.29	73.81	$0.69^{+0.07}_{-0.15} \pm 0.04$	0.55
202 GeV	$s'/s > 0.01$	280.49	181.30	$0.21^{+0.10}_{-0.18} \pm 0.01$	0.28
	$s'/s > 0.7225$	138.18	60.38	$0.41^{+0.13}_{-0.28} \pm 0.04$	0.55
205 GeV	$s'/s > 0.01$	558.79	280.90	$0.32^{+0.07}_{-0.12} \pm 0.01$	0.28
	$s'/s > 0.7225$	284.65	89.58	$0.55^{+0.09}_{-0.17} \pm 0.04$	0.55
206 GeV	$s'/s > 0.01$	846.72	526.58	$0.23^{+0.06}_{-0.09} \pm 0.01$	0.28
	$s'/s > 0.7225$	450.10	180.37	$0.45^{+0.07}_{-0.12} \pm 0.04$	0.55

Table 4.7: The corected numbers of forward (N_{F}) and backward (N_{B}) events and the measured asymmetry values at each energy are shown. The measured asymmetry values include corrections for background and efficiency, and are corrected to the full solid angle. The first error is statistical and the second is systematic. The final column shows the Standard Model predictions as calculated by ZFITTER.

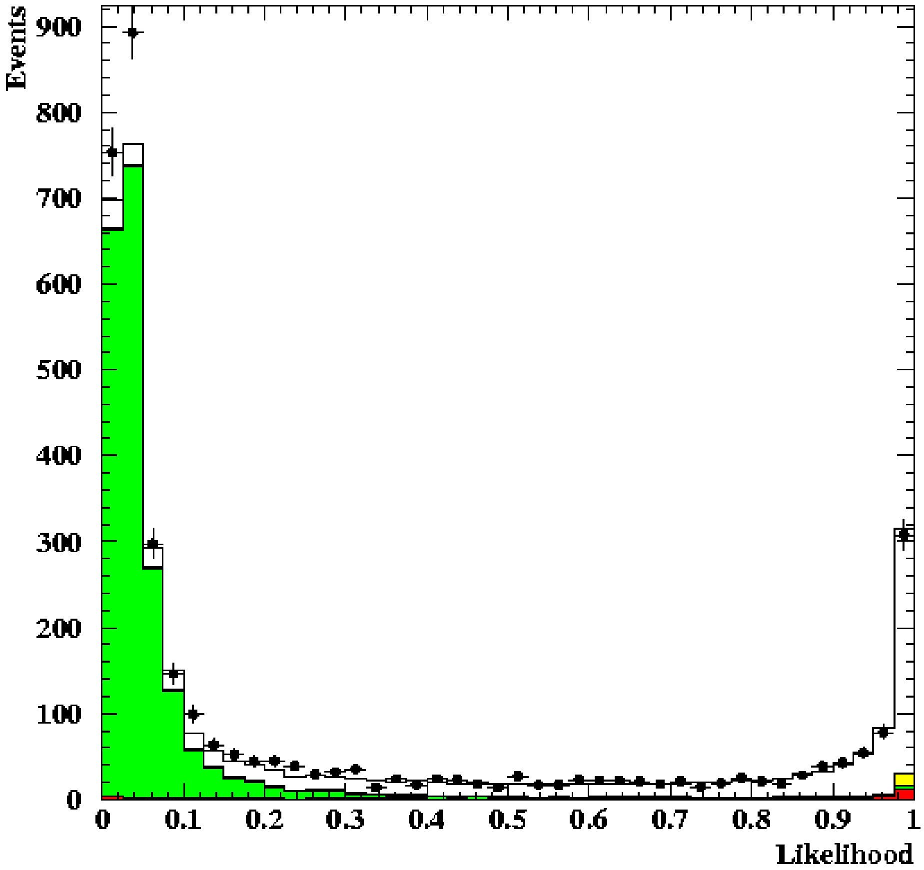

Figure 4.19: The likelihood observable with relaxed cuts for all collision energies combined.

Efficiency

The calculation of the efficiency systematic error was performed using LEP1 data to overcome the limitation of low statistics at LEP2. The value of the acolinearity cut as derived from equation 4.5 rejects events in the Z peak and so it was modified to be 15° for this study. The selection was then applied to the data collected during 1994 and Monte Carlo samples generated at the Z peak and scaled to data the luminosity (data collected during 1999-2000 at Z energies for detector calibration were also too low luminosity). The percentage difference between the number of data and Monte-Carlo selected events was 2% and this value was taken as the estimated uncertainty for the efficiency. The same procedure was repeated separately for the barrel and the endcap region and the errors found were 1.54% and 3.36% respectively. The systematic uncertainty introduced to the cross-section due to the efficiency was estimated as:

$$\Delta\sigma(eff) = \frac{\Delta\epsilon}{\epsilon} \quad \sigma \tag{4.16}$$

Luminosity

The error on the luminosity originates from various sources that can affect the measurement of small angle bhabhas and have been assessed at each energy by the OPAL collaboration . These errors can be classified in the following categories: experimental systematics (0.18-0.20%), uncertainty in the theoretical knowledge of the cross-section (0.12%) and uncertainty in the beam energy (0.04-0.05%). The error induced in the cross-section is then:

$$\Delta\sigma(\mathcal{L}) = \frac{\Delta\mathcal{L}}{\mathcal{L}} \quad \sigma \tag{4.17}$$

Feedthrough

The feedthrough systematic was estimated by modifying the $s^{'}/s$ value that defines the non-radiative region to slightly lower and higher values and comparing the feedthrough with the nominal value of $s^{'}/s = 0.7225$. The error on the cross section is given by:

$$\Delta\sigma(feed) = \frac{\Delta feed(pb)}{\epsilon} \tag{4.18}$$

	205 GeV		206 GeV	
$\Delta\sigma(Source)$	$s'/s > 0.01$	$s'/s > 0.7225$	$s'/s > 0.01$	$s'/s > 0.7225$
$\Delta\sigma(\Delta Eff_{stat})$	0.143	0.043	0.137	0.045
$\Delta\sigma(\Delta Eff_{sys})$	0.172	0.070	0.162	0.070
$\Delta\sigma(\Delta Bkg_{stat})$	0.043	0.019	0.053	0.026
$\Delta\sigma(\Delta Bkg_{sys})$	0.128	0.036	0.129	0.037
$\Delta\sigma(\Delta feed_{stat})$	0.000	0.005	0.000	0.005
$\Delta\sigma(\Delta feed_{sys})$	0.000	0.002	0.000	0.001
$\Delta\sigma(\Delta \mathrm{L}_{stat})$	0.009	0.004	0.007	0.003
$\Delta\sigma(\Delta \mathrm{L}_{sys})$	0.016	0.006	0.015	0.006
$\Delta\sigma(\Delta Interference)$	0.005	0.008	0.007	0.010
$\Delta\sigma(Statistical)$	0.556	0.289	0.416	0.224

Table 4.8: Systematic errors in *pb* for tau pairs at energies 205, 206 GeV for both inclusive and non-radiative cross-sections.

I/FSR interference

The error due to I/FSR interference was estimated by repeating the process for the calculation of $\mathrm{d}^2\sigma_{int}/\mathrm{d}m_{\mathrm{f\bar{f}}}\mathrm{d}\cos\theta$ as described in 4.6, but with an efficiency [54]:

$$E^{'}_{IFSR}(\cos\theta, m_{\mathrm{f\bar{f}}}) = \frac{1}{2}[\epsilon_{noint}(\cos\theta, m_{\mathrm{f\bar{f}}}) + \epsilon_{noint}(\cos\theta, \sqrt{s})] \tag{4.19}$$

Thus, the E_{IFSR} is taken as the average value formed by the efficiency in the specific bin $\epsilon_{noint}(\cos\theta, m_{\mathrm{f\bar{f}}})$ and the largest possible $\epsilon_{noint}(\cos\theta, \sqrt{s})$ at a given $\cos\theta$. This was motivated as follows [54]: the approximation $E_{IFSR} \simeq \epsilon_{noint}$ used in the calculation of the interference is good for $m_{\mathrm{f\bar{f}}} \simeq \sqrt{s}$, as possible radiation in this region is very likely to be FSR. The same is valid for $m_{\mathrm{f\bar{f}}} \simeq m_{\mathrm{Z}}$, as radiation in this case is very likely to be ISR. The energies between $m_{\mathrm{Z}} - \sqrt{s}$ are a mixture of radiative and non-radiative events, classes which have different efficiencies. For example in the rare case where $m_{\mathrm{f\bar{f}}}$

is small and there is an FSR photon emitted, the efficiency may be higher than the one estimated by $\epsilon_{noint}(\cos\theta, m_{\mathrm{f\bar{f}}})$. The error on the cross-section is :

$$\Delta\sigma(int) = \frac{\Delta\sigma^{'}(pb)}{\epsilon} \tag{4.20}$$

where $\Delta\sigma^{'} = \sigma_{int}(\epsilon_{noint}) - \sigma_{int}(E^{'}_{IFSR})$.

Asymmetry

The error on the asymmetry is estimated using Monte-Carlo events in order to have higher statistics. The uncertainty is assessed by comparing the asymmetry values derived using different methods to calculate $\cos\theta$: tracks, clusters or both of them (which is the normal method).

The above error is combined in quadrature with the error introduced to the asymmetry when I/FSR interference is changed. The latter is estimated by adding/subtracting the systematic error for I/FSR interference to the I/FSR correction and comparing the asymmetry derived with the normal one. The systematic errors for energies 205, 206 GeV are presented in table 4.8 and for the rest of the energies in the appendix A.

Chapter 5

Muon pairs Analysis

5.1 Introduction

The muon pair analysis was performed on the same high energy data set used for the tau pairs, collected during 1999-2000 at collision energies in the range 192-209 GeV. The initial state radiation has the same significance on the determination of the effective centre of mass energy $\sqrt{s'}$, signal definition and efficiency estimation. The definitions and methods used are not repeated here except where there is a difference with respect to the tau pairs analysis.

Initially, the selection used is described, which is almost the same as the one used at lower energies ([69], [70], [51], [71]), the only difference being the use of energetic calorimeter clusters in the determination of $\sqrt{s'}$. The Monte-Carlo estimations for efficiency and visible backgrounds follow and finally the results together with systematic checks are presented.

5.2 Selection of muon pairs

Muons are the only charged particles which travel through all detector layers. A high momentum track is associated with hits in the hadronic calorimeter and the muon chambers. For muons the electromagnetic calorimeter energy deposit is very small compared with their track momentum, as muons are minimum ionizing particles. More specifically, a high momentum track as described in the lepton pair preselection is considered a muon candidate if either:

- $N^{MUON}_{hits/track} \geq 2$, where $N^{MUON}_{hits/track}$ is the number of hits associated with the track in the muon chambers (ME, MB).
- $N^{HCAL}_{hits} \geq 4$, with $N^{HCAL}_{hits/layer} < 2$, where N^{HCAL}_{hits} is the number of hadronic calorimeter strip hits and $N^{HCAL}_{hits/layer}$ is the average number of hits per layer. In addition, for $|\cos\theta| < 0.65$, at least one hit is required in the last 3 layers of strips.
- the momentum of the charged track is greater than 15 GeV, with a total electromagnetic energy associated with the track less than 3 GeV.

An event is classified as a muon pair if there are at least two tracks within $|\cos\theta| < 0.95$ identified as muon candidates, separated by at least 320 mrad. For more than two candidates, the pair with higher total momentum is chosen. The lepton pair preselection as described in the tau analysis is applied. The number of charged tracks satisfying the track quality requirements of the preselection should be less than 3.

The determination of $\sqrt{s'}$ is performed in a similar way as to the tau pairs. The use of a possible energetic photon in planar events to improve the resolution of $\sqrt{s'}$ around the Z peak has the additional requirement for the angle between the photon and the nearest muon to be greater than 20 °. This is necessary to ensure that the assumption that the photon is due to ISR is reasonable. In the taus this is not necessary as the photon has to be outside the tau cone. The $\sqrt{s'}$ distribution for data taken with collision energy 206 GeV can be seen in figure 5.1.

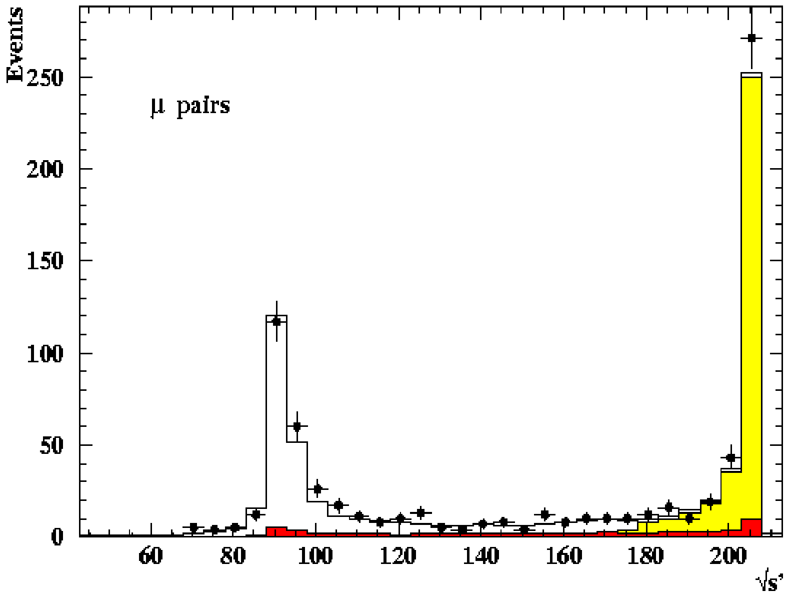

Figure 5.1: The $\sqrt{s'}$ distribution for muon pairs at 206 GeV. The open histogram is the Monte-Carlo prediction, the yellow(lightgrey) histogram is the prediction for non-radiative events and the red (dark grey) is the background contamination. The points are data.

A large fraction of the collision energy detected in the process $e^+e^- \rightarrow \mu^+\mu^-(\gamma)$ is detected: the momentum of the two muons is measured by the central tracking detectors, while the photon may travel undetected down the beam pipe or leave its energy deposit in the electromagnetic calorimeter. In contrast, important backgrounds such as tau pairs have large missing energy as mentioned in the tau pair analysis. Also in the two photon process $e^+e^- \rightarrow e^+e^-\mu^+\mu^-$, it is likely that the electron and positron will be lost in the beam pipe, carrying a large fraction of the collision energy.

The visible energy E_{vis}, defined as the sum of the momentum of the two muons normalized to the collision energy and the energy of the most energetic calorimeter cluster, can be seen in figure 5.2. When all particles of the signal process are detected, E_{vis} is close to one. The peak in the centre of the distribution is mainly due to radiative return to Z events where the photon was not detected. As the centre of mass energy increases, the energy of the photon also increases, moving this peak towards lower

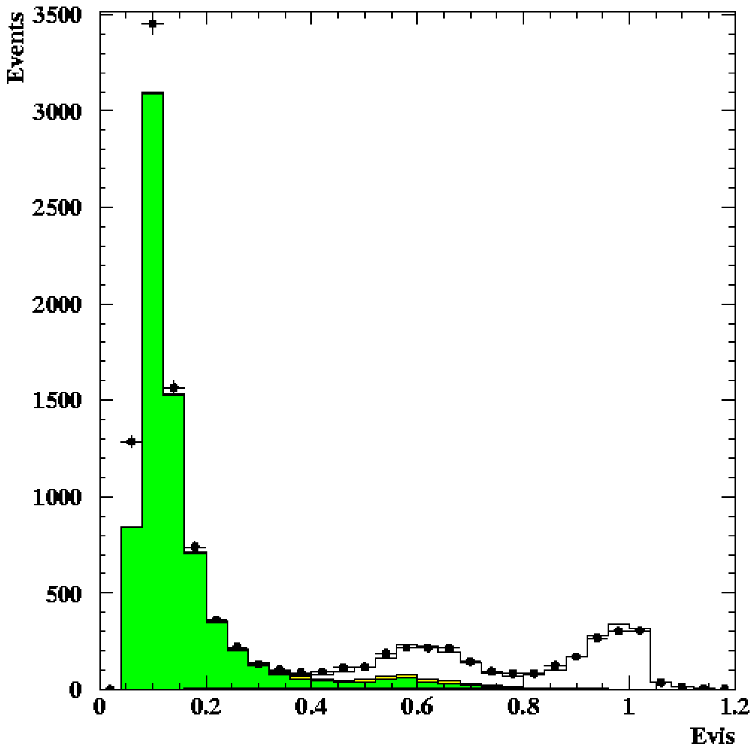

Figure 5.2: The visible energy E_{vis} for muon pair candidates for all energies combined. The open histogram represents the signal Monte-Carlo events and the green (grey) is the two photon background. The points are data.

energies. The visible energy is required to be more than the lower edge of the central peak:

$$E_{vis} > 0.35 + \frac{m^2(Z^0)}{2s} \tag{5.1}$$

In addition, for the non-radiative events, the effective mass of the two muon candidates is required to be slightly above the Z peak:

$$\mathrm{M}_{\mu\mu} > \sqrt{\mathrm{M}_{\mathrm{Z}}^2 + 0.1s} \tag{5.2}$$

Inclusive events must satisfy a lower cut for the $\mathrm{M}_{\mu\mu}$, in order to include the Z peak, or have even higher visible energy:

$$\mathrm{M}_{\mu\mu} > 70 \quad GeV \quad \text{or,}$$

$$E_{vis} > 0.75 + \frac{m^2(Z^0)}{2s}$$

5.3 Cosmic Ray studies

The study of cosmic rays contamination is significant for the muon pair analysis due to their similarities with the signal process and their contribution to the total systematic error of the muon pair cross-section (for both inclusive and non-radiative samples it is the dominant systematic error).

The rejection of cosmic rays is based, as for the tau pairs, on imposing space-time constraints to ensure that the event originates from a collision. More specifically, an event is selected if there is at least one TOF hit in the barrel region within 10 ns of the expected time of flight for a particle travelling at the speed of light and originating from the vertex (figure 5.3 (b)(c)). In addition, for events with two back-to-back TOF hits the difference between them should be less than 8 ns (figure 5.3 (a)). Events with no TOF hits in the barrel can be recovered by tight vertex cuts (figure 5.4 (a)):

$$|\sum z0| < 10\,\mathrm{cm}, \sum |d0| < 0.08\,\mathrm{cm}$$

In the endcap the cuts are relaxed due to the poorer position resolution but are tighter than the endcap vertex requirements for the tau pair analysis (figure 5.4 (d)):

$$|\sum z0| < 50\,\mathrm{cm}, \sum |d0| < 0.6\,\mathrm{cm}$$

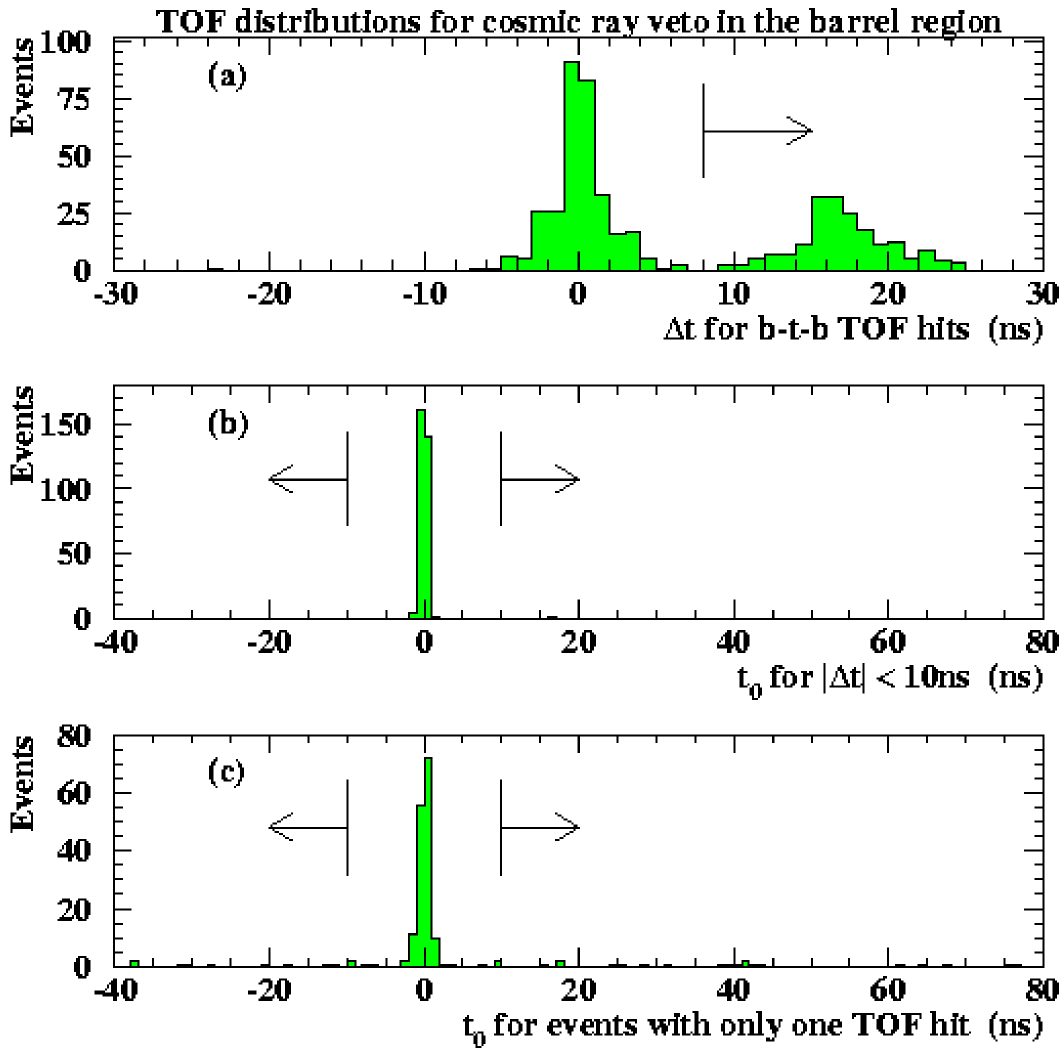

Figure 5.3: Time-Of-Flight plots in the barrel region for 206 GeVdata:

(a) The difference Δt for events with two back-to-back TOF counter hits,

(b) The corrected measured time t_0 for events passing the Δt cut,

(c) The corrected measured time t_0 for events with a only one TOF counter hit.

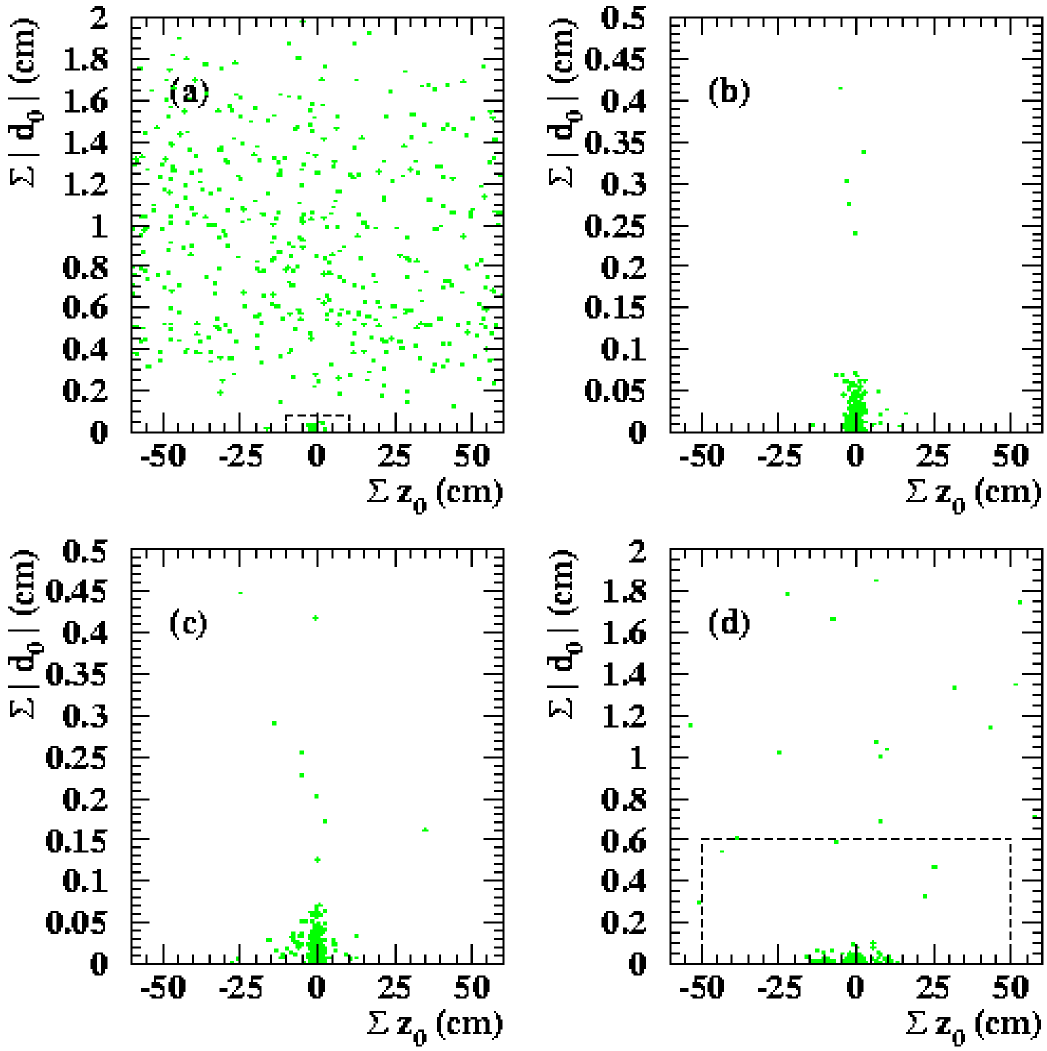

Figure 5.4: $\sum|d0|$ versus $\sum z0$ for 206 GeV data

(a) Events in the barrel region that fail the TOF cuts,

(b) Events in the barrel region that pass TOF cuts having back-to-back hits,

(c) Events in the barrel region that pass TOF cuts having a single TOF counter hit,

(d) Events in the endcaps.

The systematic error on the cosmic rays is assessed by modifying the time and vertex constraints in order to check the number of events that are close to the cuts. The total number of events found close to the cuts for all energies combined ΔN is then divided by the total integrated luminosity to estimate an 'average' cross-section for cosmic rays. The error on the muon pairs cross-section is then :

$$\Delta\sigma(cosmic) = \frac{\Delta N}{\epsilon \quad \int \mathcal{L}\mathrm{d}t} \tag{5.3}$$

5.4 Background and Efficiency estimation from Monte Carlo

The background and efficiency estimation is performed in a similar way to the tau pair analysis. The total background and efficiencies can be seen in table 5.1. No significant variations at single energy points are observed from statistical fluctuations.

The efficiencies range from 73% to 74.8% for the inclusive events and from 87.8% to 87.1% for the non-radiative selection. Table 5.2 gives the visible cross-sections for all background processes as predicted by Monte-Carlo simulation at 206 GeV. For the inclusive events the total background is about 9.2%. The biggest contribution is from four fermion events ($\sim 51.3\%$), followed by the two photon process $\mathrm{e^+e^-} \rightarrow \mathrm{e^+e^-}\mu^+\mu^-$ $\sim 30.6\%$ and tau pairs ($\sim 18\%$). The level of background in the non-radiative selection is significantly lower ($\sim 3.6\%$) with an additional feedthrough percentage of ($\sim 1.4\%$). The four fermion contribution to the background is $\sim 47.8\%$, the two photon process $\mathrm{e^+e^-} \rightarrow \mathrm{e^+e^-}\mu^+\mu^-$ is $\sim 15.8\%$ and tau pairs $\sim 36.4\%$.

Efficiencies and backgrounds 192 - 206 GeV				
Energy		Efficiency (%)	Background (pb)	Feedthrough (pb)
192 GeV	$s'/s > 0.01$	74.81±0.26±0.75	0.497±0.016±0.026	–
	$s'/s > 0.7225$	88.02±0.26±0.88	0.073±0.005±0.006	0.045±0.003±0.004
196 GeV	$s'/s > 0.01$	74.27±0.26±0.74	0.524±0.016±0.027	–
	$s'/s > 0.7225$	88.06±0.26±0.88	0.074±0.005±0.006	0.041±0.002±0.003
200 GeV	$s'/s > 0.01$	73.74±0.27±0.74	0.487±0.015±0.026	–
	$s'/s > 0.7225$	87.78±0.26±0.88	0.087±0.005±0.007	0.037±0.002±0.004
202 GeV	$s'/s > 0.01$	73.39±0.27±0.73	0.493±0.015±0.026	–
	$s'/s > 0.7225$	88.11±0.26±0.88	0.086±0.005±0.006	0.034±0.002±0.002
205 GeV	$s'/s > 0.01$	73.23±0.27±0.73	0.472±0.014±0.026	–
	$s'/s > 0.7225$	88.00±0.26±0.88	0.089±0.005±0.006	0.031±0.002±0.003
206 GeV	$s'/s > 0.01$	73.04±0.27±0.73	0.465±0.014±0.025	–
	$s'/s > 0.7225$	87.99±0.26±0.88	0.086±0.005±0.006	0.033±0.002±0.003

Table 5.1:

Efficiencies, backgrounds and feedthrough for each energy from 192 up to 206 GeV. The first error is statistical and the second systematic.

	Physics process	Generator	$s'/s > 0.01$ σ (pb)	$s'/s > 0.7225$ σ (pb)
2-fermion	$\mu^+\mu^-$	KORALZ		
	$\tau^+\tau^-$	KORALZ	0.0838±0.0033	0.0313±0.0020
	e^+e^-	BHWIDE	0.0000±0.0000	0.0000±0.0000
	$q\overline{q}$	PYTHIA	0.0000±0.0000	0.0000±0.0000
2-photon	$e^+e^-q\overline{q}$ tagged	HERWIG	0.0000±0.0000	0.0000±0.0000
	$e^+e^-q\overline{q}$ untagged	PHOJET	0.0000±0.0000	0.0000±0.0000
	$e^+e^-c\bar{c}$	PYTHIA	0.0000±0.0000	0.0000±0.0000
	$e^+e^-e^+e^-$	VERMASEREN	0.0000±0.0000	0.0000±0.0000
	$e^+e^-\mu^+\mu^-$	VERMASEREN	0.1424±0.0118	0.0136±0.0036
	$e^+e^-\tau^+\tau^-$	VERMASEREN	0.0000±0.0000	0.0000±0.0000
4-fermion	$e^+e^-e^+e^-$	GRC4F	0.0000±0.0000	0.0000±0.0000
	$e^+e^-\mu^+\mu^-$	GRC4F	0.0672±0.0034	0.0005±0.0003
	$e^+e^-\tau^+\tau^-$	GRC4F	0.0004±0.0003	0.0002±0.0002
	$e^+e^-q\overline{q}$	GRC4F	0.0000±0.0000	0.0000±0.0000
	$q\overline{q}q\overline{q}$	GRC4F	0.0000±0.0000	0.0000±0.0000
	$l^+l^-q\overline{q}$	GRC4F	0.0006±0.0003	0.0001±0.0001
	$l^+l^-l^+l^-$	GRC4F	0.1705±0.0058	0.0404±0.0028

Table 5.2: Monte Carlo sample used in efficiency and background estimates at 206 GeV and the background estimates as cross-sections for both inclusive and non-radiative samples.

5.5 Cross-sections, Angular distributions and Asymmetries

The sample for all data collected during the years 1999-2000 is divided into the same 6 energy bins described in table 4.5. The data quality minimum requirements are given in table 5.3.

Status	CV	CJ	TB	EB	EE	ME
Detector	2	2	2	2	2	0
Trigger	0	2	2	0	0	2

Table 5.3: The status requirements for the muon pair analysis

The calculation of the cross-sections is performed using the same procedure as that described in section 4.7.2: the total number of events is divided by luminosity and the background, I/FSR interference and feedthrough cross-sections are subtracted. Finally, it is corrected by the efficiency estimated from Monte-Carlo. The measured cross-sections for all energies can be seen in table 5.4 and figure 5.5. The agreement with the Standard Model theoretical predictions is good.

The asymmetry is calculated using the same procedure as that described in section 4.7.3: the $-Q\ cos\theta$ distribution (figures 5.6, 5.7) is corrected on a bin-by bin basis for background, I/FSR interference and efficiency. A final correction to the full-solid angle is applied using ZFITTER. For the asymmetry measurement the value of θ is calculated using CV/CZ detectors if available and muon chambers otherwise. The measured asymmetries can be seen in table 5.5 and plotted in figure 5.8. The agreement with Standard Model predictions is also good.

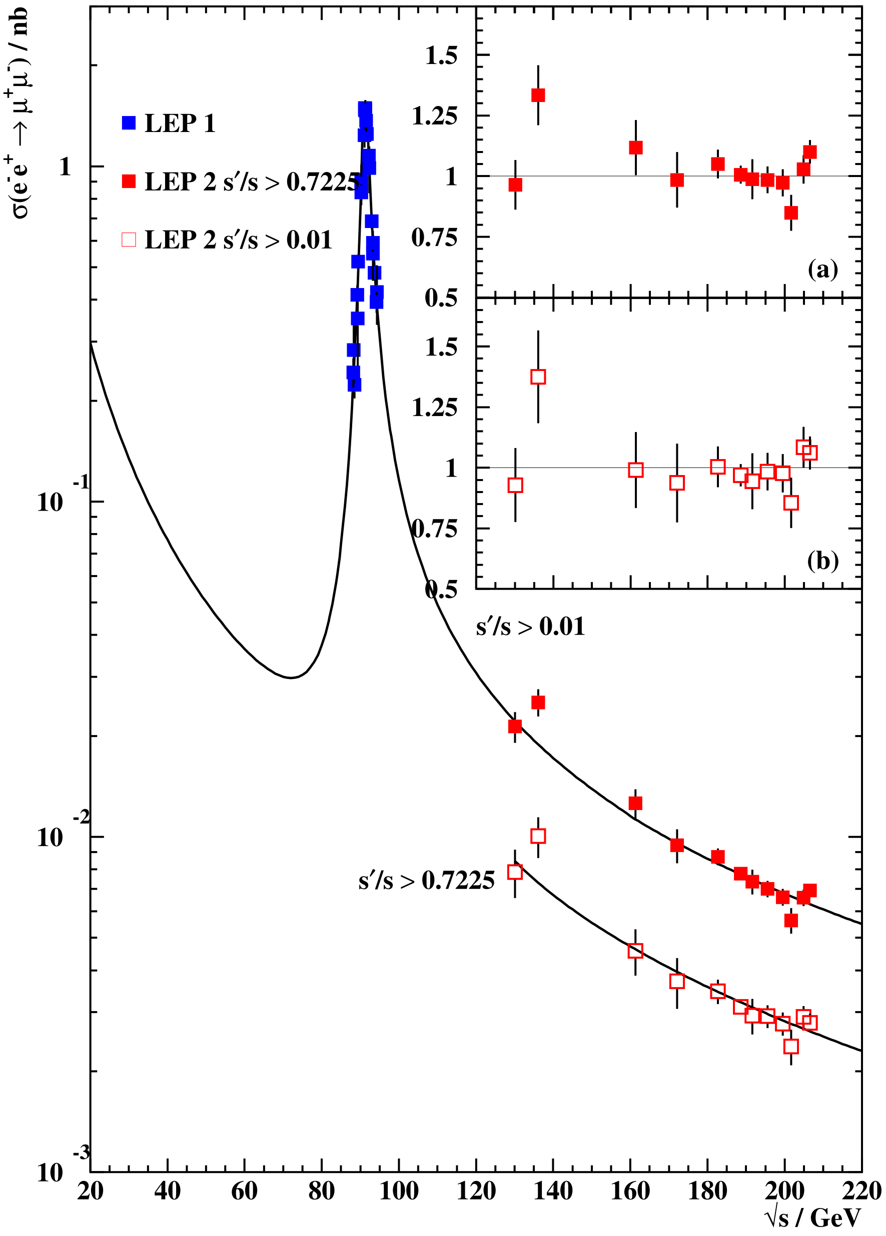

Figure 5.5: The cross-section measurements for the muon pair analysis as a function of $\sqrt{s}$ for both radiative and inclusive samples. The solid line is the Standard Model prediction as calculated by ZFITTER. The insets show the ratio of the measurements and predicted cross-sections for (a) $s^{'}/s > 0.7225$ and (b) $s^{'}/s > 0.01$.

Cross-sections					
Energy		$\int \mathcal{L}\mathrm{d}t$ (pb^{-1})	Events	σ (pb)	σ^{SM} (pb)
192	$s'/s > 0.01$	29.21	176	7.36±0.61±0.13	7.45
	$s'/s > 0.7225$		80	2.93±0.35±0.09	3.10
196	$s'/s > 0.01$	76.01	437	7.00±0.37±0.13	7.11
	$s'/s > 0.7225$		207	2.92±0.21±0.09	2.97
200	$s'/s > 0.01$	78.04	421	6.61±0.36±0.13	6.80
	$s'/s > 0.7225$		203	2.77±0.21±0.09	2.84
202	$s'/s > 0.01$	37.42	174	5.63±0.48±0.12	6.64
	$s'/s > 0.7225$		84	2.37±0.28±0.08	2.77
205	$s'/s > 0.01$	78.57	418	6.59±0.35±0.13	6.41
	$s'/s > 0.7225$		213	2.90±0.21±0.09	2.68
206	$s'/s > 0.01$	134.54	746	6.93±0.28±0.13	6.29
	$s'/s > 0.7225$		351	2.79±0.16±0.09	2.63

Table 5.4: Cross-sections for energies 192-206 GeV for both inclusive and non-radiative samples and the Standard Model predictions as calculated by ZFITTER. The first error on the cross-section is statistical and the second systematic.

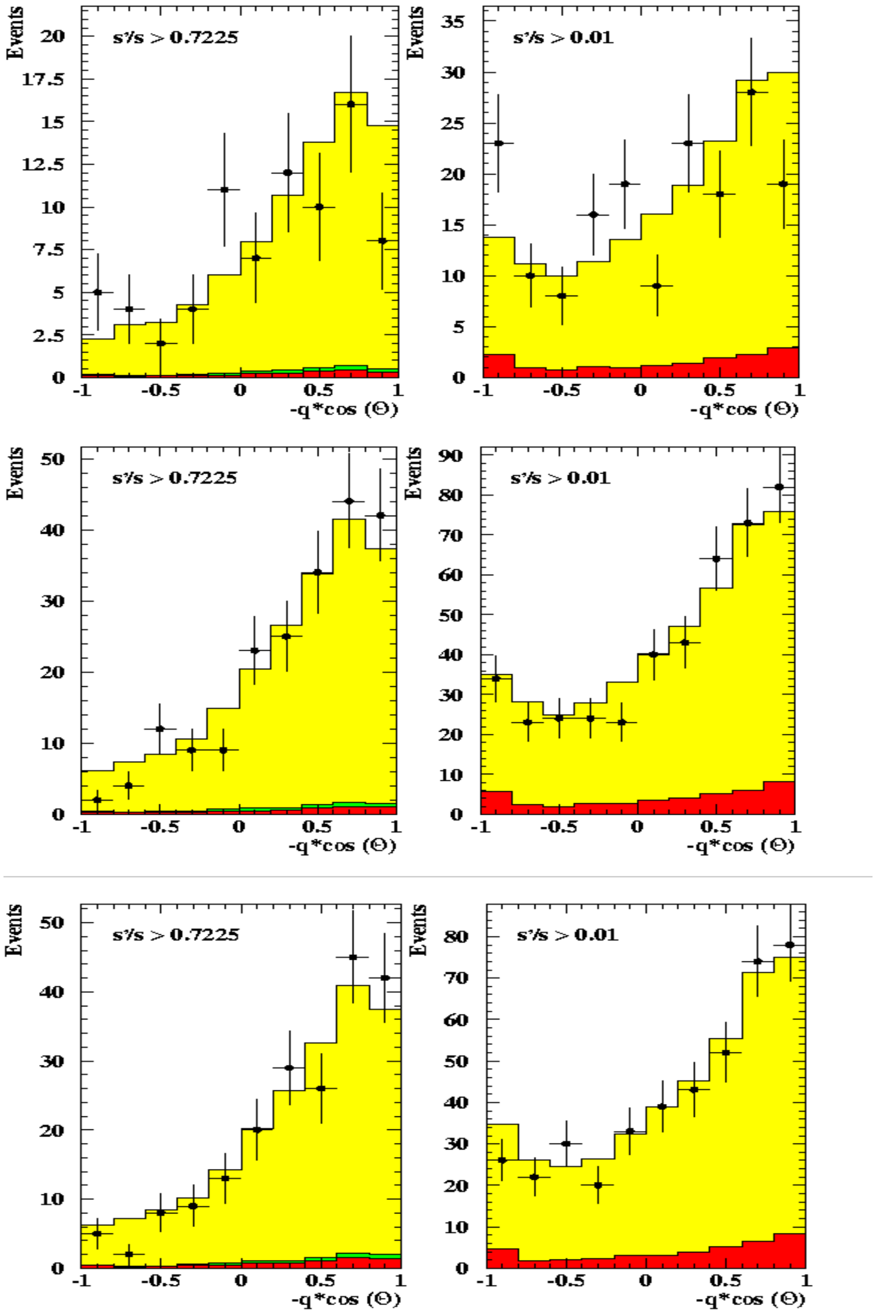

Figure 5.6: The $-Q\ cos\theta$ distributions at $\sqrt{s'}$=192 GeV (upper), 196 GeV (medium), 200 GeV (lower). The plots on the left are for the non-radiative samples and on the right are for the inclusive samples. The yellow (light grey) histogram is the prediction for the muon pairs from Monte-Carlo. The green (medium grey) and red (dark grey) histograms are the predictions for feedthrough and background contributions respectively and the points represent data.

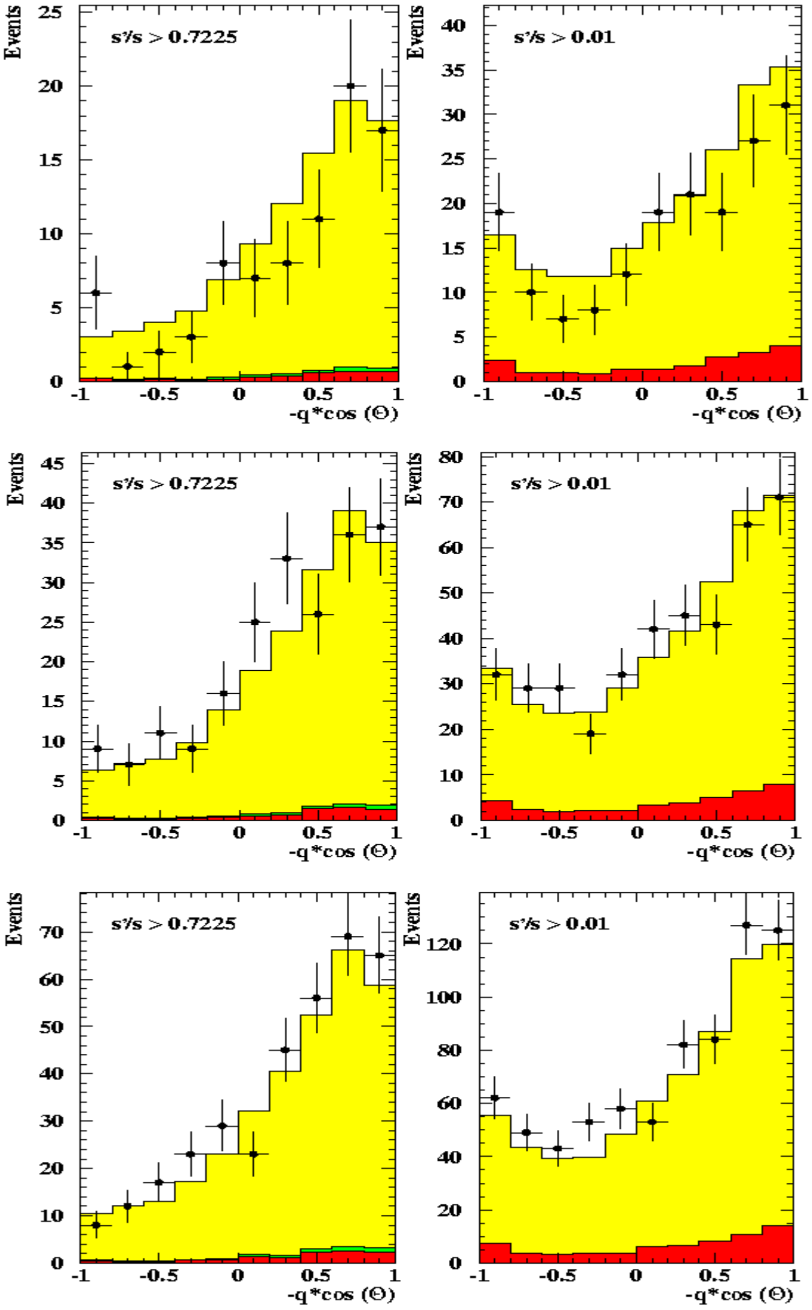

Figure 5.7: The $-Q\ cos\theta$ distributions at $\sqrt{s'}$=202 GeV (upper), 205 GeV (medium), 206 GeV (lower). The plots on the left are for the non-radiative samples and on the right are for the inclusive samples. The colour scheme is the same as in figure 5.6.

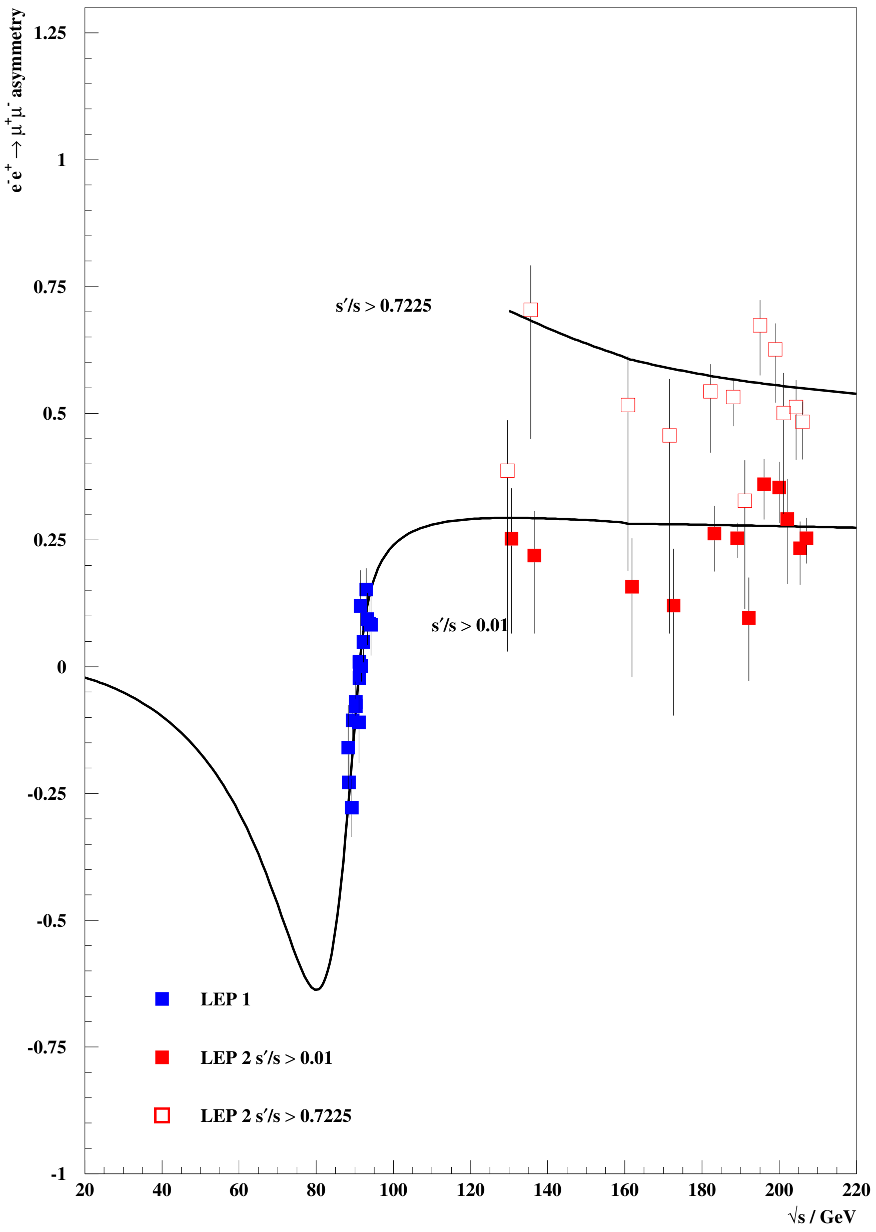

Figure 5.8: The measured asymmetries for the muon pair process as as function of $\sqrt{s}$ for both inclusive and radiative samples. The solid line is the Standard Model prediction as calculated by ZFITTER.

Asymmetries					
	Energy	N_{F}	N_{B}	A_{FB}	A_{FB}^{SM}
192 GeV	$s'/s > 0.01$	206.48	169.00	$0.10^{+0.08}_{-0.12} \pm 0.01$	0.28
	$s'/s > 0.7225$	102.90	53.12	$0.33^{+0.11}_{-0.21} \pm 0.02$	0.56
196 GeV	$s'/s > 0.01$	628.77	287.90	$0.36^{+0.05}_{-0.07} \pm 0.01$	0.28
	$s'/s > 0.7225$	339.73	70.73	$0.67^{+0.05}_{-0.10} \pm 0.02$	0.56
200 GeV	$s'/s > 0.01$	607.00	281.87	$0.35^{+0.05}_{-0.07} \pm 0.01$	0.28
	$s'/s > 0.7225$	318.97	77.35	$0.63^{+0.06}_{-0.10} \pm 0.01$	0.55
202 GeV	$s'/s > 0.01$	237.36	127.24	$0.29^{+0.08}_{-0.13} \pm 0.01$	0.28
	$s'/s > 0.7225$	122.20	42.09	$0.50^{+0.10}_{-0.20} \pm 0.01$	0.55
205 GeV	$s'/s > 0.01$	548.45	334.80	$0.23^{+0.05}_{-0.07} \pm 0.01$	0.28
	$s'/s > 0.7225$	313.32	104.43	$0.51^{+0.06}_{-0.10} \pm 0.01$	0.55
206 GeV	$s'/s > 0.01$	1013.42	591.42	$0.25^{+0.04}_{-0.05} \pm 0.01$	0.28
	$s'/s > 0.7225$	508.12	183.01	$0.48^{+0.05}_{-0.07} \pm 0.01$	0.55

Table 5.5: The corected numbers of forward (N_{F}) and backward (N_{B}) events and the measured asymmetry values at each energy are shown. The measured asymmetry values include corrections for background and efficiency, and are corrected to the full solid angle. The first error is statistical and the second is systematic. The final column shows the Standard Model predictions as calculated by ZFITTER.

5.6 Systematic Errors

The estimation of systematic errors for the luminosity, feedthrough and I/FSR interference is performed using the same methods as in the tau pair analysis. The principles for the errors in efficiency, backgrounds and asymmetry are similar, but are discussed here due to some differences with respect to the tau pair analysis.

Efficiency

The systematic error on the efficiency was estimated using LEP1 data, as for the tau pairs. The visible energy requirement was changed to the value used at LEP1 ($E_{vis} > 0.6$), as the value calculated by equation 5.1 is too close to the Z peak. The selection was applied to data collected during 1994 and Monte-Carlo generated at the Z peak. The percentage difference between the number of selected data and Monte-Carlo events was estimated to be 0.95% . The same procedure was repeated separately for the barrel and endcap regions and the errors found were 0.42% and 2.06% respectively.

Background

The systematic error for the two-photon process $e^+e^- \rightarrow e^+e^-\mu^+\mu^-$ was estimated from the visible energy plot (figure 5.2) using the same method as for the tau pairs background systematic error estimate: the number of selected data and Monte-Carlo events for all energies combined were compared in the lower E_{vis} region (0.08-0.4), giving a percentage error of $\sim$ 6.8%. The four-fermion and tau pairs uncertainty was estimated using the acoplanarity and PTclusters observables respectively. The percentage errors were $\sim$ 15.9%, for the tau pairs and $\sim$ 8% for the four fermion processes.

	205 GeV		206 GeV	
$\Delta\sigma(Source)$	$s'/s > 0.01$	$s'/s > 0.7225$	$s'/s > 0.01$	$s'/s > 0.7225$
$\Delta\sigma(\Delta Eff_{stat})$	0.024	0.008	0.026	0.008
$\Delta\sigma(\Delta Eff_{sys})$	0.066	0.029	0.069	0.028
$\Delta\sigma(\Delta Bkg_{stat})$	0.019	0.006	0.019	0.006
$\Delta\sigma(\Delta Bkg_{sys})$	0.035	0.007	0.035	0.007
$\Delta\sigma(\Delta feed_{stat})$	0.000	0.002	0.000	0.002
$\Delta\sigma(\Delta feed_{sys})$	0.000	0.004	0.000	0.003
$\Delta\sigma(\Delta \mathrm{L}_{stat})$	0.009	0.004	0.007	0.003
$\Delta\sigma(\Delta \mathrm{L}_{sys})$	0.015	0.006	0.015	0.006
$\Delta\sigma(\Delta N_{cosmic})$	0.095	0.079	0.095	0.079
$\Delta\sigma(\Delta Interference)$	0.003	0.011	0.003	0.010
$\Delta\sigma(Statistical)$	0.354	0.210	0.277	0.157

Table 5.6: Systematic errors in *pb* for muon pairs at energies 205, 206 GeV.

Asymmetry

The systematic uncertainty on the assymetry was assessed by comparing the asymmetry values derived using different methods for $\cos\theta$ calculation, with the default method. The later uses CV/CZ detectors if availiable and muon chambers otherwise. The other methods used for $\cos\theta$ are: using central tracking information for both barrel and endcap, demanding CV/CZ in the barrel and good quality tracks and finally using CV/CZ if availiable and muon chambers otherwise with the additional requirement for the tracks to have good quality (enough detector hits). The error introduced by I/FSR was estimated with the same procedure already desribed in 4.8. The systematic errors for energies 205, 206 GeV are presented in table 5.6 and for the rest of the energies in the appendix A.

Chapter 6

The Forward Jet Triggering for ATLAS Detector

6.1 The LHC Collider and the ATLAS Detector

The LHC (Large Hadron Collider) is a 7+7 TeV proton proton collider designed to be installed in the 27 km circumference LEP tunnel in CERN (figure 6.1). The injector consists of a 50 MeV Linac, the 1.9 GeV proton booster, the 26 GeV PS (Proton Synchrotron) and the 450 GeV SPS (Super Proton Synchrotron). The design luminosity is $10^{34}\ cm^{-2}\ s^{-1}$. The total energy for new physics is much less than 14 TeV (centre of mass energy), due to the fact that the proton's constituents (partons) carry only a fraction of proton's momentum and significant energy is lost to soft scattering of other partons.

The basic physics studies are similar to the ones performed at LEP: Higgs boson search, precision measurements of the Standard Model parameters and supersymmetric searches. More specifically, the Standard Model mechanism to allow gauge bosons to acquire mass without destroying the gauge invariance of the Lagrangian, the Higgs mechanism, is still not verified experimentally: the excess observed at LEP is not inconsistent with the background hypothesis as explained in 3.2.

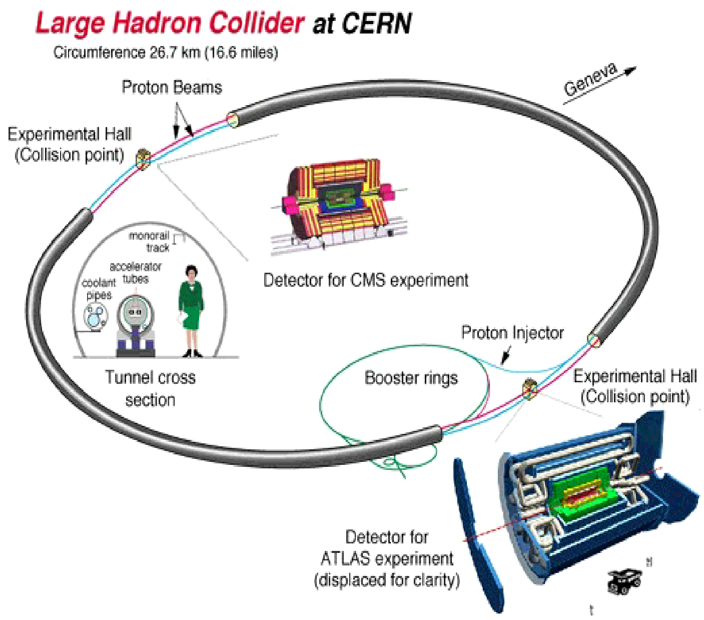

Figure 6.1: The Large Hadron Collider

The major searches for physics beyond the standard model will be focused on searches for supersymmetric particles. If supersymmetric particles exists on the electroweak scale, they are expected to be seen in the ATLAS experiment. Other interesting physics are high precision bottom and top quark physics, measurement of the W mass with an error of 2 MeV as well as other electroweak parameters measurement such as triple gauge couplings.

6.1.1 ATLAS detector

The overal detector layout is shown in figure 6.2. It consist of the magnet, the high resolution inner detector (ID), the liquid argon (LAr) electromagnetic calorimeter (EM), the hadronic calorimeters and the muon spectrometer [72]. A sophisticated trigger and data acquisition system is required to reduce the data stored to an acceptable level without losing interesting physics events. The magnet system consists of an inner thin superconducting solenoid surrounding the inner detector and large superconducting air-core toroids. As a coordinate system the the following convention is used: The origin is the collision point. The z-axis is defined to be the beam axis. The azimuthal

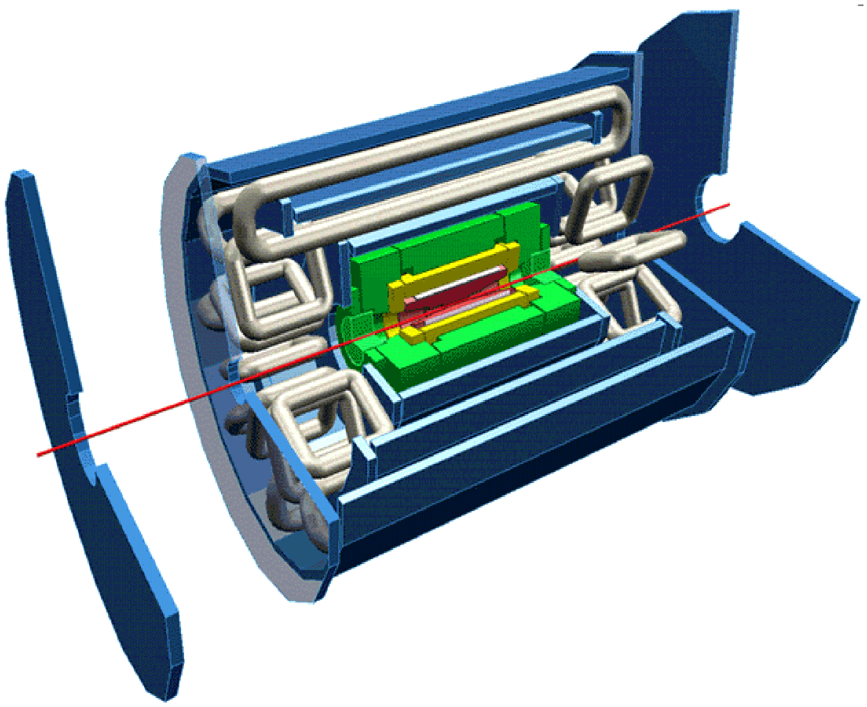

Figure 6.2: The ATLAS detector

angle ϕ and the radius R (defined as the distance from the beam axis) are used to define a point in the plane transverse to the beam axis. The above define a point in cylindrical coordinates. It is also useful to use spherical coordinates by using the polar angle θ or even better in terms of the Lorentz invariant pseudo-rapidity:

$$\eta = -\ln \tan \frac{\theta}{2}$$

6.1.2 Inner Detector

The inner detector is designed to measure the paths of electrically charged particles. It is contained in the central solenoid (2 Tesla), so that the particle paths are curved. The curvature of the track allows the measurement of the momentum and sign of electric charge. The inner tracker combines high resolution detectors at the inner radii with continuous tracking elements at the outer radii (figure 6.3).

The requirements for momentum and vertex resolution make necessary the use of fine granularity detectors. The main reason for that is the very large track density expected. The precision requirements have to balance the high cost. So three different technologies are used:

- pixel detector
- silicon strip detectors (semiconductor tracker or SCT)
- continuous straw tube tracking (transition radiation tracker or TRT)

Pixel detector

It is designed to provide a very high granularity for the highest track density, close to the beam pipe. It consists of thin layers of silicon subdivided into rectangular regions ('pixels'), of dimension 50 by 300 microns. Each time a particle transverses such a region, pairs of holes and electrons are created, giving an electrical pulse. Closer to the collision point pixels are placed cylindrically (three barrel layers) and for large $|\eta|$ they are located on disks (five on each side) in order to reduce the thickness of the material particles pass through and to improve position resolution.

Semiconductor Tracker (SCT)

This subdetector is also used for position measurements and is located a little further from the collision point. It consists of layers of silicon microstrip detectors, each covering an area of $6.36 \times 6.40\,\mathrm{cm}^2$ with 768 readout strips of 80 microns pitch. Each layer has two sets of strips running at an angle of 2.3 degrees relative to each other. When a charged particle transverses the two set of strips, it gives signals to a strip in each set. By the intersection of those struck strips, we have a very accurate position measurement. Again closer to the collision point the strips are placed cylindrically

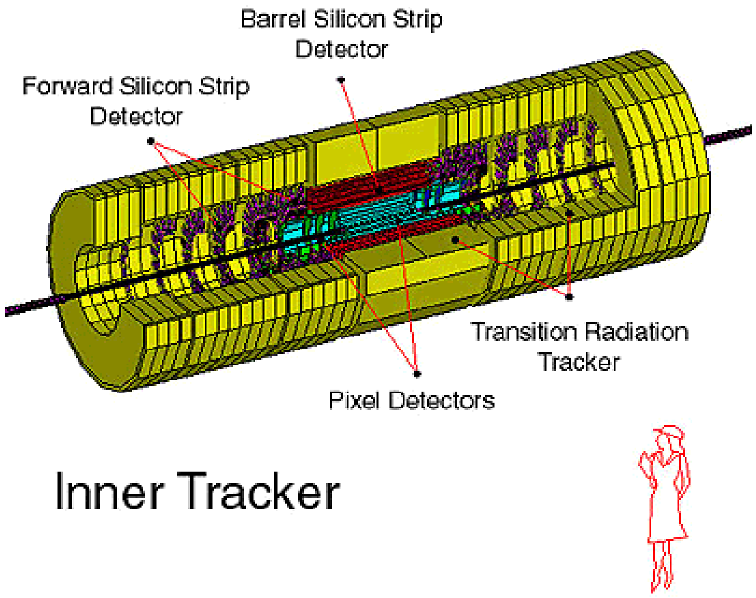

Figure 6.3: The Inner Tracker Detector

(eight layers), but for larger $|\eta|$ they are located on disks (9 end-cap wheels on each side). It has much less material per track point and a lower cost compared to the pixel detector.

Transition radiation tracker (TRT)

It consists of a large number of straws filled with a $Xe/CF_4/CO_2$ gas mixture. Each straw has a wire down its axis. With high voltage between the wire and straw wall, charged particles transversing the straw induce electrical pulses that are recorded (gas-wire drift detectors). In the center section the tubes run parallel to the beam pipe but again for large $|\eta|$, they are positioned radially.

When a particle traverses interfaces between materials with different refractive indices (in this case solid material and gas) with a speed extremely close to the speed of light, X-rays are generated (Transition Radiation). As electrons have small mass compared to other charges particles, they have a speed very close to the speed of light, so they produce transition radiation X-rays. The X-rays interact with the gas giving larger pulses than other charged particles. This way, we can determine wether that the particle traversing the detector is an electron (electron IDentification).

The silicon pixel and strip detectors provide about 10 points of the track with an accuracy 10-20 microns. The TRT provides further 36 points with an accuracy of 150 microns. Software is used to convert all these signals into tracks (pattern recognition) and also to determine momentum and sign of charge.

6.1.3 Calorimeters

The ATLAS calorimeters are shown in figure 6.4. There are three major sections: electromagnetic calorimeter using liquid argon technology (LAr), the hadronic calorimeter using a mixture of LAr for the endcaps ('wheels' perpendicular to the beam axis) and scintillating tiles for the barrel, as well as the Forward calorimeter (also LAr).

The Electromagnetic Calorimeter

The electromagnetic calorimeter measures the total energy of electrons, positrons and photons. When these particles interact with an absorbing medium, they lose momentum, producing photons. These photons give positron-electron pairs (pair creation) and these further interact with the absorbing medium, producing more photons. This cascading sequence is called electromagnetic shower. The energy of the initial particle is transformed into the rest masses of a large number of electron-positron pairs (the number is proportional to the kinetic energy of the initial particle). Between several plates of absorbing medium, another medium is placed (eg. liquid argon) to sense the presence of the pairs created. Electrons or positrons cause an ionisation of some of the atoms, leaving ions in their place. The medium is subjected to a large electric field, so electrons are collected by the positive side of the electric field used, producing a current pulse proportional to the number of electron-positron pairs created.

The electromagnetic calorimeter is designed to use lead absorber plates in a liquid argon ionisation medium. Liquid argon technology is radiation resistant, provides long term stability of the detector response, excellent hermeticity, as well as good energy resolution. In both barrel and endcap regions the absorber plates are of an accordion geometry to ensure hermeticity. In the barrel the plates are arranged radially in ϕ, whereas in the endcaps they lie in parallel to the beam axis. The granularity depends on the depth in order to keep a balance between cost and precision.

The electromagnetic calorimeter is preceded in the barrel by a presampler detector layer, located immediately behind the cryostat inner wall, in order to correct the energy loss in the material in front of the electromagnetic calorimeter and to contribute to the measurement of electromagnetic showers.

The Hadronic Calorimeter

It measures the total energy of hadrons (protons, neutrons, pions and kaons). The hadronic calorimeter is based on the same principle as the electromagnetic one: The hadrons interact with the dense material used as the absorbing medium, producing a hadronic shower (photons and electrons have already stopped in the electromagnetic calorimeter). This shower consists of many low energy protons, neutrons, pions and other hadrons. To sense the shower two different technologies were used: In the barrel plastic scintillator plates are used embedded in an iron absorber which also serves as a flux return (tile calorimeter). The shower when traversing the scintillating tiles, causes them to emit light proportional to the incident energy. The light is converted by photomultipliers into an electrical pulse. The hadronic tile calorimeter is subdivided into three sections: a central barrel and two extended barrels, with gaps between them to allow space for the cryogenics feedthroughs for the electromagnetic calorimeter and services for the inner detector. The hadronic tile calorimeter surrounds the cryostats which house the LAr sections of the calorimeter. In the two endcaps the same LAr technology as the electromagnetic calorimeter is used, but copper plates are used as an absorbing medium.

The transverse energy is an important concept for the calorimetry, as for objects near the speed of light the jet energy/direction can easily be converted to transverse momentum. The conservation of transverse momentum is the only way to detect the presence of neutrinos (by the calculating the missing momentum), as in the direction of the beam pipe there is a hole (the transverse energy is defined as the energy times sinθ, where θ is the angle between the particle's momentum and the beam axis). Also the gluons and quarks produced quickly pick-up additional quark-antiquark pairs and emerge as jets. The jet energy and jet direction represent the energy and direction of the initial quark/gluon.

Integrated Forward Calorimeter

The integrated forward calorimeter uses the same LAr technology and it is used to measure electrons, photons and hadrons. Due to the fact that in the forward region covering high values of $|\eta|$, the radiation is much higher, a novel rod and tube structure is used which allows the LAr gap to be very small. This ensures rapid charge collection and high density.

6.1.4 Muon Spectrometer

Muons are the only particles (except neutrinos) that reach the muon spectrometer, due to the fact that they have about 200 times more mass than the electrons and do not interact via the strong force. The muon spectrometer is shown on figure 6.5. It uses large superconducting air-core toroid magnets to curve the path of muons in order to measure their momentum and the sign of charge. The spectrometer has separate trigger and high precision tracking chambers. For small $|\eta|$ the magnetic field is provided by the large barrel toroid. Two smaller end-cap magnets inserted into both ends of the barrel toroid provide the bending for larger $|\eta|$. The barrel consists of three cylindrical superlayers. The endcaps are also divided into three layers, perpendicular to the beam axis.

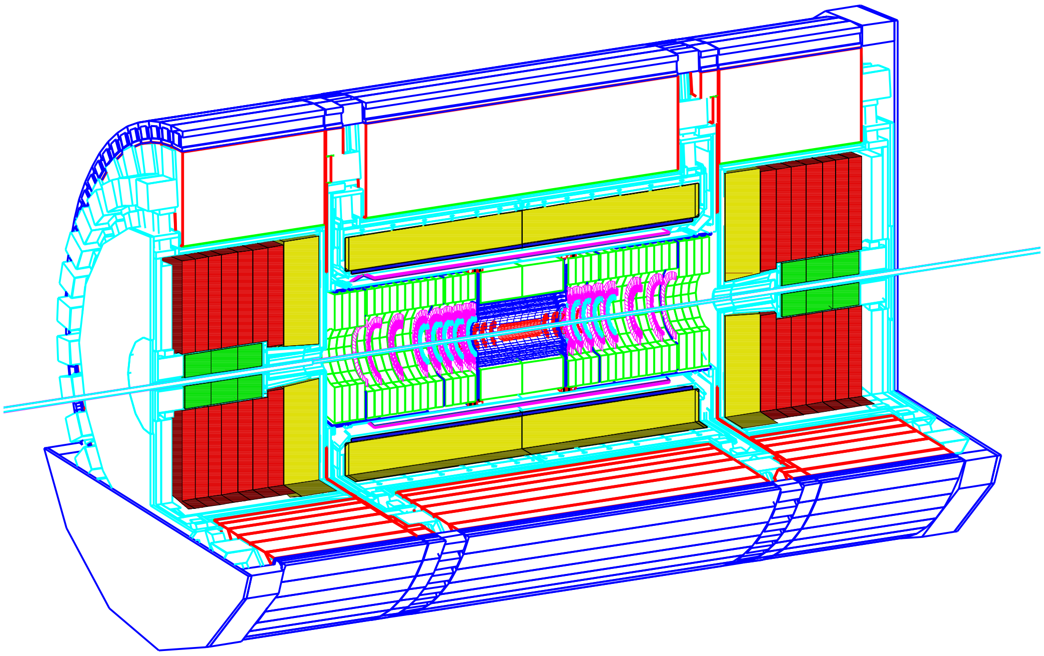

Figure 6.4: The Calorimeters

A major role in the design of the spectrometer was played by the high level of particle fluxes, requiring different levels of rate capability, granularity and radiation hardness for different parts of the detector. For precision measurements covering most $|\eta|$, Monitored Drift Tubes (MDT) are used. Close to the interaction point, at large $|\eta|$, Cathode Strip Chambers (CSC) are used with higher granularities. Finally, for the trigger system, Resistive Plate Chambers (RPCs) are used in the barrel and Thin Gap Chambers (TGCs) in the endcap region.

6.1.5 Triggering and Data Aquisition

The ATLAS Triggering and Data Aquisition system is shown in figure 6.6. The interaction rate is of order 10^9 Hz for a luminosity of 10^{34} cm^{-2} s^{-1}, while the bunch crossing rate is 40 MHz. It is designed to store permanently about 100 events/sec, requiring a rejection factor of 10^7 and excellent efficiency for rare physics events such as Higgs boson decays [73].

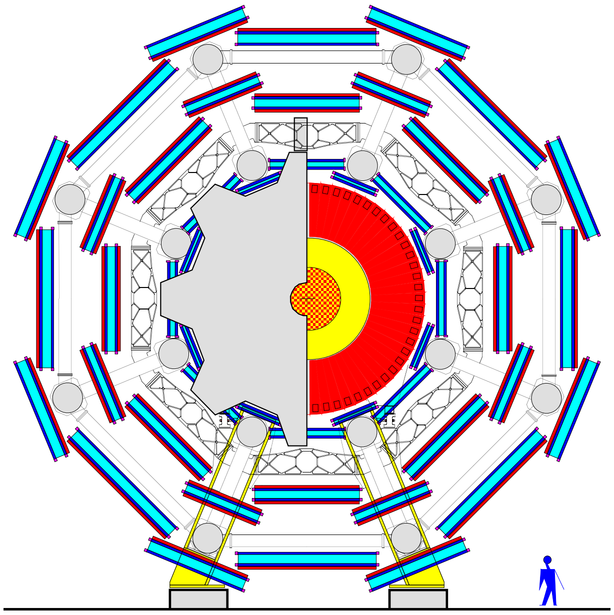

Figure 6.5: The Muon Spectrometer

The selection takes place in three different levels. Full granularity data are stored in pipeline memories while waiting for the Level 1 decision (2 μsecs). Only reduced granularity data from the calorimeter and muon trigger chambers are used for the first selection level. The calorimeter data are used looking for clusters indicative of electrons, photons and jets, as well as missing tranverse energy. Coordinates of interesting objects called Regions of Interests (RoIs) are passed to the second level in order to reduce the amount of full granularity data necessary for the Level 2 decision. The event rate is reduced to 75 kHz. The Level 1 part of the triggering system is described in detail in the next chapter.

After an acceptance from the first level, full granularity data are transfered to the readout buffers (ROBs). Derandomisers are used to average out the high instantaneous data rate coming from the first level. Data from the ROBs are selected based on RoI information supplied from Level 1, to extract features from interesting objects (electrons, photons, muons and jet candidates). This level reduces further the event rate to $\sim 1\,$kHz.

After an acceptance decision from Level 2, data stored in the readout buffers (ROBs) are assembled by an event building network and tranfered to a farm of commercials workstations for full event reconstruction and selection based on sophisticated physics criteria.

6.2 Level 1 Calorimeter Trigger

Level 1 calorimeter triggering makes the initial selection from an interaction rate of 10^9 Hz at a luminosity of $10^{34} cm^{-1} s^{-1}$ to 75 kHz for the second level while maintaining a high efficiency for interesting physics processes. Using reduced granularity information from the calorimeter, it searches for high P_T electrons and photons, as well as jets, tau leptons decaying into hadrons and missing energy. Regions of interest (the coordinates of interesting objects) are passed to the second level in order to reduce the amount of full granularity data required for the second level of selection.

6.2.1 Architectural Overview

The Level 1 calorimeter trigger is shown in figure 6.7. Trigger tower signals are transmitted as analogue pulses to the preprocessor, where flash analog to digital convertors (FADCs) transform the signals to digital form. As the duration of the calorimeter pulses is several times the bunch crossing interval, a Bunch Crossing IDentification (BCID) algorithm is required to associate calorimeter pulses with a single bunch crossing. A Look Up Table (LUT) is used for calibration in tranverse energy. In the LUT a tower E_T threshold is applied to reduce electronic and pile up noise. In addition, 2×2 tower E_T values are summed for both electromagnetic and hadronic calorimeters and transmitted via a serial link to Jet/Energy sum processor. The Cluster Processor, divided in four crates of Central Processing Modules (CPMs), performs the electron/photon and hadron/τ algorithms. The similarity of the algorithms allows them to be implemented in the same chips. The Jet/Energy sum processor consists of two crates each containing 16 Jet/Energy sum Modules(JEMs) and performs the jet algorithm. The

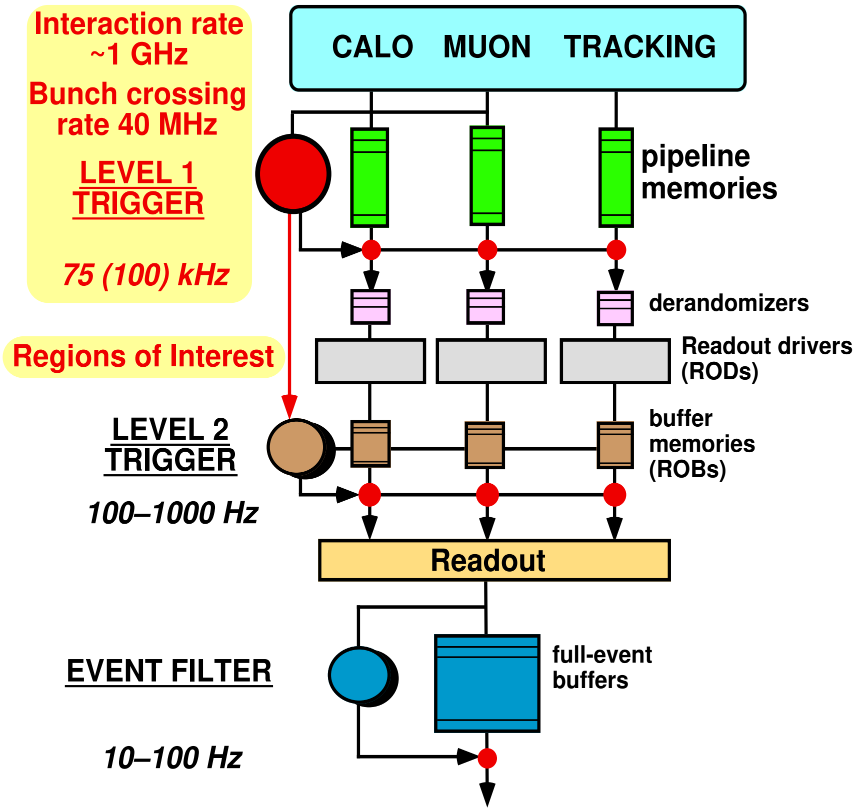

Figure 6.6: The Triggering system.

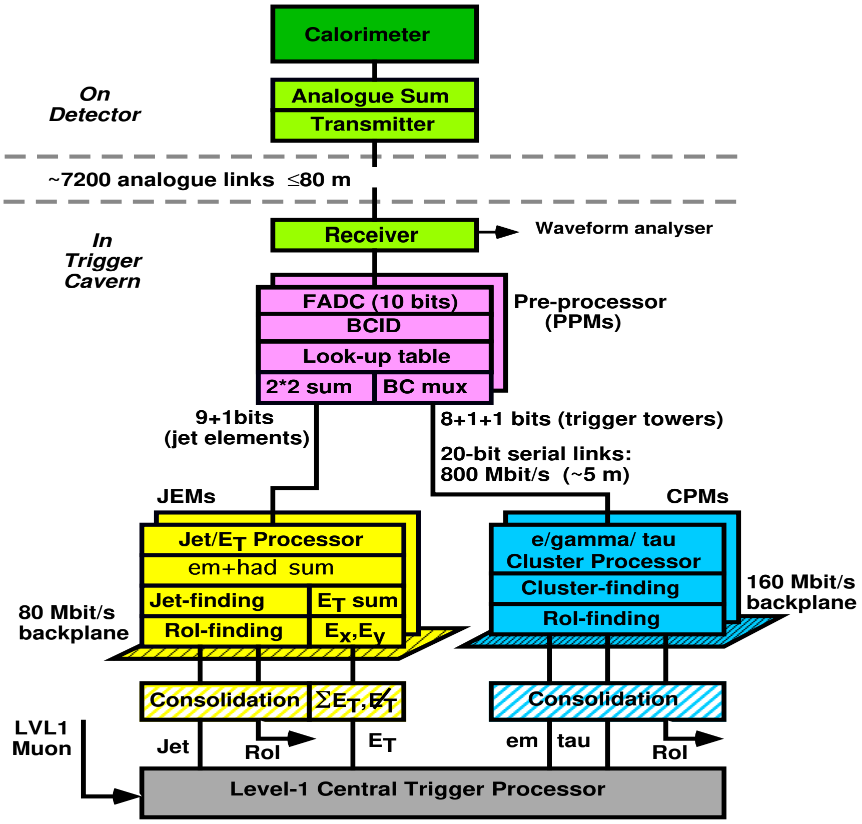

Figure 6.7: Architectural overview of Level 1 calorimeter triggering system.

results (object multiplicities) are passed to Level 1 Central Trigger Processor for the final Level 1 decision.

6.2.2 The Triggering Algorithms

The algorithms for electron/photon, τ/hadrons as well as jets are all based on a fixed size window of trigger towers ([73], [75]). Signals from the calorimeters are summed into 'trigger towers' of 0.1×0.1 in η, ϕ, with no depth segmentation other than the division between electromagnetic and hadronic calorimeters. The window consists of 4×4 trigger towers (except jets as discussed later in this section) in the η, ϕ directions, and slides in steps of one tower in either direction. There is therefore a large overlap between neighbouring windows. This is necessary to avoid mis-measuring particles which fall at the boundary between two windows, but does mean that a single particle can pass the algorithm in more than one window. To avoid multiple counting of particles, an additional 'declustering' algorithm is needed (described below).

The electron/photon algorithm

The electron/photon algorithm has to trigger on electromagnetic showers in the calorimeters (shown in figure 6.8). It is based upon a 4×4 array of 0.1×0.1 trigger towers in the electromagnetic and the hadronic calorimeters. It must recognise electron and photon candidates among high jet background. A cluster is defined as one of the four horizontal (2×1) or vertical (1×2) energy sums of the 2×2 central window. A trigger object is found if:

- The cluster with the highest energy deposit is above the electromagnetic cluster threshold.
- The energy deposits in the electromagnetic/hadronic isolation regions are below the electromagnetic/hadronic isolation thresholds respectively. This criterion is used to distinguish electron/photons over jets which spread over a bigger area.
- To prevent multiple counting due to overlapping windows, a further condition is required: the central 2×2 tower cluster within the window is a local maximum i.e. is more energetic than the 8 other 2×2 clusters which can be formed within the window. This condition is also used to define the coordinates of Regions of Interest (RoIs) for the Level 2 trigger. The above criterion is also called declustering. To take into account the case where two neighbouring 2×2 clusters contain the same energy, the local E_T maximum condition is modified: the central cluster has to have more energy than its neighbours along two adjoining edges and energy greater than or equal to its neighbours along the opposite two edges.

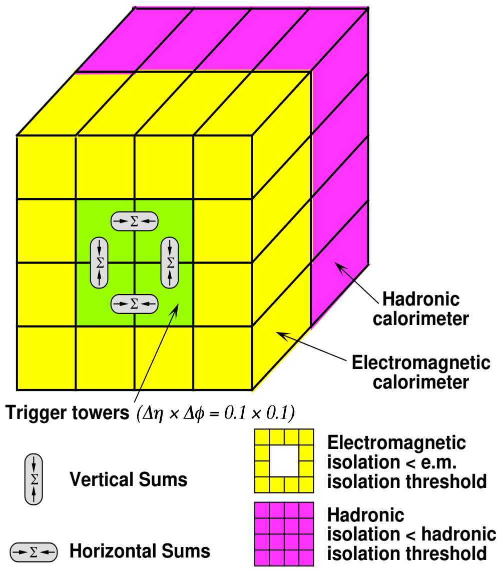

Figure 6.8: The electron/photon algorithm.

The τ/h algorithm

The task of this algorithm is to detect hadronic decays of τ leptons. Hadrons leave an energy deposit in both the electromagnetic and the hadronic calorimeter. The algorithm is very similar to the electron/photon one except:

- The trigger clusters are now the sum of 1×2 or 2×1 electromagnetic clusters plus the central 2×2 hadronic towers.
- The RoI cluster includes both the electromagnetic and the hadronic 2×2 central area.
- The hadronic isolation for τ is a 12 tower ring.

The fact that the algorithms are very similar has been exploited in the design by modifying the electron/photon algorithm slightly [74]. More specifically:

- The hadronic window is split into two isolation regions, with different energy thresholds.

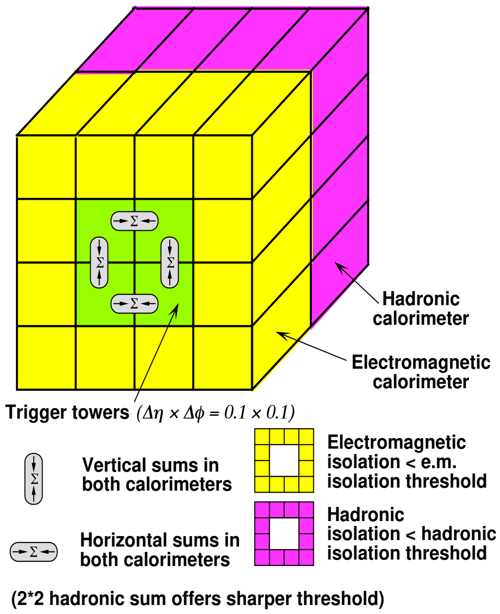

Figure 6.9: The τ, hadron algorithm.

- The RoI is the sum of 2×2 central regions in both the electromagnetic and hadronic calorimeter

The missing E_T and energy sum trigger

For the missing transverse energy and the total transverse energy triggers, the vector and scalar sums of transverse energy over all the calorimeter area (up to $|\eta|$=4.9) are used. These are defined as:

$$E_{T missing} = -\sum_{i}^{em,had} \vec{E}_T^i$$

$$E_T = \sum_{i}^{em,had} \mid \vec{E}_T^i \mid$$

For a trigger acceptance each of these triggers has to be above a defined threshold. The main features which affect resolution are:

- the ϕ granularity for converting E_T into Ex, Ey (sums of $\delta\phi$=0.2 are converted into Ex/Ey components).
- the minimum E_T included in the summation (e.g. for the energy sum trigger a threshold on the 0.2×0.2 jet elements is set and only elements above this threshold are used). This is not helpful for jet or missing energy triggers, as it will sum up all of the noise in the calorimeters, but it is necessary for the energy sum trigger.
- the energy loss in calorimeter gaps and $|\eta|$ coverage.

The rapidity range included in the summation if not extended to the forward region degrades resolution. Although the missing E_T trigger is not included in the basic Level 1 triggers, its combination with other triggers is important in order to trigger interesting events with low transverse energy. The scalar E_T sum is included to provide the most unbiassed possible trigger on the highest-energy collisions.

The Jet algorithm

The Jet algorithm is also based on a fixed size, sliding window to measure E_T, as well as an RoI to prevent double counting of jets. In the area $\eta \leq$3.2 the full jet granularity of $\delta n \times \delta\phi$=$0.2 \times 0.2$ is used. (Forward Jet Triggering is the subject of the next section and will not be examined here). Jet production is the dominant background process at the LHC so the task is to provide optimal E_T resolution rather than to distinguish different types of objects. Balance between E_T, spatial resolution and noise rejection requires different window sizes for single jet triggers (large window optimal) and multi-jets (smaller window optimal). Different window sizes are 0.4×0.4, 0.6×0.6, 0.8×0.8 are available. Finally the requirements for the algorithm to trigger are as expected: the RoI must be a local maximum and the jet cluster window must be above a defined threshold.

6.3 The Forward Jet Triggering

6.3.1 Physics Motivations

The benefit from the availability of a forward jet triggering is discussed in detail in [76]. The forward triggering will use the forward liquid argon (LAr) ATLAS calorimeter 's energy deposits in the region of $3.2 \leq \eta \leq 4.9$. The following physical processes are thought to benefit:

Higgs production via weak boson fusion ($qq \rightarrow qHq$)

The requirement of two forward jets in the triggering suppresses background from other QCD processes and improves the Signal to Background (S/B) ratio. Decays of the Higgs to two photons, taus or $W^{\star}W^{\star}$ processes might benefit from a forward triggering by the possibility of lowering thresholds for objects like photons, leptons and taus. In supersymmetric models Higgs may decay to weakly-interacting particles giving a signature of forward jets and missing energy. A forward jet triggering is crucial to observe this process which is called 'the invisible Higgs' [77].

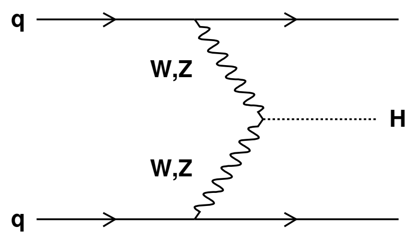

Figure 6.10: Feynman diagram for Higgs production via weak boson fusion.

Gauge boson couplings via weak boson fusion

The idea is to study single W production in association with two forward going jets.In the weak boson fusion $qq \rightarrow qWq$, two triple gauge boson vertices contribute: WWγ, WWZ. Forward jet triggering could reduce the background contributions.

Di-jet production at large rapidity separation

Specific regions of the kinematic phase space (e.g small x Bjorken variable) of QCD dynamics can be probed in the process of jet pair production at large rapidity and small transverse momenta. At large rapidity separation a forward trigger may be the only way of triggering on some parts of the cross section.

Since the LHC experiment is designed to search for new physics in the TeV region, we should be able to adapt the triggering system for the physics discovered. A forward triggering might give more flexibility in order to do that.

6.3.2 Defining the window size

Jets are characterised by a dispersed, roughly conical energy deposit in both electromagnetic and hadronic calorimeters. The signal granularity for the forward calorimeter (FCAL) is an array of 4×16 trigger towers in η, ϕ for each end (left/right) of each calorimeter (hadronic and electromagnetic). These are summed over η and in depth to form a single 1×16 array at each end (left/right), with each element having a size of 1.7×0.4 in η, ϕ.

The algorithm will be based on the same elements as the barrel jet algorithm: a fixed-size sliding window, and an E_T cluster and RoI within this. As the FCAL array is 1×16, the window would only slide in the ϕ direction. Because each tower is relatively wide in ϕ, the simplest RoI (a single element which is more energetic than its neighbours) might provide a reasonable starting point. This criterion should be relaxed to take into account the case where two trigger towers have the same energy deposit: It is required the RoI to be greater than its previous neighbour and greater and equal than its next neighbour in ϕ.

The window size can be optimized by simulation studies using the ATLFAST simulation software package [78]. If the cluster is too small, not all of the jet's energy will be contained within it, degrading resolution. Conversely, a larger cluster sums noise and pileup E_T over a larger area, and so a too large cluster will also suffer from degraded resolution (as well as an increasing probability of including more than one jet within the cluster). Five different window sizes from 1-5 trigger towers in ϕ have been simulated using ATLFAST.

The ATLFAST software used for this study is fast simulation which models only longitudinal shower development. It simulates the detector response as well as the preprocessor and all the Level 1 algorithms except the forward jet triggering. The jetfinder algorithm of ATLFAST models the jet reconstruction which should be possible in offline analysis of ATLAS data, and is used as a reference when comparing the performance of different trigger algorithms. Simulation code for all the different versions of the forward jet triggering algorithms (for cluster sizes equal to 1-5 trigger towers in ϕ) has been implemented. For each simulated event the most energetic jet triggered by the forward jet triggering and the most energetic jet found by the jetfinder algorithm of ATLFAST are compared. The correlation between the energy of the most energetic jet found by the triggering algorithm and the energy of the most energetic jet found by the jetfinder algorithm for cluster sizes 1-4 seems to be good for all cluster sizes as shown in figure 6.11.

Another way to compare performance is the sharpness of the efficiency threshold curve. This is the range in true E_T (defined by the ATLFAST jetfinder) over which the trigger efficiency rises from a low efficiency to a high efficiency (e.g. 10%-90%). The sharpness is important because all algorithms can cross 90% efficiency at the same E_T by using different thresholds. However, if the threshold curve is softer (i.e. more efficient for lower E_T jets) this will give a higher rate, because there are many more low-E_T jets than high-E_T (figure 6.12).

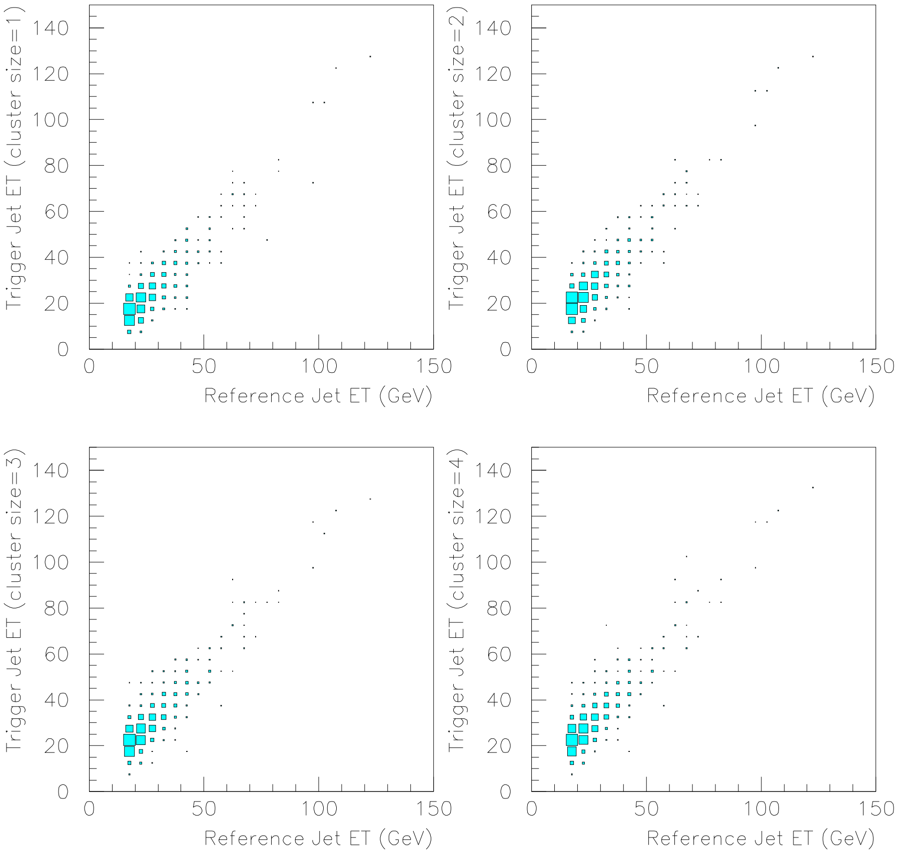

Figure 6.11: Energy correlation of the most energetic jet found by the triggering (for cluster sizes 1-4) and by the jetfinder of ATLFAST (Reference Jet).

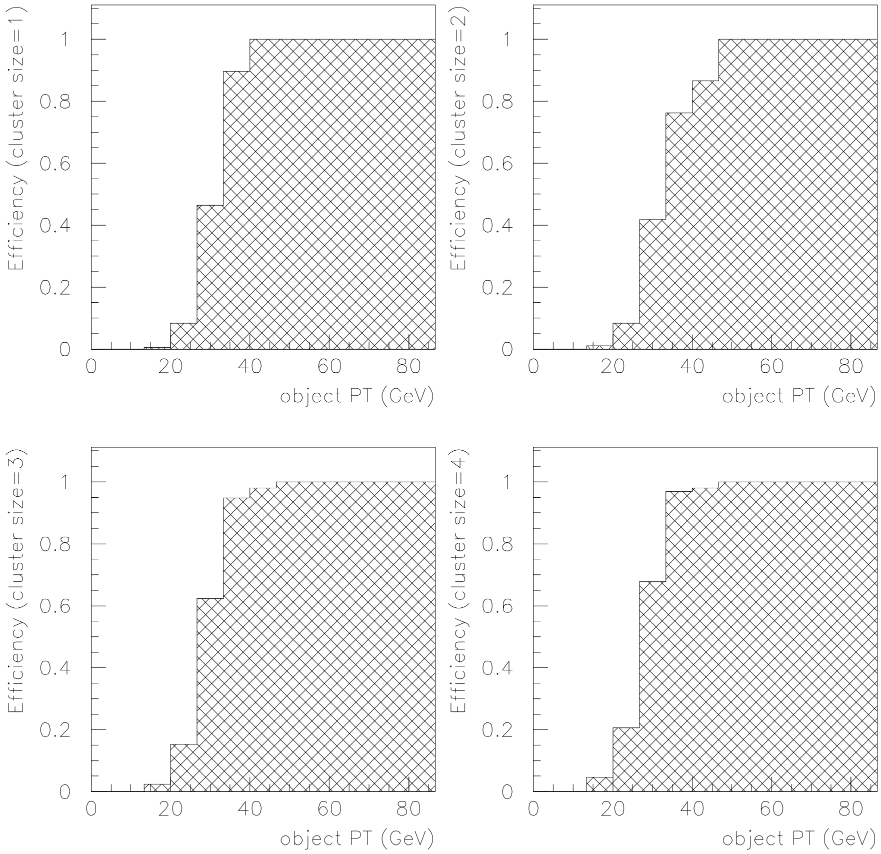

Figure 6.12: Efficiencies as a function of the triggering object momentum for a fixed threshold of 30 GeV.

6.3.3 The boundary area

Further studies in the boundary area between the forward calorimeter and the barrel at $\eta = 3.2$ have shown that there is a problem in the energy resolution in this area: Jets leave their energy deposits in both calorimeters (forward and central), so the reconstructed energy found by all versions of the forward algorithm is less than the actual jet energy. This is shown in figure 6.13 where the same plots for the energy correlation between the most energetic jet found by the triggering and the most energetic jet found by the jetfinder of ATLFAST are plotted only for the boundary region ($\eta \sim 3.2$): the correlation is worse for all cluster sizes.

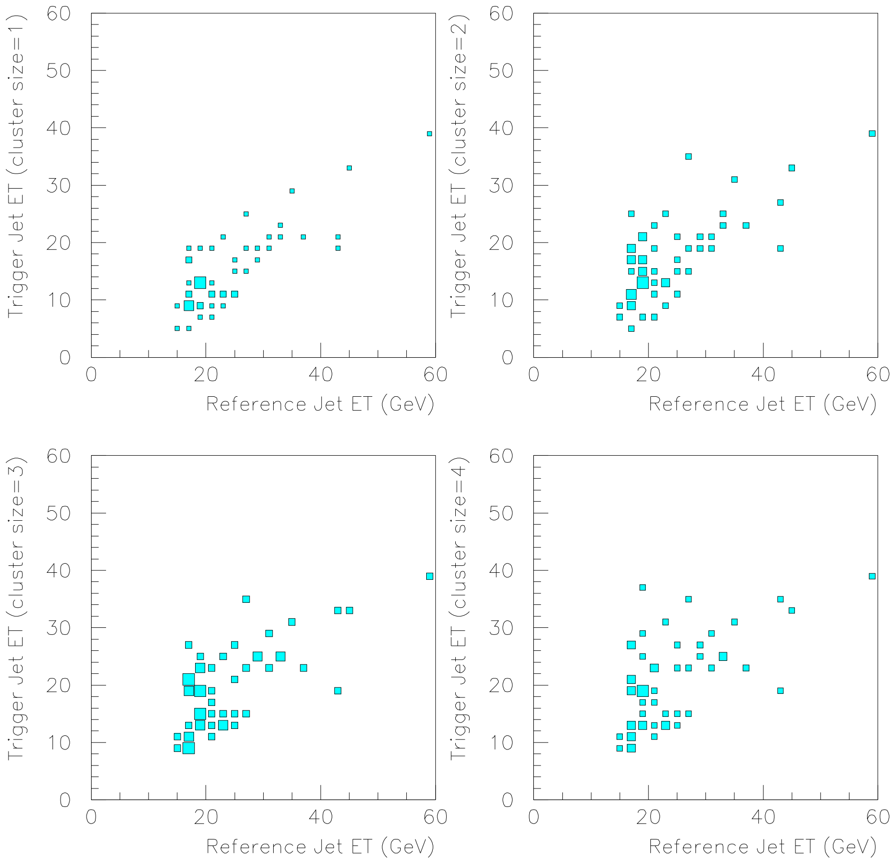

Figure 6.13: Energy correlation of the most energetic jet found by the triggering (for cluster sizes 1-4) and by the jetfinder of ATLFAST (Reference Jet), in the boundary region.

To solve this problem we have to perform a trigger algorithm based on a fixed window spanning both calorimeters, to include the jet energy deposit falling in the boundary region. This is not trivial as the geometry of the central and the forward calorimeter is different: 0.2×0.2 in the central and 1.7×0.4 in the forward calorimeter. Two different possible solutions were tested:

- Treating the forward calorimeter as an extension of the central and perform the central jet trigger algorithm in both. But in order to do that each trigger tower of the forward calorimeter was divided into two 1.7×0.2 elements and each one of them was treated as a central trigger tower, having half the energy deposit of the original forward trigger tower. As there are two different versions of the central jet triggering algorithm for window sizes 0.4×0.4 and 0.8×0.8, both of them were tested for this extension of the central algorithm in the forward region.

- Add to each 1.7×0.4 forward trigger tower the two 0.2×0.2 neighbour central towers to form a window of size 2.1×0.4. This window now includes the possible energy deposit in the central tower. The forward algorithm described earlier is performed over all the new windows formed without any further modification. A clear disadvantage of this method is the possible double counting due to the fact that the 0.2×0.2 central towers added to the forward trigger tower are also used by an independent central algorithm.

The results for these two approaches are shown in figure 6.14 for the energy correlation of the most energetic jet found by the triggering and the most energetic jet found by ATLFAST jetfinder, plotted for the whole forward calorimeter area. The upper two plots are for cluster sizes two and three of the second approach ($\delta\phi$=0.8, 1.2 respectively) and the lower two plots are for the window size 0.4×0.4 and 0.8×0.8 of the first approach. According to these plots the energy correlation is good for both approaches and better in general when compared to the plots in figure 6.11. The improvement in the correlation is most striking in the boundary region as can be seen in figure 6.15.

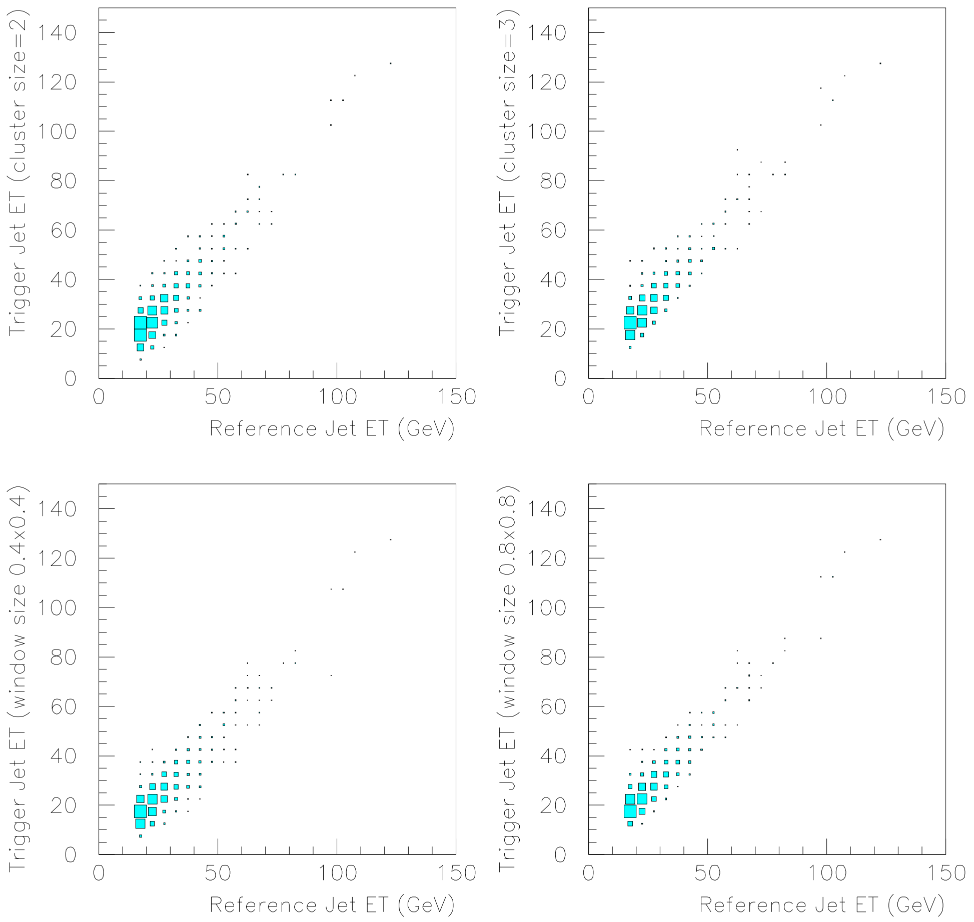

Figure 6.14: Energy correlation for cluster size 2, 3 (upper left and right) for the modified FCAL algorithm (adding central towers) and window sizes 0.4×0.4, 0.8×0.8 (lower left, right) when treating FCAL as part the central calorimeter.

	FCAL (adding central towers) Cluster Size				FCAL as extension of central region Window Size	
Algorithm	1	2	3	4	0.4×0.4	0.8×0.8
Threshold	21 GeV	24 GeV	30 GeV	31 GeV	21 GeV	24 GeV

Table 6.1: Typical thresholds for all versions of forward jet triggering algorithm that give a fixed rate of $\sim 1\,\mathrm{kHz}$.

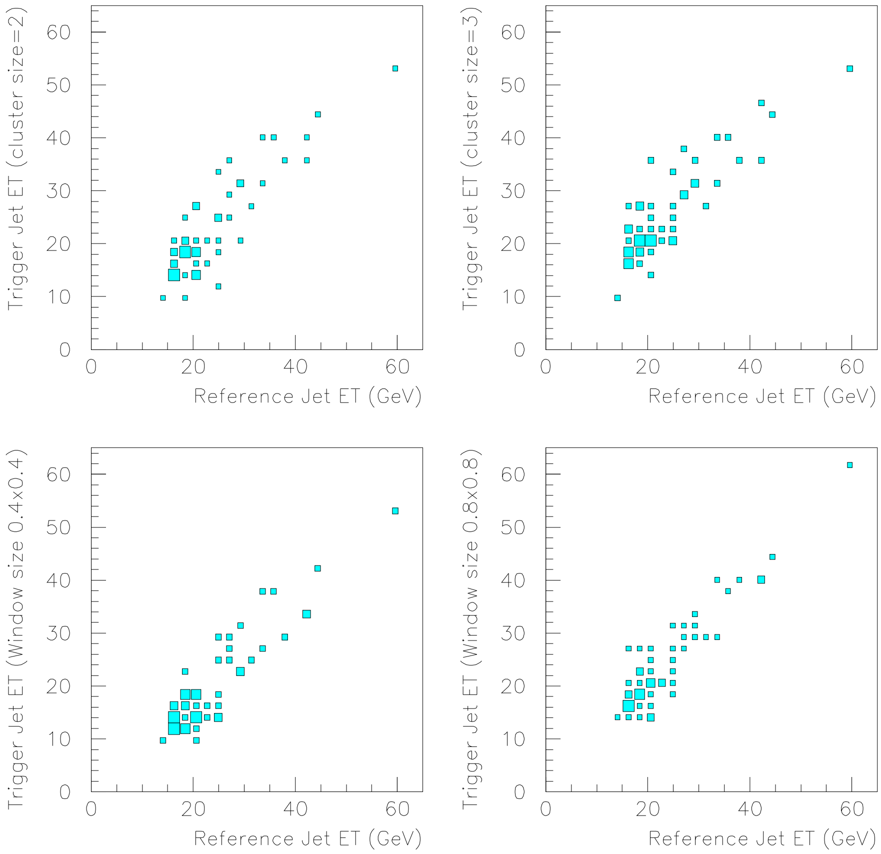

Figure 6.15: Energy correlation in the boundary region, for cluster size 2, 3 (upper left and right) and window sizes 0.4×0.4, 0.8×0.8 (lower left, right).

The next interesting question is what are the typical thresholds for the forward jet triggering giving a reasonable trigger rate. The later is estimated as:

$$Rate \quad = \quad \mathcal{L} \times \sigma_{\mathcal{QCD}} \times \ \mathcal{F} \qquad (6.1)$$

where $\mathcal{L}$ is the intergrated luminosity ($\sim 10^{33}$), $\sigma_{\mathcal{QCD}}$ is the total QCD cross-section and $\mathcal{F}$ is the fraction of generated events triggered. For a fixed rate of $\sim 1\,$kHz the thresholds required for all different versions of the forward jet triggering alogorithm were estimated as seen in table 6.1. The efficiency plots for these thresholds are presented in 6.16. For a threshold fixed to give a rate of $\sim 1\,$kHz all versions are efficient for jets of 35-40 GeV. The forward jet triggering is very likely to be combined

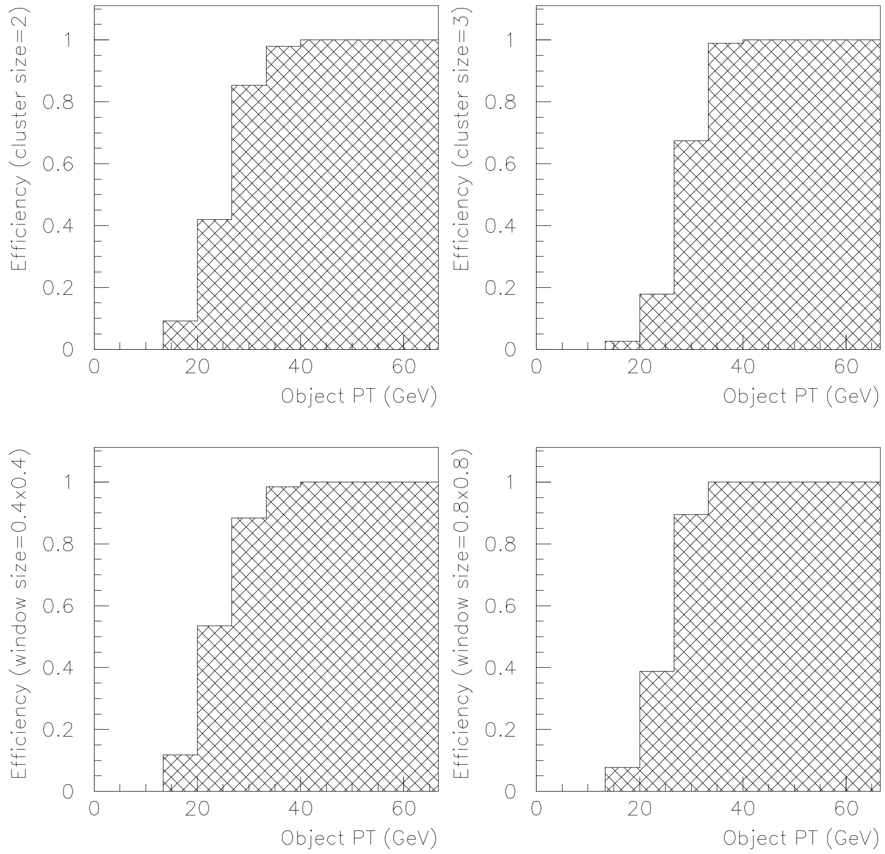

Figure 6.16: Efficiencies as a function of triggering object momentum for the thresholds of table 6.1 , using cluster size 2, 3 (upper left and right) and window sizes 0.4×0.4, 0.8×0.8 (lower left, right).

with other trigger conditions like missing E_T allowing even lower thresholds or lower thresholds.

The η distribution of the forward jets in the physics studies mentioned cover all the range from $\eta = 0$ up to 5 rather than the barrel or forward region. Thus, it is desirable to have the same framework for both . The treatment of the forward calorimeter as part of the barrel for the jet algorithm has also the advantage of being easier to implement in terms of hardware design. The window size 0.8×0.8 has at least as good energy correlation between the jet found by the triggering system and the reference as the other versions and has an equally sharp efficiency threshold curve. Therefore, it was chosen as the prefered solution. As a result of the feasibility to trigger on forward jets with resonable rates, the hardware design was modified to allow such a trigger.

Conclusions

During the last 12 years of LEP operation the Standard Model has passed successfully all difficult tests. The local, non-abelian gauge character of electroweak interactions has been verified. Two fermion observables such as cross-sections and asymmetries are an important part of the predictions made by the model and their angular distributions can be used to search for new physics.

In this thesis the analysis of tau pairs ($\mathrm{e}^+\mathrm{e}^- \rightarrow \tau^+\tau^-$) and muon pairs ($\mathrm{e}^+\mathrm{e}^- \rightarrow \mu^+\mu^-$) is presented. The effective centre of mass energy, signal and efficiency definition are complicated for both channels by the frequent emission of one or more initial state photons. The effective centre of mass energy is calculated by the angles of the two fermions assuming an undetected ISR photon emitted along the beam pipe. For planar events with a detected energetic photon the expected energy of the latter is used in the calculation to improve $\sqrt{s'}$ reconstruction.

The selection of tau pairs is complicated by the neutrinos(s) produced in tau decays. A large number of cuts is necessary to suppress the background levels based on event multiplicity, visible, missing and expected energy, as well as the coplanarity and colinearity of the tau pairs. The electron veto was implemented such as to take into account the dependance from the polar angle of the E/P ratio.

Two detector effects were studied: events with poor track reconstruction leading to misassigned track and clusters and thus zero calorimeter energy in the tau cone and events passing close to the anode wires of the CJ detector with poor momentum measurement. As the background level in the intermediate $\sqrt{s'}$ region was $\sim 40\%$ (at least double of the level in the other $\sqrt{s'}$ regions) in the selection used in the preliminary results [54], a multivariable discriminant method (likelihood) was employed to suppress it efficiently. This cut balances the background levels in all regions and suppresses the uncertainty introduced by the two photon background processes. The cross-sections and asymmetries were measured and no deviation from the Standard Model predictions was found. The dominant systematic error for both inclusive and non-radiative cross-sections is introduced by the efficiency uncertainty.

The selection of muon pairs consists of a smaller number of cuts based on the visible energy and invariant mass of the muon candidates as muons have a clean experimental signature. Cosmic rays were vetoed by imposing space-time constraints to ensure that events originate from collisions. The uncertainty introduced by the cosmic rays in the cross-section is the dominant systematic error for both inclusive and non-radiative samples. The cross-sections and asymmetries were measured and found to be in good agreement with the Standard Model predictions.

The feasibility of a forward jet trigger for the ATLAS detector at the LHC has been studied. The requirement of two forward jets can help to suppress the QCD background from other processes in the Higgs production via weak boson fusion. Different window and cluster sizes have been studied. The reconstruction of the jet energy in the boundary region between the forward calorimeter and the barrel was found to be poor compared to the rest of the $|\eta|$ region. Two different approaches were tested to improve the resolution : the first was treating the forward calorimeter as part of the barrel by dividing the towers into two parts, each having half the original energy and the second solution was adding the two neighbouring endcap towers to each forward tower. The first solution was prefered due to the fact that it was easier to implement in terms of hardware design. In addition, for at least some physics studies the jet trigger should be as uniform as possible over all η. Reasonable trigger rates can be achieved for two forward-backward jets of 35-40 GeV energy each, especially if combined with other triggers.

Bibliography

[1] O' Raifeartaugh L., The dawning of Gauge theory, Princeton University Press.

[2] Moriyasu K., Elementary Primer for Gauge Theory, World Scientific, 1983.

[3] Higgs P.W., Phys.Lett.12(1964), 132 Phys.Rev.Lett.13(1964), 508 Phys.Rev.145 (1966), 1156.

[4] t'Hooft G., 1971 Nucl.Phys. B33 173.

[5] Atchison I.J.R., and Hey A.J.G, Gauge Theories in particle physics.

[6] Glashow S.L., Nucl. Phys. 22 579, 1961.

[7] Noether E., Nachr. Ges. Wiss. Gottingen 171, 1918.

[8] Glashow S.L, Iliopoulos J., Maiani L., Phys.Rev D2, 1285, 1970.

[9] Kobayashi M., Maskawa K., Prog. Ther. Phys. 49 652, 1973.

[10] Salam A., Ward J.C., Phys. Lett 13 168, 1964.

[11] Arnison G et al., Phys. Lett. 118B 167, 1982.

[12] Utiyama R., Invariant Theoretical Interpretation of Interaction, Phys. Rev. 101 (1956) 1597.

[13] Halzen F., and Martin A.D., Quarks and Leptons: An Introductory Course in Modern Particle Physics, John Wiley & Sons, NY, 1984.

[14] Piguet O., Introduction to Supersymmetric Gauge Theories., Lectures notes hep-th/9710095.

[15] Sabbata V., Gasperini, M., Introduction to Gravitation, World Scientific 1985.

[16] Ward D.R., Green M.G., Lloyd S.L., Rattof M.G., Electron-Positron Physics at the Z, IOP publications, 1998.

[17] Wille K., The Physics of Particle Accelerators, Oxford University Press, 1996.

[18] Green D., The Physics of Particle Detectors, Cambridge University Press, 2000.

[19] Kleinknecht K., Detectors for Particle Radiation, Cambridge University Press, 1998.

[20] OPAL collaboration, The OPAL detector at LEP, Nuclear Instruments and Methods in Physics Research, A305(1991) 275-319.

[21] Anderson S. et al., The Extended OPAL Silicon Strip Microvertex Detector, Nucl. Instrum. Meth. A403, 326, 1998.

[22] Fischer H.M. et al., The OPAL Jet Chamber, Nucl. Instrum. Meth. A283, 492, 1989.

[23] Drumm H. et al., Experience with the Jet Chamber of the JADE Detector at PETRA, Nucl.Instrum.Meth. 176, A333, 1980.

[24] Kobayashi T., Realization of OPAL Electromagentic Barrel Calorimeter, 2nd International Conference on Calorimetry in HEP, Capri, Italy, 1991.

[25] Allison J. et al., Formulae and Methods in experimental data evaluation, European Physical Society, 1984.

[26] Artusi G. at al., Limited Streamer Tubes for the OPAL Hadron Calorimeter, Nucl. Instrum. Meth. A279, 523, 1989.

[27] Akers R.J. et al., The OPAL Muon Barrel Detector, Nucl. Instrum. Meth. A357, 253, 1995.

[28] Arnison G.T.J. et al., Production and Testing of Limited Streamer Tubes for the Endcap Muon Subdetector of OPAL, Nucl. Instrum. Meth. A294, 431, 1990.

[29] Cowan G., Statistical Data Analysis, Oxford University Publications, 1998.

[30] CERN Application Software Group, GEANT Detector Description and Simulation Tool, Software, Software Manual CERN, 1999.

[31] Allison J. et al., The Detector Simulation Program for the OPAL Experiment at LEP, Nucl.Instrum.Meth. A317, 47, 1992.

[32] Hawkes C. et al., ROPE user's guide, 1996, OPAL offline note 16.

[33] Arkani-Hamed N., Dimopoulos S., and Dvali G., Phys. Lett. B429 (1998) 263, hep-ph/9803315,
Antoniadis I., Arkani-Hamed N., Dimopoulos S., and Dvali, Phys. Lett. B436 (1998) 257, hep-ph/9804398,
Arkani-Hamed N., Dimopoulos S., and Dvali, hep-ph/9807344.

[34] Barberio E., Mass and Width of the W boson at e^+e^- colliers, Sienna 2001 The legacy of LEP and SLC, Proceedings.

[35] Torrence E., W boson properties, OPAL CR-473 hep-ex/0110003, Sepetember 2001.

[36] The OPAL Collaboration, K. Ackerstaff et al., Measurement of the W Boson Mass and W+W- Production and Decay Properties in e+e- Collisions at sqrt(s)=172 GeV, CERN-PPE/97-116, Eur. Phys. J. C1 (1998) 395-424, 18th August 1997.

[37] The LEP collaborations ALEPH, DELPHI, L3, OPAL and the LEP WW Working Groups, Combined Preliminary Results on the W Mass and Width of the W Boson Measured by the LEP Experiments, LEPEWWG/MASS/2002-02, OPAL TN-725, September 2002.

[38] The LEP collaborations ALEPH, DELPHI, L3, OPAL and the LEP TGC Working Groups, A Combination of Preliminary Results on the Gauge Boson Couplings

Measured by the LEP Experiments, LEPEWWG/TGC/2002-02, OPAL TN-728, October 2002.

[39] Schmidt-Karst S., W mass measurements using the fully hadronic events at LEP2, Proceedings on the International Conference on High Energy Physics, Osaka, Japan, September 200.

[40] The LEP collaborations ALEPH, DELPHI, L3, OPAL and the LEP WW Working Groups, LEP Four-Fermion Cross Section Results for the Summer 2002 Conferences, LEPEWWG/XSEC/2002-02, OPAL TN-729, November 2002.

[41] The LEP collaborations ALEPH, DELPHI, L3, OPAL and the LEP Group for Higgs Boson Searches, Search for the Standard Model Higgs Boson at LEP, ICHEP 2002 Amsterdam, LHWG Note 2002-01, July 2002.

[42] Murray W.J., Search for the Higgs in the 2 jet modes at LEP, Sienna 2001 The legacy of LEP and SLC, Proceedings.

[43] Kado Marumi., Search for the Higgs boson in the Four-Jet Channel at LEP, Sienna 2001 The legacy of LEP and SLC, Proceedings.

[44] Abbiendi G., Fermion pair production at LEP2 and interpretations, OPAL CR-477, hep-ex/0111014, November 2001.

[45] Kaluza T., On the Unification Problem of Physics, Sitzungsber, Preuss. Aka. Wiss. Berlin 1921 966.

[46] Abbiendi et al., Test of the Standard Model and Constraints on New Physics from Measurements of the Fermion-pair Production at 183 GeV at LEP, The OPAL collaboration, CERN-EP/98-108, July 1998.

[47] Abbiendi at al., Search for an Indirect Signal for the Gravity Interaction in Extra Dimensions Using Muon, Tau and Photon Pairs at $\sqrt{s} = 183$ GeV at LEP, The OPAL Collaboration, Physics Note PN381, March 1999.

[48] Kirk J., Watkins P., Talbot S.D., Tau Pair Analysis at 161 GeV, OPAL Technical Note TN-397, July 1996.

[49] Talbot S.D., Kirk J., Watkins P., Tau Pair Analysis at 172 GeV, OPAL Technical Note TN-457, January 1997.

[50] Talbot S.D., Muon and Tau Pair Analysis at 130-172 GeV, OPAL Technical Note TN-516, October 1997.

[51] Talbot S.D., Production of Muon and tau pairs using the OPAL Detector at LEP, PhD thesis, University of Birmingham, 1998.

[52] Ward C.P., private communication.

[53] Bardin D. et al., ZFITTER-An Analytical Program for Fermion Pair Production in e^+e^- Annihilation, CERN-TH-6443/92, 1992.

[54] Abbiendi G. et al., Test of the Standard Model and Constraints on New Physics from Measurements of Fermion-pair production at 130-172 GeVat LEP, Eur.Phys.J C2, 1998 441.

[55] Abbiendi G. et al., Measurement of Standard Model Processes in e^+e^- collisions at $\sqrt{s} \sim 203 - 209$ GeV, LEP2 Standard Model, WW and QCD Groups, 1st February 2001.

[56] Smith T. et al., The LL Processor in ROPE, OPAL Internal Note (1995).

[57] Bugard C. et al., WW115 Manual, OPAL Internal Note (2002)

[58] Ward D., Banks J., A Grope Primer, OPAL internal document GR202, March 1996.

[59] Bloomer J.E., Measurement of the Topological Branching Ratios of the Tau Lepton using the OPAL Detector at LEP, PhD thesis, University of Birmingham, 1997.

[60] Rigby D.A., Measurement of the Muonic Branching Ratio of the Tau lepton using the OPAL Detector at LEP, PhD thesis, University of Birmingham, 1996.

[61] Alessandro De Angelis, Invited Talk at the III Workshop on Neural Networks: From Biology to High Energy Physics (Isola d' Elba, Italy, 1994), UDPHIR 95/02/AA.

[62] Bugard C., Eatough D., Shears T., Likelihood selection for $W^+W^- \rightarrow \mathrm{q\overline{q}q\overline{q}}$ events at 171 GeV, OPAL Technical Note TN443, December 1996.

[63] Desch K., Schumacher M., Toerne E.V., A Likelihood Selection for SM-Higgs-Search in the 4-Jet-Channel,

[64] Verzocchi M., REW99: A library of routines for reweighting four fermion Monte Carlo Samples based on grc4f Matrix Elements, OPAL Technical Note TN618, August 1999.

[65] Altarelli G., Sjostrand T., Zwirner F. (Editors), Physics at LEP2, CERN 96-01, February 1996.

[66] Cartwright S. et al., Two photon physics at LEP2 RAL-97-042, hep-ph/9708478.

[67] Migliore E., 4f and 6f processes at $\mathrm{e^+e^-}$ colliders, Sienna 2001 The legacy of LEP and SLC, Proceedings.

[68] Jadach S. et al., The Monte Carlo Program KORALZ, version 4.0, for Lepton or Quark Pair Production at LEP/SLC energies, Comp. Phys. Comm. 79 (1994) 503.

[69] Kirk J., Watkins P., Talbot S.D., Muon Pair Analysis at 161 GeV, OPAL Technical Note TN-424, October 1996.

[70] Talbot S.D., Kirk J., Watkins P., Muon Pair Analysis at 172 GeV, OPAL Technical Note TN-456, January 1997.

[71] Ashby S.F., A Study of the Process $\mathrm{e^+e^-} \rightarrow \mu^+\mu^-\gamma$ at $\sqrt{s}$ <m($\mathrm{Z^0}$), $\sqrt{s} = 189$ GeV and $\sqrt{s} = 192$ GeV using the OPAL Detector at LEP, PhD thesis, University of Birmingham, 2000.

[72] ATLAS Technical Design Report, CERN/LHCC/99-14.

[73] The ATLAS First Level Trigger Technical Design Report, CERN/LHCC/98-14.

[74] Watson A., Updates to the Level-1 e/γ & τ/h Algorithms

[75] Connors A., The Level 1 Jet Trigger for ATLAS and a Preliminary Study of R-Parity violating Supersymmetry, PhD thesis, University of Birmingham, 1998.

[76] Tapprogge S., The use of a forward (jet) energy trigger at LVL1 for ATLAS, ATLAS internal note November, 1999.

[77] Girolamo B., Newkermans L., Observing the invisible Higgs in ATLAS, hep-ph/0203056.

[78] Richter-Was E., ATLFAST 2.0 a Package for Particle-level Analysis, ATLAS Internal note, (1997).

[79] Particle Physics Booklet, Particle Physics Data Group, American Institute of Physics, 2001.

[80] Lamport L., The LaTeXCompanion, Addison-Wesley Publishing Company Inc., UK, 1994.

Appendix A

Systematic errors

- Tau pairs
  - Table A1: systematic errors for energies 192, 196 GeV.
  - Table A2: systematic errors for energies 200, 202 GeV.
- Muon Pairs
  - Table A3: systematic errors for energies 192, 196 GeV.
  - Table A4: systematic errors for energies 200, 202 GeV.

	192 GeV		196 GeV	
$\Delta\sigma(Source)$	$s'/s > 0.01$	$s'/s > 0.7225$	$s'/s > 0.01$	$s'/s > 0.7225$
$\Delta\sigma(\Delta Eff_{stat})$	0.153	0.048	0.146	0.045
$\Delta\sigma(\Delta Eff_{sys})$	0.193	0.078	0.182	0.072
$\Delta\sigma(\Delta Bkg_{stat})$	0.068	0.040	0.049	0.026
$\Delta\sigma(\Delta Bkg_{sys})$	0.137	0.035	0.136	0.036
$\Delta\sigma(\Delta feed_{stat})$	0.000	0.006	0.000	0.006
$\Delta\sigma(\Delta feed_{sys})$	0.000	0.006	0.000	0.000
$\Delta\sigma(\Delta \mathrm{L}_{stat})$	0.016	0.007	0.010	0.004
$\Delta\sigma(\Delta \mathrm{L}_{sys})$	0.019	0.008	0.016	0.006
$\Delta\sigma(\Delta Interference)$	0.006	0.010	0.006	0.010
$\Delta\sigma(Statistical)$	0.948	0.502	0.574	0.300

Table A.1: Systematic errors in pb for tau pairs at energies 192, 196 GeV.

	200 GeV		202 GeV	
$\Delta\sigma(Source)$	$s'/s > 0.01$	$s'/s > 0.7225$	$s'/s > 0.01$	$s'/s > 0.7225$
$\Delta\sigma(\Delta Eff_{stat})$	0.142	0.048	0.161	0.047
$\Delta\sigma(\Delta Eff_{sys})$	0.175	0.077	0.192	0.074
$\Delta\sigma(\Delta Bkg_{stat})$	0.053	0.028	0.050	0.025
$\Delta\sigma(\Delta Bkg_{sys})$	0.137	0.038	0.140	0.037
$\Delta\sigma(\Delta feed_{stat})$	0.000	0.006	0.000	0.005
$\Delta\sigma(\Delta feed_{sys})$	0.000	0.003	0.000	0.002
$\Delta\sigma(\Delta \mathrm{L}_{stat})$	0.010	0.004	0.015	0.006
$\Delta\sigma(\Delta \mathrm{L}_{sys})$	0.016	0.007	0.018	0.007
$\Delta\sigma(\Delta Interference)$	0.005	0.009	0.006	0.009
$\Delta\sigma(Statistical)$	0.560	0.307	0.857	0.437

Table A.2: Systematic errors in pb for tau pairs at energies 200, 202 GeV.

	192 GeV		196 GeV	
$\Delta\sigma(Source)$	$s'/s > 0.01$	$s'/s > 0.7225$	$s'/s > 0.01$	$s'/s > 0.7225$
$\Delta\sigma(\Delta Eff_{stat})$	0.026	0.009	0.025	0.008
$\Delta\sigma(\Delta Eff_{sys})$	0.074	0.029	0.070	0.029
$\Delta\sigma(\Delta Bkg_{stat})$	0.021	0.006	0.021	0.006
$\Delta\sigma(\Delta Bkg_{sys})$	0.035	0.007	0.037	0.006
$\Delta\sigma(\Delta feed_{stat})$	0.000	0.003	0.000	0.003
$\Delta\sigma(\Delta feed_{sys})$	0.000	0.004	0.000	0.004
$\Delta\sigma(\Delta \mathrm{L}_{stat})$	0.015	0.006	0.009	0.004
$\Delta\sigma(\Delta \mathrm{L}_{sys})$	0.018	0.007	0.015	0.006
$\Delta\sigma(\Delta N_{cosmic})$	0.093	0.079	0.093	0.079
$\Delta\sigma(\Delta Interference)$	0.004	0.013	0.003	0.012
$\Delta\sigma(Statistical)$	0.606	0.345	0.370	0.213

Table A.3: Systematic errors in pb for muon pairs at energies 192, 196 GeV.

	200 GeV		202 GeV	
$\Delta\sigma(Source)$	$s'/s > 0.01$	$s'/s > 0.7225$	$s'/s > 0.01$	$s'/s > 0.7225$
$\Delta\sigma(\Delta Eff_{stat})$	0.024	0.008	0.021	0.007
$\Delta\sigma(\Delta Eff_{sys})$	0.066	0.028	0.056	0.024
$\Delta\sigma(\Delta Bkg_{stat})$	0.020	0.006	0.020	0.006
$\Delta\sigma(\Delta Bkg_{sys})$	0.035	0.007	0.036	0.007
$\Delta\sigma(\Delta feed_{stat})$	0.000	0.003	0.000	0.002
$\Delta\sigma(\Delta feed_{sys})$	0.000	0.004	0.000	0.003
$\Delta\sigma(\Delta \mathrm{L}_{stat})$	0.009	0.004	0.011	0.004
$\Delta\sigma(\Delta \mathrm{L}_{sys})$	0.015	0.006	0.013	0.005
$\Delta\sigma(\Delta N_{cosmic})$	0.094	0.079	0.095	0.079
$\Delta\sigma(\Delta Interference)$	0.003	0.011	0.003	0.011
$\Delta\sigma(Statistical)$	0.355	0.206	0.479	0.276

Table A.4: Systematic errors in pb for muon pairs at energies 200, 202 GeV.